USGS
science for a changing world

Prepared in cooperation with the Bureau of Land Management

Landscape Evolution in Eastern Chuckwalla Valley, Riverside County, California

Scientific Investigations Report 2021–5017

U.S. Department of the Interior
U.S. Geological Survey

Cover. U.S. Geological Survey photograph of wind-rippled sand and sand verbena in eastern Chuckwalla Valley, Riverside County, California.

Landscape Evolution in Eastern Chuckwalla Valley, Riverside County, California

By Amy E. East, Harrison J. Gray, Margaret Hiza Redsteer, and Matthew Ballmer

Prepared in cooperation with the Bureau of Land Management

Scientific Investigations Report 2021–5017

U.S. Department of the Interior
U.S. Geological Survey

U.S. Geological Survey, Reston, Virginia: 2021

For more information on the USGS—the Federal source for science about the Earth, its natural and living resources, natural hazards, and the environment—visit https://www.usgs.gov or call 1–888–ASK–USGS (1–888–275–8747.

For an overview of USGS information products, including maps, imagery, and publications, visit https://store.usgs.gov.

Suggested citation:
East, A.E., Gray, H.J., Redsteer, M.H., and Ballmer, M., 2021, Landscape evolution in eastern Chuckwalla Valley, Riverside County, California: U.S. Geological Survey Scientific Investigations Report 2021–5017, 46 p., https://doi.org/10.3133/sir20215017.

Associated data for this publication:
Gray, H.J., and East, A.E., 2021, Luminescence, weather, and grain-size data from eastern Chuckwalla Valley, Riverside County, California: U.S. Geological Survey data release, https://doi.org/10.5066/P9LZ02E4.

ISSN 2328-0328 (online)

Contents

Figures

Tables

Conversion Factors

International System of Units to U.S. customary units

Multiply	By	To obtain
	Length	
centimeter (cm)	0.3937	inch (in.)
millimeter (mm)	0.03937	inch (in.)
meter (m)	3.281	foot (ft)
kilometer (km)	0.6214	mile (mi)
	Area	
square meter (m^2)	0.0002471	acre
square kilometer (km^2)	247.1	acre
square centimeter (cm^2)	0.001076	square foot (ft^2)
square meter (m^2)	10.76	square foot (ft^2)
square centimeter (cm^2)	0.1550	square inch (ft^2)
square kilometer (km^2)	0.3861	square mile (mi^2)
	Mass	
kilogram (kg)	2.205	pound avoirdupois (lb)
	Velocity	
meter per second (m/s)	3.281	feet per second (ft/s)

Temperature in degrees Celsius (°C) may be converted to degrees Fahrenheit (°F) as follows:

$$°F = (1.8 \times °C) + 32.$$

Temperature in degrees Fahrenheit (°F) may be converted to degrees Celsius (°C) as follows:

$$°C = (°F - 32) / 1.8.$$

Datum

Vertical coordinate information is referenced to the North American Vertical Datum of 1988 (NAVD 88).

Horizontal coordinate information is referenced to the North American Datum of 1983 (NAD 83).

Elevation, as used in this report, refers to distance above the vertical datum.

Supplemental Information

Wind direction is given in degrees azimuth, for which 0, 90, 180, and 270 degrees refer to due north, east, south, and west respectively.

Abbreviations

cm	centimeter
CAM	central age model
DOD	U.S. Department of Defense
ENSO	El Niño Southern Oscillation
EPA	U.S. Environmental Protection Agency
IRSL	infrared-stimulated luminescence
ka	kilo-annum (thousand years ago)
km	kilometer
km^2	square kilometer
k.y.	thousand years (duration)
LGM	Last Glacial Maximum
LPSA	Coulter laser particle-size analyzer
m	meter
Ma	mega-annum (million years ago)
m/s	meter per second
m/yr	meter per year
PDO	Pacific Decadal Oscillation
pIRIRSL	post-infrared infrared-stimulated luminescence
ppm	parts per million
PRISM	Parameter-elevation Regression on Independent Slopes Model
USGS	U.S. Geological Survey

Landscape Evolution in Eastern Chuckwalla Valley, Riverside County, California

By Amy E. East,[1] Harrison J. Gray,[1] Margaret Hiza Redsteer,[2] and Matthew Ballmer[3]

Abstract

This study investigates sedimentary and geomorphic processes in eastern Chuckwalla Valley, Riverside County, California, a region of arid, basin-and-range terrain where extensive solar-energy development is planned. The objectives of this study were to (1) measure local weather parameters and use them to model aeolian sediment-transport potential; (2) identify surface sedimentary characteristics in representative localities; and (3) evaluate long-term landscape evolution rates and processes by analyzing stratigraphy in combination with luminescence geochronology.

The new stratigraphic and geochronologic data presented in this report demonstrate the varying local significance of aeolian, alluvial fan, lacustrine (playa), and possibly Colorado River influence over a range of time scales. The dominant sand-transport direction in eastern Chuckwalla Valley is toward the northeast, consistent with the recognized regional west-to-east wind direction. However, occasional strong wind events from the north can transport large quantities of sand southward and temporarily reshape local geomorphic features. Influence of a northwest wind direction is also locally dominant around mountain ranges and controls the modern morphology of the Palen dune field. Modeled sand fluxes are on the order of 10^5 kilograms per meter width per year at the site of weather monitoring, 5 kilometers northwest of the Mule Mountains. Aeolian dunes are locally well developed and actively migrating. Their location and activity are determined largely by sediment supply from playa surfaces and ephemeral stream channels, which also control the dunes' spatial extent and migration potential; stream channels act as both source and sink for aeolian sediment in this environment.

Excavations at five sites along a northwest-to-southeast transect reveal that playa deposits formed around 266–226 thousand years ago south of the McCoy Mountains and immediately north of the present location of Interstate 10. The playa material is overlain by late Pleistocene to Holocene alluvial fan deposits. To the southeast (south of Interstate 10, but north of the Mule Mountains), we identified rapid accumulation of alluvial sediment around the time of the Last Glacial Maximum (23–20 thousand years ago), unconformably overlain by a locally varying assemblage of recent aeolian material or Holocene alluvial fan sediment. We have used stratigraphic characteristics and luminescence ages to calculate accumulation rates for sites in eastern Chuckwalla Valley, and thereby to identify spatial variation in landscape stability over decadal and longer time scales.

If future solar-energy development plans are to include natural sand-transport corridors, plans would entail retaining the ability for sand to be transported eastward from the ephemeral stream channels and playas that supply sediment to the dunes, sand sheets, and sand ramps of Chuckwalla Valley, and also to allow for southward transport during episodic strong weather events several times per year. The aeolian sediment-transport corridors are dynamic spatially and temporally, reorganizing on the basis of seasonal changes to wind drift potential. Future landscape stability also will be determined by climate-driven changes to vegetation and thereby to aeolian sediment availability. In a warmer, drier climate, aeolian sediment activity is expected to increase, owing to a decrease in stabilizing vegetation cover and more extreme rain that supplies sediment to ephemeral stream channels and playas from which it is remobilized by wind.

Introduction

Large areas of the southwestern U.S. deserts are being developed for solar-energy generation. Installing and maintaining productive solar infrastructure in drylands requires detailed knowledge of local and regional surficial geology and the geomorphic processes that are likely to influence the landscape over seasonal to multidecadal time scales. Like other desert regions, drylands of the southwestern U.S. are shaped by various geomorphic and sediment-transport processes, including aeolian (windblown) sediment movement and fluvial and alluvial fan runoff. Understanding how the local significance of those processes varies through space and time is key to identifying feasible locations for solar arrays.

This study investigates landscape evolution in a region of the Sonoran Desert within eastern Riverside County, southeastern California. We analyzed weather conditions, geomorphic processes, and rates of sediment accumulation at representative sites within a 110-square kilometer (km^2) region of Chuckwalla Valley west of Blythe, Calif. (fig. 1), an area designated by the

[1]U.S. Geological Survey.

[2]School of Interdisciplinary Arts and Sciences, University of Washington.

[3]U.S. Department of Agriculture.

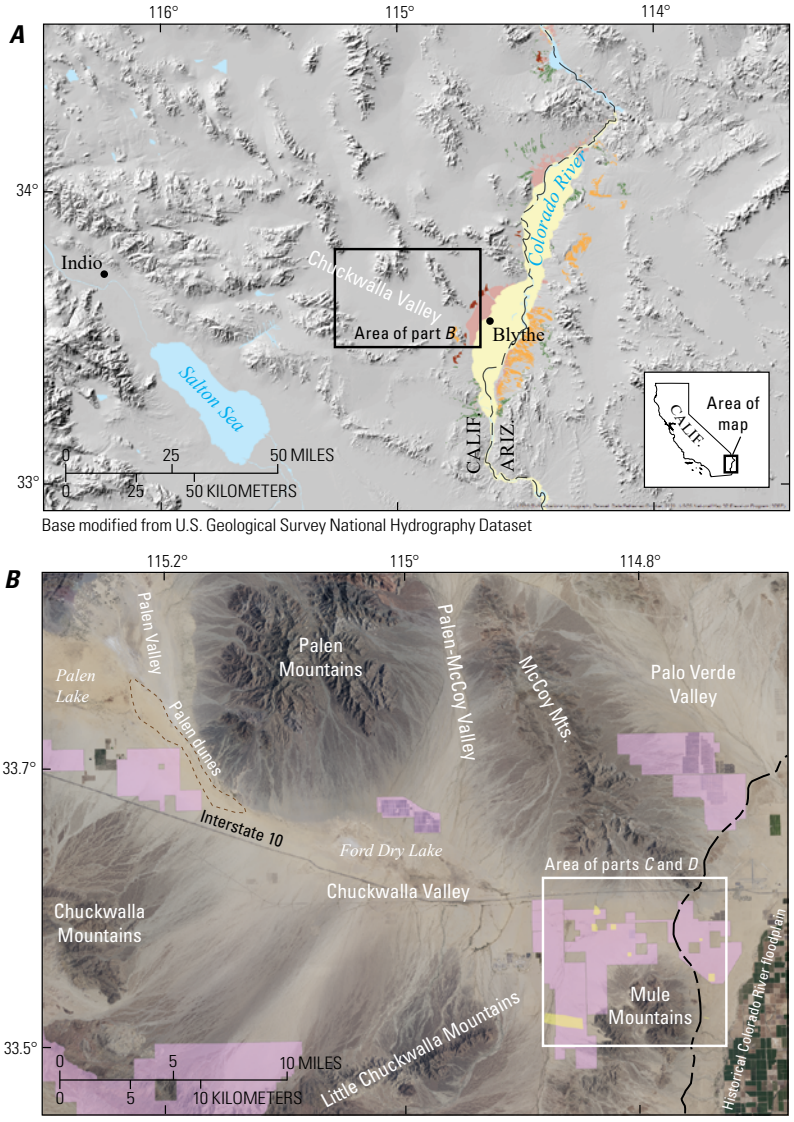

Figure 1. Maps and images of the study area in Chuckwalla Valley, eastern Riverside County, California (Riverside East Development Focus Area). *A*, Shaded-relief map of the field area within southeastern California and western Arizona. Demarcated within the Colorado River corridor are sedimentary deposits of the Colorado River dating from approximately 6 Ma to the Holocene, as mapped by Crow and others (2018); yellow, Blythe Alluvium; pink, Chemehuevi Formation; red, Palo Verde alluvium; orange, Bullhead Alluvium; and green, Bouse Formation (see Crow and others, 2018, for detailed descriptions and discussions of probable ages). Box indicates area shown in panel *B*. *B*, Aerial photograph showing the eastern Chuckwalla Valley, with major basins and ranges labeled. Brown dashed line shows the approximate recent boundary of the Palen dune field. Pink-shaded areas have been permitted for solar-energy development. Yellow-shaded areas are U.S. Geological Survey (USGS) polygons referred to in this report. Black dashed line at eastern side shows the approximate west boundary of ancient Colorado River gravels (Palo Verde Mesa), as mapped by Stone (2006). Box indicates area shown in detail in *C*. *C*, Aerial photograph showing greater detail of study area in eastern Chuckwalla Valley. For clarity, permitted solar-energy zones have been omitted. Yellow-shaded areas are USGS study polygons. Weather station is shown by a blue circle and subsurface pits by red circles. *D*, Portion of geologic map by Stone (2006) showing the focus area (white box) in *B*. Units pertinent to discussion in this report are from Stone (2006) and include alluvium of modern washes (Qw), alluvial deposits of the Mule Mountains (QTmm), eolian sand (Qs), playa lake deposits (Qp), and units 3 and 6 of the alluvial fan and alluvial valley deposits (Qa3 and Qa6, respectively). Stone (2006) interpreted the QTmm deposits as likely associated with a former channel of the Colorado River.

Bureau of Land Management as the Riverside East Development Focus Area. By measuring the rates and processes by which sediment accumulates or moves across this landscape, we provide new information relevant to the longevity and performance of future solar-energy facilities in this region.

Objectives

The objectives of the study in eastern Chuckwalla Valley (Riverside East Development Focus Area) were to: (1) measure local weather parameters and use them to estimate modern aeolian sediment transport potential for several seasons; (2) identify surface sedimentary characteristics in representative areas of eastern Chuckwalla Valley; and (3) evaluate long-term landscape evolution rates and processes by analyzing stratigraphy in combination with luminescence geochronology. These methods allowed us to identify the most relevant landscape processes and the ways in which they interact over a range of time scales. The results could be used to help determine the feasibility of solar energy development in eastern Chuckwalla Valley. Moreover, one goal of the Bureau of Land Management solar energy development plan is to preserve natural sand-transport processes and pathways and to maintain habitat condition for *Gopherus agassizii* (desert tortoise), *Uma scoparia* (Mojave fringe-toed lizard), and other sensitive species; this report provides new information relevant to understanding aeolian sand-transport pathways and time scales of sediment movement to assist with that effort. Future studies may use geochemical and mineralogic characteristics from key geomorphic features to examine sediment provenance and infer sediment-transport pathways.

Field Setting and Previous Work

Chuckwalla Valley, east Riverside County, California, trends east-west in the northwestern part of the Sonoran Desert, within the basin-and-range province of the southwestern U.S. (fig. 1). Mountain ranges flanking the valley consist of Mesozoic metamorphic rocks (meta-igneous and metasedimentary bedrock), whereas other local ranges consist of Tertiary (mostly Oligocene and Miocene) volcanic rocks with minor occurrences of granite (Stone and Kelly, 1989; Sherrod and Tosdal, 1991; Stone, 2006). This study focuses on a 110 square kilometer (km^2) area within the valley. The range nearest our study area, the Mule Mountains (fig. 1), consists primarily of Jurassic plutonic and volcanic rocks (Stone, 2006). Bedrock in the McCoy Mountains, immediately to the north, is predominantly Cretaceous sedimentary rocks (siliciclastic sandstones, shales, and conglomerate with minor carbonate occurrence); many lithic clasts within the Cretaceous units are volcanic in origin (Stone, 2006).

The Colorado River truncates the east end of Chuckwalla valley, forming the east boundary of Riverside County and the California–Arizona state line. Because the location of Colorado River channels have shifted continuously in historical and prehistoric time, large paleochannels are present beneath the city of Blythe, Calif., and throughout its surroundings (fig. 1; for example, Crow and others, 2018; Block and others, 2019). Much of the historical floodplain is developed for agriculture today. Paleochannel deposits of the Colorado River include fluvial gravels containing well-rounded siliciclastic particles; the oldest comprise Pleistocene deposits of Palo Verde Mesa (Metzger and others, 1973; Stone, 2006). Additional Pliocene to Pleistocene exposures of alluvial gravels occur south of the McCoy Mountains but have an unresolved stratigraphic relation with the Palo Verde Mesa deposits. The westernmost local exposures of fluvial gravels that are thought to be associated with the ancestral Colorado River occur on the north and northwest sides of the Mule Mountains, at elevations of 150–240 m (unit QTmm of Stone, 2006; fig. 1D). The Pleistocene or Pliocene sedimentary deposits (unit QTmm of Stone, 2006) consist of weakly to moderately consolidated sand and pebbly sand interbedded with locally derived gravel. Stone (2006, p. 12) described "rounded river pebbles, mostly quartzite and chert" in the QTmm deposits and noted that the unit extends through a wide depression in the northwestern Mule Mountains, probably marking a former channel of the Colorado River.

Key geomorphic features of eastern Chuckwalla Valley include a north-flowing ephemeral stream informally named Wiley Well wash, which flows into the valley from the south and delivers sediment to the valley floor near key sampling sites (fig. 1). Playa deposits associated with ephemeral lakes, as well as aeolian dunes and sand sheets, are common on the valley floor adjacent to the terminus of this and other washes. Chuckwalla Valley also contains alluvial fans that are sourced from the surrounding ranges. Alluvial fans in the southwestern U.S. typically are deposited by large, episodic floods and debris flows that form and evolve during major storms (for example, Harvey and others, 1999; D'Arcy and others, 2017). Work by Miller and others (2010) has indicated that alluvial fans in this region may aggrade most commonly owing to flash floods and debris flows during intense summer storms, whereas their channels likely incise during floods caused by less intense cool-season frontal storms. The discharge from these alluvial fans drains into ephemeral channels, which empty into ephemeral, closed lake basins that form playa deposits after desiccation. Interspersed between these alluvial features are the aeolian dunes and sand sheets; the aerial photograph in figure 1*B* illustrates the juxtaposition of alluvial fans, aeolian sand sheets, and playa deposits in this region. Dunes in this study area range from less than one meter to several meters tall. Some previous research has described the aeolian features as forming sand-transport corridors, wherein wind deflection (topographic steering) by mountain ranges facilitates sand transport between various aeolian depocenters (for example, Zimbelman and others, 1995). The sand-transport corridors are argued to have developed as a result of climatic conditions (Lancaster and Tchakerian, 2003), although sediment supply and geomorphic factors introduce nuance into this conceptual framework, as we discuss further below (Muhs and others, 2003). Our field area occupies part of the Clarks Pass system described by Zimbelman and others (1995).

Geomorphic features and their formative processes interact extensively in southwestern U.S. drylands (for example, Parsons and Abrahams, 2009; Nials and others, 2013; Lancaster, 2020; Redsteer, 2020). Streamflow in ephemeral washes supplies

sediment to aeolian dunes and sand sheets downwind (Clarke and Rendell, 1998; Draut and others, 2012; Bogle and others, 2015), and playa surfaces are commonly sources of aeolian dust (Reheis and Kihl, 1995; Pelletier, 2006; Reynolds and others, 2007). Zimbelman and others (1995) and Muhs and others (2003), while investigating regional aeolian sand-transport pathways for southeastern California and western Arizona, found that locally derived alluvium is a major source of aeolian sediment in dunes and sand sheets in eastern California, whereas in western Arizona the Colorado River becomes a significant source of sediment in aeolian deposits to the east (downwind). Alluvial fan morphology and sediment composition in desert environments are modified by water as overland flow, and by wind reworking that adds sediment to the fan from noncatchment sources, in some places forming aeolian sand sheets on top of alluvial fan deposits (Blair and McPherson, 2009).

The regional climate in eastern Riverside County is arid and is classified as the hot desert (BWh) category in the Köppen-Geiger climate classification (Beck and others, 2018). From 1981 to 2010 annual rainfall was about 10 centimeters (cm) there, and temperatures are some of the hottest in the U.S.; mean annual temperature is 22–25 °C, and maximum temperature is above 40 °C during July, August, and September (Parameter-elevation Regression on Independent Slopes Model [PRISM], 2020). These warm temperatures are partly attributable to low elevation: elevations within eastern Chuckwalla Valley are generally 100–250 meters (m) above sea level. The lowest local elevation is about 80 m and occurs in the Colorado River floodplain near the town of Blythe, Calif. Historical precipitation records from Blythe show that the driest months of the year occur during spring (April to June); June typically has zero precipitation (National Oceanic and Atmospheric Administration, 2020a). Approximately 65 percent of rainfall occurs in winter as a result of cold frontal storms. The remaining 35 percent occurs during summer and early fall: July to October, the North American Monsoon season, when moisture is advected inland from the Gulf of California (Maddox and others, 1995; Young and others, 2017). Monsoon-season storms can include severe thunderstorms and flash flooding (for example, Griffiths and others, 2009). Occasional tropical cyclones also bring moisture into southwestern U.S. deserts during late summer, causing regional flooding (Barth and others, 2018). On annual to multidecadal time scales, regional climate is influenced by the El Niño Southern Oscillation (ENSO) and Pacific Decadal Oscillation (PDO) cycles (Hereford and others, 2006; Seager and others, 2007), but the ways in which those teleconnections influence southern California's weather and climate remain incompletely understood (Lee and others, 2018). The southwestern U.S. has dried measurably in the past 30 years (Seager and others, 2007; U.S. Global Change Research Program [USGCRP], 2018) and since 2000 has developed persistent, severe dry conditions now considered a megadrought, partly attributable to anthropogenic warming (Williams and others, 2020). Particularly extreme drought from 2012 to 2015 in California was both temperature- and precipitation-driven, had an historical recurrence interval of greater than a century (Biondi and Meko, 2019), and may have been the most severe drought of the past 1,400 years (AghaKouchak and others, 2014; Griffin and Anchukaitis, 2014; Hatchett and others, 2015). Its severity is thought to exemplify future drought conditions in this region as climate continues to warm (Diffenbaugh and others, 2015; Ullrich and others, 2018; Williams and others, 2020).

Landscapes in the study region are sparsely vegetated. We did not conduct systematic vegetation surveys but noted that on sandy surfaces the dominant shrub species is *Larrea tridentata* (creosote; fig. 2), and *Ambrosia dumosa* (burrobush) is also common, especially in broad, flat, and sandy landscapes with little active sand transport. Examples of other common species include *Abronia villosa* (sand verbena), *Sphaeralcea emoryi* (globemallow), *Hesperocallis undulata* (desert lily), and grasses including *Pleuraphis* sp. (galleta) and *Aristida purpurea* (three-awn). Locally occurring nonnative vegetation includes invasive *Brassica tournefortii* (Sahara mustard), *Schismus* sp. (schismus grass), and, less commonly, *Salsola* sp. (Russian thistle). Additional information on vegetation in this region can be found in the work of Menke and others (2016).

A 300-m-deep well drilled by Everett and others (2013) in eastern Chuckwalla Valley near the depocenter of Wiley Well wash revealed silt and clay deposits with marl (carbonate mineral accumulations) alternating with silty sand beds primarily below a depth of 86 m, which the authors assigned to the (informally named) Pinto formation. These were overlain at that location by a series of very fine to medium sand, sandy silt, and silty gravelly sand deposits, described collectively as "alluvium" by Everett and others (2013) and assigned no formal stratigraphic name.

The most recent geomorphic investigations covering portions of our study area were by Kenney (2016) and Kenney (2018), who described geomorphic features and investigated subsurface material with a focus on the north and east sides of the Mule Mountains while assessing feasibility for the proposed Crimson Solar Project. The report by Kenney (2016) identified a transition from alluvial to eolian deposition occurring during the early to middle Holocene (8 to 5 thousand years ago [ka]) in the area northeast of the Mule Mountains. In contrast, working farther to the northwest in Palen Valley (fig. 1*B*), Nials and others (2013) identified Pleistocene aeolian and alluvial deposits interbedded and overlain unconformably by late Holocene to modern alluvium, but no early or mid-Holocene strata were observed. Kenney (2018) noted that aeolian sand-migration pathways tend to be local rather than regional and driven by topographic steering of wind around mountain ranges; he also used geomorphic features to infer likely local transport pathways around the northeastern part of the Mule Mountains. Kenney (2018) recognized that on the flanks of the Mule Mountains sediment moves downslope when carried by alluvial fan runoff and can be carried back up the alluvial fan channels by wind. However, he inferred that the dominant local aeolian transport direction appeared to be toward the northeast, consistent with the interpretations of Muhs and others (2003). Transport also was inferred from sand sources in Palen Valley (fig. 1*B*), implying a component of sand migration directed toward the south-southeast (Plate 3A of Kenney, 2018). This interpretation by Kenney (2018) was consistent with a

remote-sensing analysis having shown that dunes in the Palen dune field (fig. 1*B*) migrate about 50 meters per year (m/yr) toward the south-southeast (Potter and Weigand, 2016).

Having found that in the area northeast of the Mule Mountains the aeolian sediment was commonly about 1 m thick and underlain by Holocene material, Kenney (2018) inferred that modern accumulation rates of aeolian sand are low, that the aeolian sand was derived from local rather than far-field sources, and that local sand deposits are "stable and degrading." Moreover, Kenney (2018) posited that aeolian deposits were unlikely to become active in the immediate vicinity of the Mule Mountains "for at least a thousand years," even under warmer, drier climate. Other studies have found that potential aeolian transport from local sources commonly does occur in similar settings, as source-bordering dunes (Draut and others, 2012; Bogle and others, 2015) and can pose risks to infrastructure.

Kenney (2018) also noted that when (nonnative) Sahara mustard plants bloom during late winter and early spring, the vegetation cover can become so dense locally that sand entrainment by wind is almost nonexistent. However, vegetation cover does not preclude periods of aeolian sediment transport if vegetation germination and growth is out of phase with wind events or if pulses of sediment from local sources form dunes that migrate over a stable vegetated surface (Bogle and others 2015).

Our present study expands on previous work and considers a larger field area (about 110 km^2) to examine the potential aeolian sediment transport and local dune activity. By focusing generally north of the 35-km^2 region studied by Kenney (2018), we included areas other than the Crimson Solar Project that also have been permitted provisionally for solar-energy development (fig. 1). We obtained and analyzed stratigraphic and geochronologic information from areas not previously investigated, and we collected high-resolution weather data that were used to model potential aeolian sand flux in eastern Chuckwalla Valley.

Methods

Our assessment of landscape processes in the Riverside East Development Focus Area involved measuring local weather parameters and using the data to estimate aeolian sand-transport potential, characterizing surface sediment and modern geomorphic processes, and using stratigraphy and luminescence geochronology to quantify long-term accumulation rates. The following descriptions of the weather-station deployment and locations of sedimentary and stratigraphic data collection refer to eight areas (polygons) that we selected to be representative of various geomorphic settings in eastern Chuckwalla Valley. Locations of the polygons are shown on figure 1.

Weather Monitoring and Sand-Transport Modeling

We deployed a weather station on February 7, 2019, at lat 33.584° N., long 114.830° W., on a sparsely vegetated sand sheet within polygon 2 (fig. 2). The station consisted of sensors (mounted on a tripod) that measure wind speed, wind direction, air temperature, and relative humidity. Wind speed and wind direction were measured at a height of 2 m above the ground surface. The wind-speed sensor was an Onset S-WSB-M003 unit capable of measuring wind speed from 0 to 76 meters per second (m/s). This sensor has a starting threshold of 1 m/s and reports the average wind speed and maximum 3-second gust over each logging interval. The wind-direction sensor was an Onset S-WDA-003 unit with a manufacturer-stated resolution of 1.4 degrees and accuracy within 5 degrees. This sensor has a measurement range of between 0 and 355 degrees azimuth, and so does not resolve wind direction within 5 degrees west of north. It uses vector components of wind direction, averaged every 3 seconds, to provide average wind direction over the logging interval. Temperature and relative humidity were measured using an Onset S-THB-M002 sensor. Temperature measurements from that sensor have an accuracy of ± 0.21 °C from 0 to 50 °C and resolution of 0.02 °C. Relative humidity measurements (0–100 percent) made with that sensor have 0.1 percent resolution and accuracy ± 2.5 percent from 10 to 90 percent relative humidity, although below 10 percent or above 90 percent the accuracy decreases to ± 5 percent. These three sensors were connected to an Onset U30 data logger, which was set to 4-minute logging and averaging intervals throughout

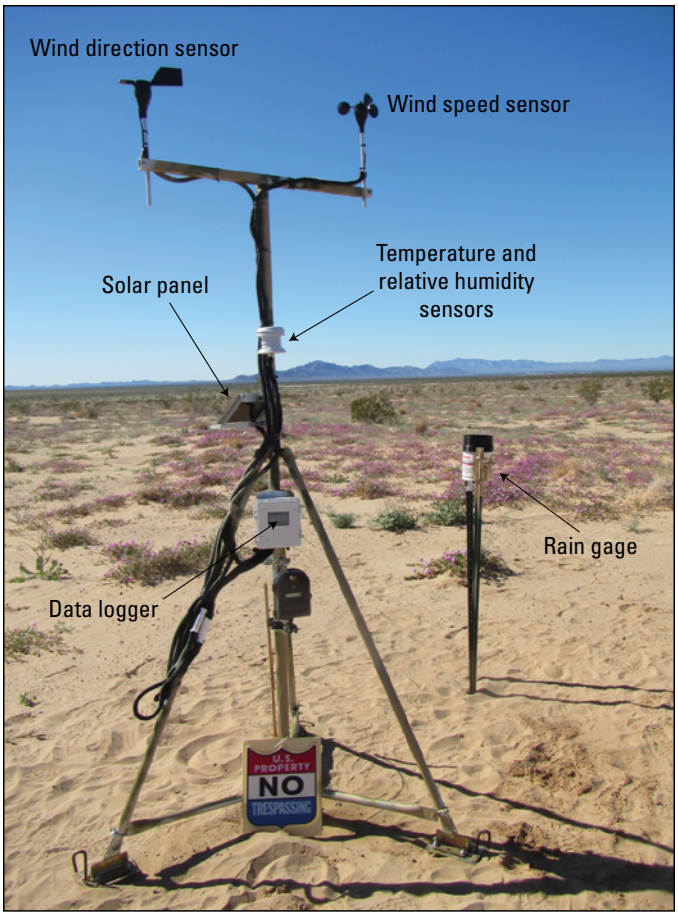

Figure 2. Photograph of a weather station deployed in eastern Chuckwalla Valley on February 7, 2019. U.S. Geological Survey photograph taken February 7, 2019, view facing southwest.

the study duration. The use of a 4-minute interval was intended to allow the highest resolution of wind speed while minimizing the risk that the logger memory would fill between maintenance visits.

Rainfall was recorded on an Onset HOBO RG3-M standalone tipping-bucket rain gage, affixed to a 1-m-high stake approximately 3 m away from the primary tripod (fig. 2). This gage measures rainfall with a resolution of 0.2 millimeter (mm). Data were recorded on a self-contained pendant logger housed within the unit. The gage also records air temperature, with resolution 0.1 °C and accuracy ± 0.5 °C, although because the temperature sensor operated within the aluminum rain-gage housing instead of in its own shaded housing, its temperature measurements are assumed to be over-estimates during daylight (sunlit) hours.

The weather-monitoring equipment operated without telemetry capabilities. The station underwent maintenance, and the data were downloaded during site visits on June 26, September 20, and November 13, 2019, and on March 16, June 1, September 4, and December 21, 2020, at which time the weather station was removed.

Measurements of wind speed and direction were used to calculate vector sums over the entire study duration and for individual months. We also used the 4-minute wind-speed data to model the sand flux that could occur under ideal conditions of unlimited sediment supply (that is, assuming no vegetation-induced inhibition of aeolian sand entrainment). To model sand flux, we applied four aeolian sediment-transport equations (table 1): those of Bagnold (1941), Kawamura, (1951), Zingg (1953) and an equation developed by both Durán and others (2011) and Kok and others (2012), hereafter referred to as the Durán-Kok model. The predictions of any aeolian sediment-transport model are considered to have substantial uncertainty, owing to the inherent difficulty of quantifying the nonlinear relationship between wind speed and sand transport (Bauer and others, 1996). The scientific community has not agreed upon one transport model that performs ideally. We chose these four models because each has robust support in the literature and the use of all four includes a range of approaches and assumptions to infer the sediment-transport rate. The transport equations in table 1 require an estimate of shear velocity, u_*, which we calculated for each 4-minute data point using the Kármán-Prandtl equation (the Law of the Wall):

$$u_* = u(z)\ \kappa / \ln (z/z_0) \quad (1)$$

where

u is wind speed measured at height z,
κ is von Kármán's constant (0.41), and
z_0 is the roughness length.

While calculating u_* and before applying the four models, we chose a roughness length of 0.02 m based on observations of small wind ripples and occasional gravel particles in the vicinity of the weather station. The median grain size (D_{50}) at the weather-station site was 150 micrometers (μm; see Surficial Sediment Characterization section) and so we assigned a threshold wind speed of 2 m/s on the basis of the critical entrainment threshold formulation of Bagnold (1941), which yields a threshold shear velocity (u_{*_t}) of 0.1781 m/s. We assumed sand would become too wet to be entrained by wind if at least 1 mm of rain fell within 1 hour, and that the sand would remain immobile for 6 hours thereafter.

Surficial Sediment Characterization

We characterized surface processes and sedimentary properties in eight polygons (fig. 1*C*) intended to represent a variety of geomorphic settings within the proposed Riverside East Development Focus Area. In each polygon, the sedimentary and geomorphic setting were assessed visually during site visits in February 2019. Orientations of any aeolian geomorphic features were noted, and multiple samples were collected for grain-size analysis.

Sediment grain size was analyzed at the USGS laboratory in Santa Cruz, Calif. Particles coarser than 2 mm were sieved

Table 1. Sediment-transport equations used to model aeolian sand flux.

[u_*, shear velocity; d, grain size (in meters); D, reference grain size (in meters), namely 250 micrometer-diameter sand; u_{*_t}, threshold shear velocity for motion of the grain size considered; ρ_s and ρ, densities of quartz sediment and air, respectively (taken to be 2,650 and 1.2 kilograms per cubic meter; g, gravitational acceleration (9.8 meter per square second). C is a constant from Kok and others (2012) set equal to 5. In that equation, u_* refers to the shear velocity associated with the impact threshold, a similar concept to u_{*_t} in the equation of Kawamura (1951) and several other transport models in the literature]

Reference	Equation for sand flux (q)
Bagnold (1941)	$q = 1.8\left(\frac{d}{D}\right)^{0.5}\frac{\rho}{g}u_*^3$
Kawamura (1951)	$q = 2.78\frac{\rho}{g}(u_* - u_{*_t})(u_* + u_{*_t})^2$
Zingg (1953)	$q = 0.83\left(\frac{d}{D}\right)^{0.75}\frac{\rho}{g}u_*^3$
Kok and others (2012) and Durán and others (2011)	$q = C\frac{\rho}{g}u_{*_{it}}u_*^2\left(1-\frac{u_{*_{it}}^2}{u_*^2}\right)$

using a RO-TAP sieve shaker, and particles finer than 2 mm were analyzed with a Coulter laser particle-size analyzer (LPSA), after organic matter had been removed using a hydrogen peroxide solution. Several months after the samples were analyzed, a problem was discovered with the LPSA that had caused inaccurate measurement of the coarse silt content (sizes approximately 40 to 63 μm). Grain-size distribution of particles coarser than 63 μm was unaffected, and the proportions of silt (4–63 μm) and clay (finer than 4 μm) also were measured accurately. Therefore, these data are reported in the Results section below without defining particle-size distribution between 4 and 63 μm.

Stratigraphic Analysis and Luminescence Dating

We evaluated subsurface profiles at five locations in March 2020 (red circles of fig. 1*C*), describing stratigraphy and sampling sediment in pits excavated with a backhoe. The five pit locations defined a northwest-to-southeast transect along eastern Chuckwalla Valley. Pit 1 was located north of Interstate 10, southwest of the McCoy Mountains at the southeast end of Palen-McCoy valley. Pit 2 was located within polygon 2, several hundred meters west of the weather station and north of the Mule Mountains. Pit 3 was approximately 1 km east of polygon 2, and Pit number 202 was located at the north side of the Mule Mountains. Pit 4, the only exposure that was dug by hand, was within polygon 4, northeast of the Mule Mountains. In each pit, we described and sampled sedimentary units and described the soil profiles. Grain size of sediment samples from these subsurface pits was analyzed by sieving, using sieve sizes ranging from 45 μm to 4 mm.

To estimate the ages of the deposits uncovered during the subsurface excavations, we employed luminescence dating. Luminescence dating is a technique that involves counting the number of electrons stuck in meta-stable states at the molecular scale of common minerals such as quartz and feldspar (for a summary of luminescence geochronology, see Gray and others, 2019). These electrons become stuck in these states at a measurable rate due to natural background ionizing radiation and generally escape only when given energy, such as by exposure to sunlight. As such, a luminescence age effectively measures the time since a mineral grain has been exposed to sunlight. Here, we use a method known as post-infrared infrared-stimulated luminescence (pIRIRSL) on 180–250 μm sand grains of potassium feldspar (Thomsen and others, 2008; Thiel and others, 2011; Li and others, 2014) as the typical optically stimulated luminescence dating used on quartz does not work well in this region due to unfavorable quartz geochemistry (Lawson and others, 2012).

We performed standard sample preparation at the USGS Luminescence Geochronology Laboratory in Denver, Colo., following the procedures of Gray and others (2015). First, we collected samples from each of the five pits by hammering in light-proof stainless-steel tubes into the exposed stratigraphic layers. We extracted and capped the tubes and collected bulk sediment samples for measurement of elemental concentrations of potassium, thorium, and uranium using Inductively Coupled Plasma Mass Spectrometry (ICP-MS) and high-resolution germanium gamma spectrometry using USGS facilities. Dose rates were determined using the Dose Rate and Age Calculator of Durcan and others (2015). Samples were opened under dark-room conditions lit by sodium-vapor amber lamps; water content by weight was measured from the extracted sediment. We extracted feldspar separates by treating the samples with rounds of 5N HCl, 30 percent H_2O_2, sieving to isolate the 180–250 μm size fraction, and performing magnetic and heavy liquid density separations.

To calculate luminescence ages, we used pIRIRSL measurement protocols adapted from Li and others (2014) and Carr and others (2019) using an automated Lexsyg Research luminescence reader fitted with infrared light-emitting diodes and a filter combination centered on 410 nanometers. We first confirmed that all samples had adequate luminescence characteristics by performing dose recovery tests using our protocol on six aliquots with a given beta dose of 16.5 gray. All samples produced successful dose recovery within 5 percent. We then performed fading tests following methods adapted from Auclair and others (2003), irradiating samples with 50 gray of beta dose and holding the samples for 72 hours. All but two samples produced g-values significantly less than 2 percent, so we concluded that any positive g-values represent laboratory artifact and thus no fading correction was performed. Equivalent doses obtained for each aliquot were used to calculate a sample-wide paleodose using the central age model (CAM; Galbraith and Roberts, 2012) and the R-Luminescence package (Kreutzer and others, 2012). We chose the CAM since the aeolian deposits in this location are likely to be well bleached and no suitable modern analog is present in order to apply the minimum age model for non-aeolian sediments (Galbraith and Roberts, 2012).

Results

Weather and Sand-Transport Modeling

Figures 3–8 summarize the weather conditions recorded in eastern Chuckwalla Valley between February 2019 and December 2020. Several of the weather sensors experienced intermittent malfunctions, presumably because high winds interrupted electrical connections. On April 10, 2019, during sustained (4 minute) wind speeds exceeding 10 m/s and gusts of 13–14 m/s, the wind-direction, temperature, and relative-humidity sensors all ceased recording data within several minutes of each other. These sensors remained non-operational until they were repaired on June 26, 2019 (the data gaps on figs. 3–5). Another outage of the temperature and humidity sensor occurred on October 30, 2019, during sustained wind speeds of 13 m/s and concurrent gusts of as much as 18 m/s; that sensor was repaired, and data collection resumed on November 13, 2019 (figs. 4, 5). The temperature and humidity sensor malfunctioned again on June 1, 2020, and was replaced with a new sensor the following day. That sensor failed during strong winds (14 m/s gusts) on September 8, 2020, and remained inactive for the rest of the study interval.

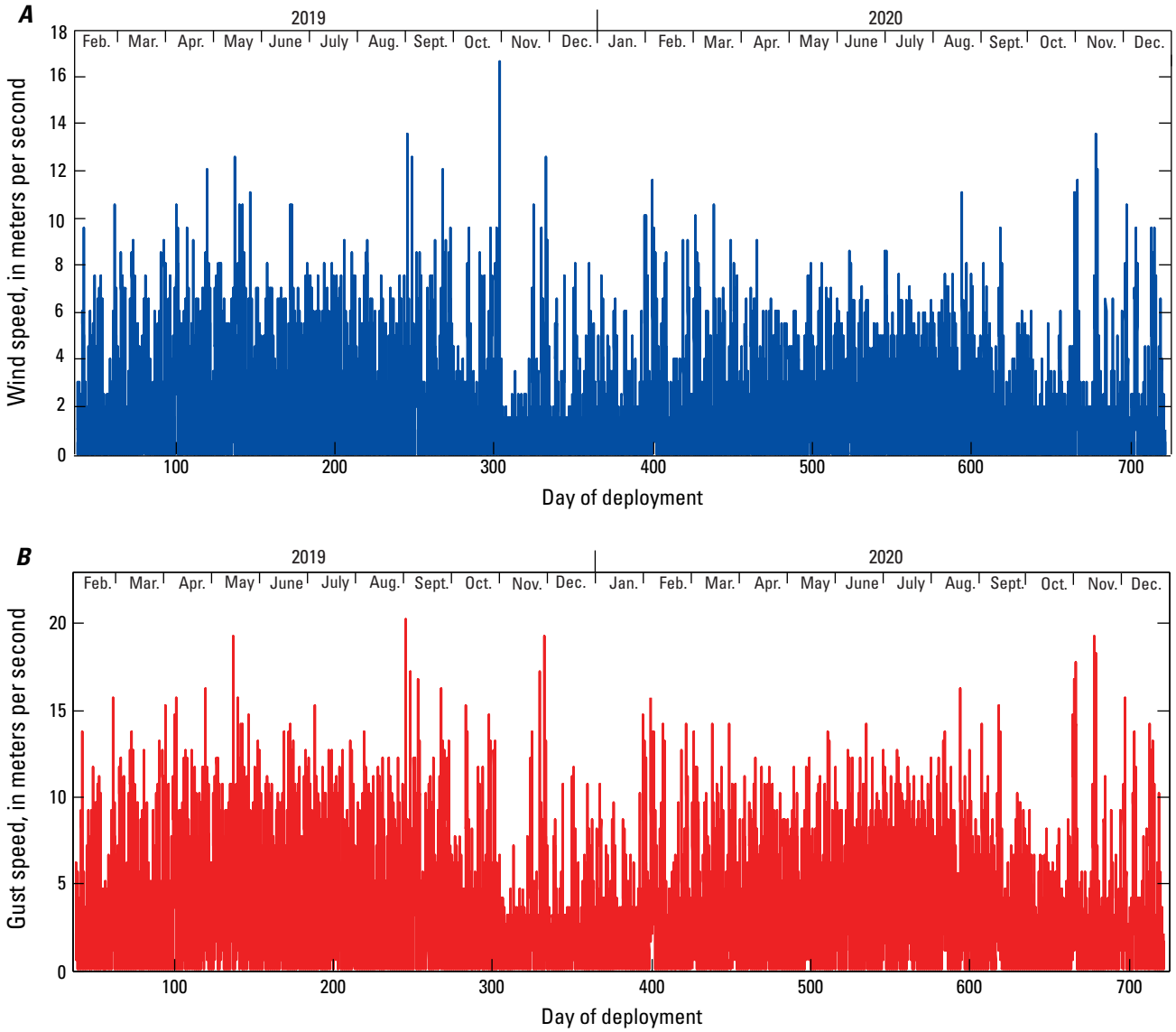

Figure 3. Graphs of wind speed, plotted as 4-minute average values (*A*), and maximum gust speed in each 4-minute interval (*B*), for the study duration beginning on February 7, 2019, and ending December 21, 2020.

The recorded weather data (figs. 3–5) generally conformed to expected, previously measured patterns for the southwestern U.S. drylands and to those measured at the Blythe airport, 8 km west of the town of Blythe (National Oceanic and Atmospheric Administration, 2020b). Wind speeds measured at our station commonly were highest in the spring (fig. 3), with 4-minute average values greater than 10 m/s on multiple occasions. Daytime temperatures were greater than 40 °C in summer and were usually 10–20 °C during winter. The spring windy season was accompanied by little rain (similar to patterns observed by, for example, Draut and Rubin, 2008, and Draut and others, 2012). Winter 2019 was dry, and only 2.8 mm of rain fell between the time of instrument deployment in early February and the onset of the typically dry spring and early summer. The summer monsoon season of 2019 (July to late September) brought less than 5 mm of rain to this site, and the 2020 summer monsoon brought none at all (fig. 5*B*). Major spatial variability in rain was evident. For example, during February 13–15, 2019, an extreme atmospheric-river storm brought record-setting atmospheric moisture to southern California (Hatchett and others, 2020), including more than 130 mm of rain in western Riverside County that caused widespread flooding (Guilinger and others, 2020). Our weather station in eastern Riverside County recorded only 1.4 mm of rain during that storm. The most substantial rainfall recorded at this station occurred on March 10–12, 2020, when 32.4 mm of rain fell.

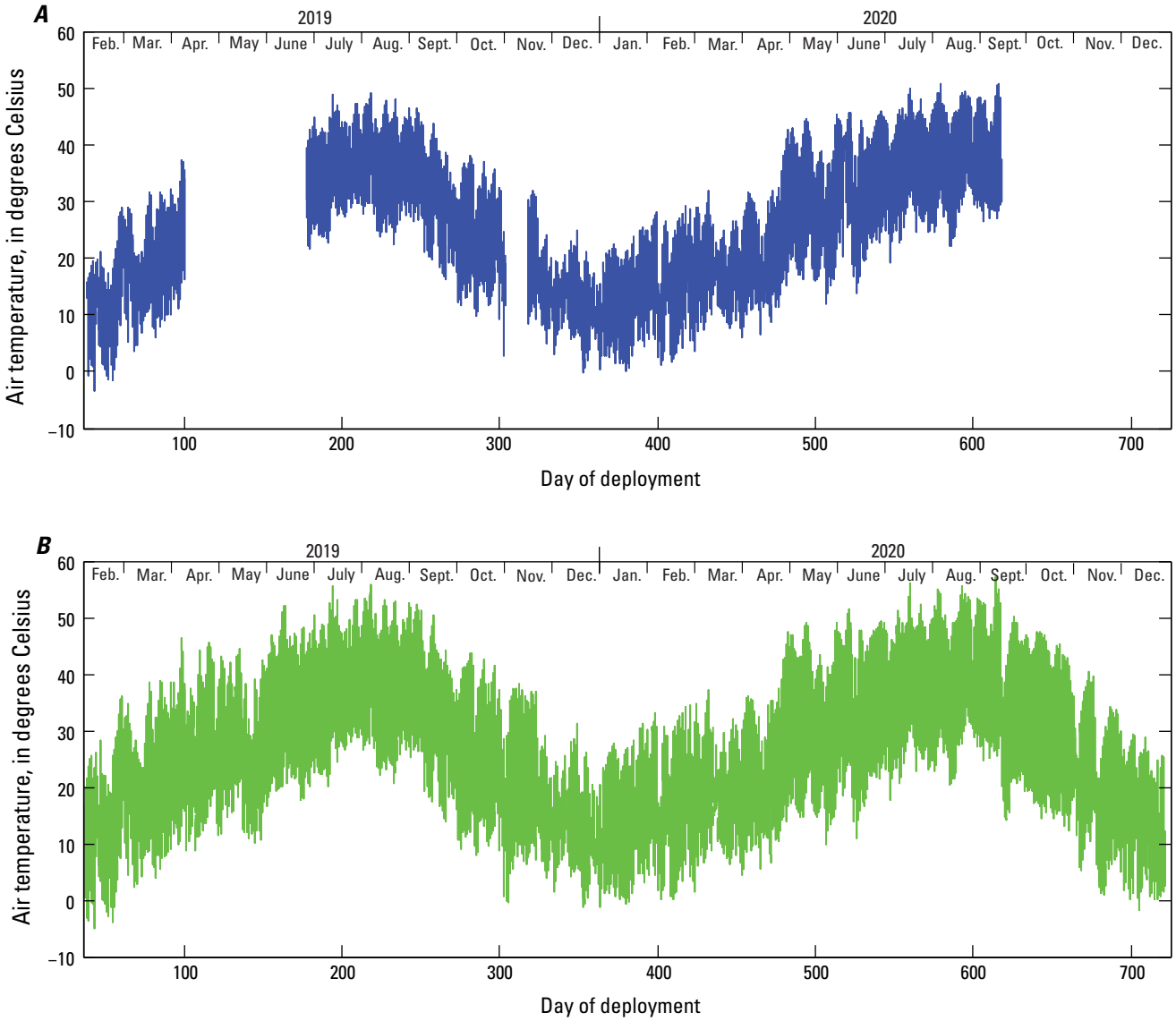

Figure 4. Graphs of air temperature measured using the sensor mounted on the main weather-station (*A*) and a sensor within the aluminum tipping-bucket rain gage (*B*; see fig. 2 and text for description of setup). Data gaps in *A* occurred over several intervals after electrical connections were disrupted during strong wind events.

Wind directions were commonly from the southwest (usually ranging from south-southwest to west-southwest), although seasonal variability was apparent (figs. 6–8). Monthly vector sums of wind magnitude and direction indicated wind blew from between 180 (due south) and 270 degrees (due west) in most months for which wind-direction data were collected (table 2). A notable wind event that consisted of strong northwesterly winds occurred during October 30–31, 2019. Those high winds were preceded by several days (October 27–28) of moderately strong winds (4–9 m/s) from the southwest, but the October 30–31 event included sustained winds above 15 m/s and gusts as strong as 22 m/s from the north-northwest (fig. 9). That northwesterly wind event developed suddenly, and wind speed increased from 0 to consistently above 10 m/s within 30 minutes. No decrease in temperature accompanied the arrival of strong north winds, indicating the event was likely not caused by a cold front. The October 30–31, 2019, northwesterly wind event reshaped local sedimentary features and formed sand shadows (some as tall as 30–40 cm) in the lee sides of rocks and vegetation (fig. 9) where no strong geomorphic indicators of wind direction had been present on earlier site visits. Similar rapidly developing, strong, dry northerly winds were recorded over September 8–10, 2020, and December 12–13, 2020, that again reshaped sand shadows around the weather-station location to reflect that wind direction. At other times, particularly in fall, strong and dry wind events were recorded coming from the southwest, northwest, and occasionally southeast (figs. 6, 7).

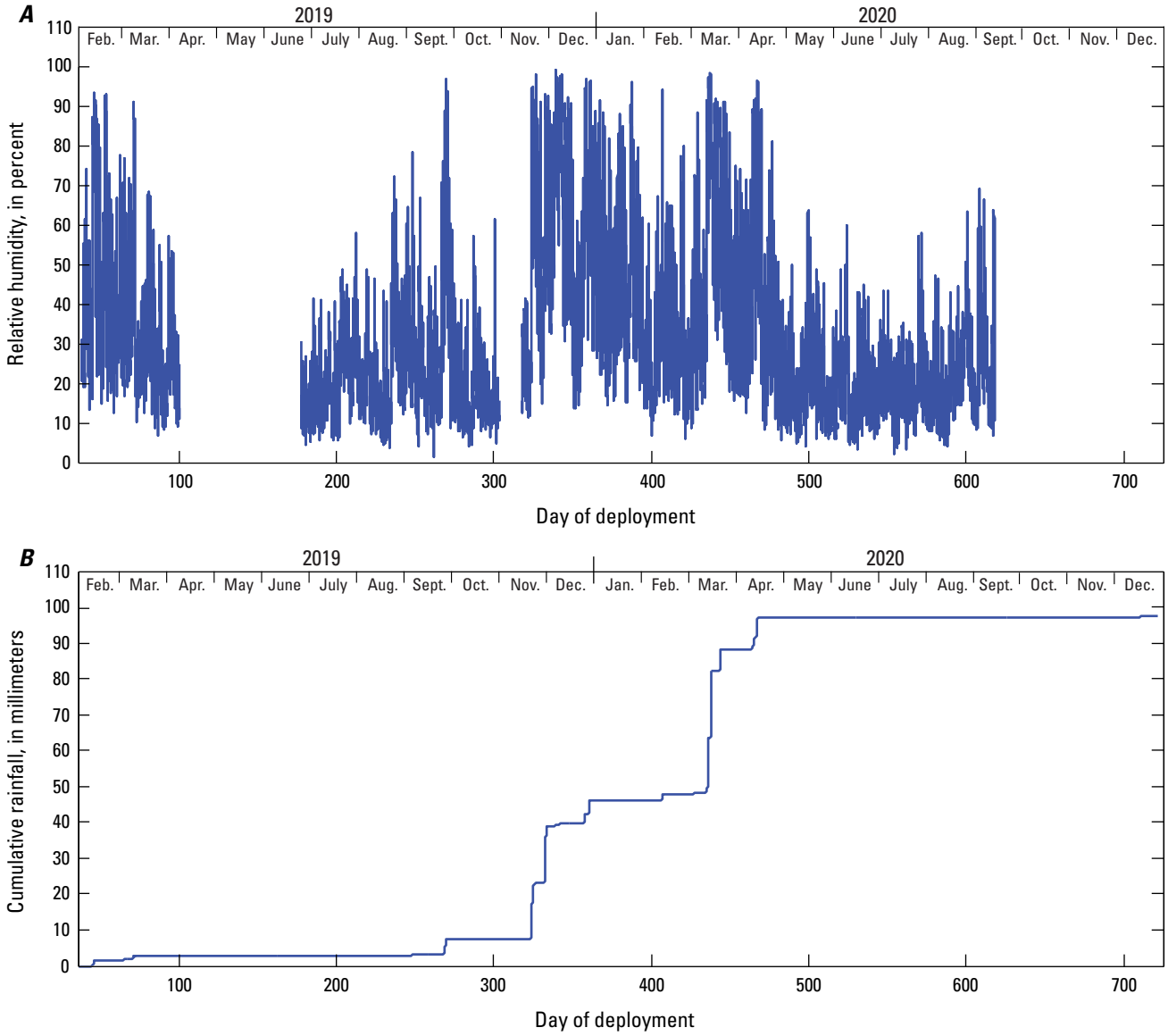

Figure 5. Graphs of relative humidity (*A*), including the same data gaps as in figure 4*A*, and cumulative rainfall (*B*) during the study interval. Data gaps in *A* occurred over several intervals after electrical connections were disrupted during strong wind events.

Table 2. Vector sums of wind speed (4-minute averages) and direction, by month.

[Due to sensor malfunction, wind directions were not recorded between April 10 and June 26, 2019; NA, not available. Wind speed is reported in meters per second and wind direction in degrees azimuth, which refers to the direction from which the wind blew. The magnitudes in this table can be used to compare relative strength (directionality) by month, but because they are vector sums, do not represent instantaneous wind speeds]

Month and year	Magnitude	Direction
February 2019	5,165	226
March 2019	8,533	239
April 2019	24,522	197
May 2019	32,693	NA
June 2019	23,583	189
July 2019	23,938	182
August 2019	17,511	182
September 2019	13,311	185
October 2019	6,212	315
November 2019	3,376	186
December 2019	4,519	288

Month and year	Magnitude	Direction
January 2020	3,927	310
February 2020	5,998	319
March 2020	13,223	209
April 2020	10,786	211
May 2020	12,852	198
June 2020	14,573	184
July 2020	17,334	181
August 2020	18,398	184
September 2020	2,111	182
October 2020	2,852	294
November 2020	6,698	239
December 2020	5,544	339
Entire study duration:	195,180	201

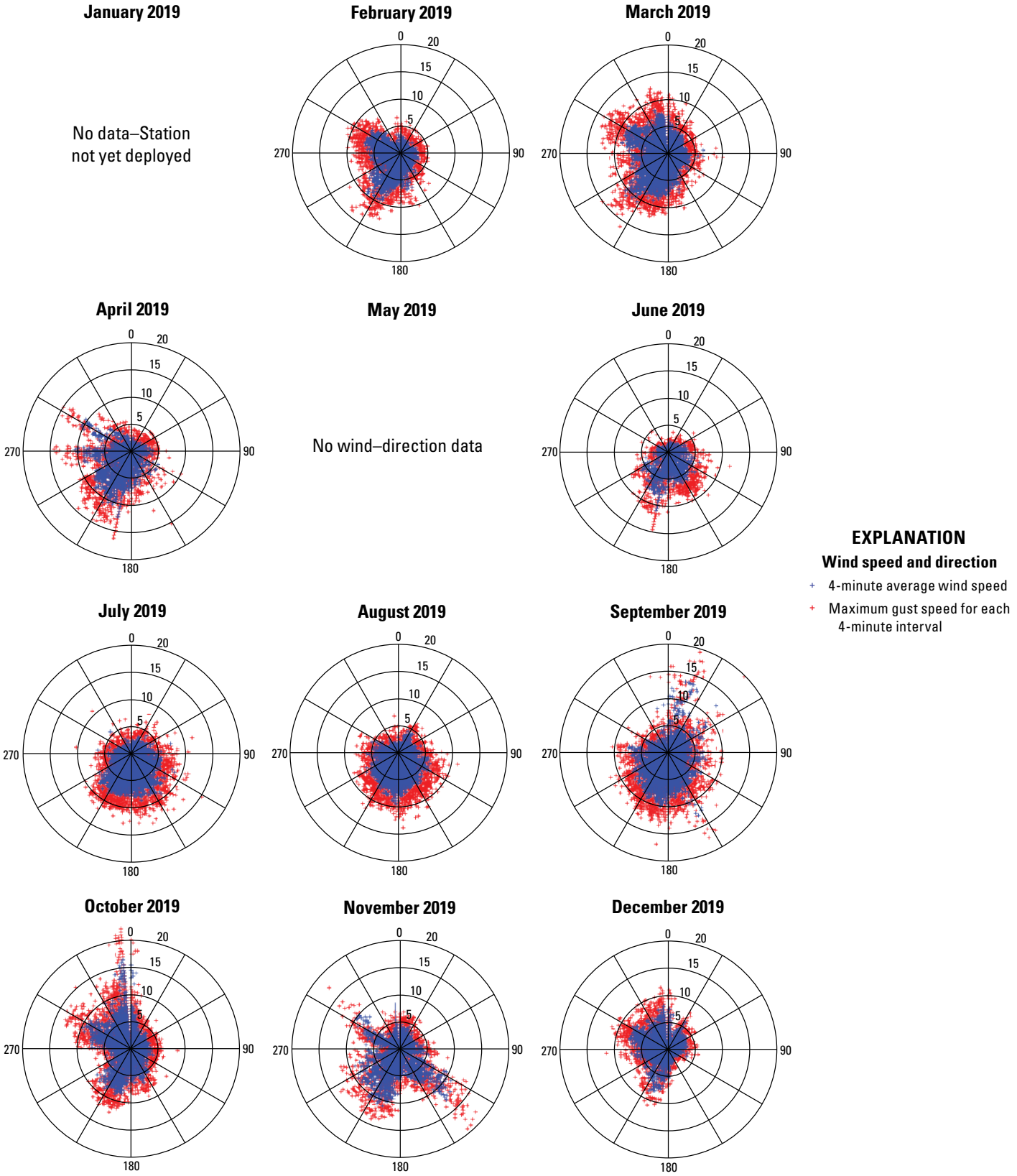

Figure 6. Polar plots of wind speed (in 0 to 20 meters per second from the center to the perimeter of the circle, respectively) and wind direction (in degrees azimuth; shown radially along circle's perimeter) for each month of 2019. January data are absent because data collection began on February 7. Blue symbols represent 4-minute average wind speed, and red symbols represent maximum gust speed for each 4-minute interval. No data are shown from April 10 to June 26, 2019, or from October 30 to November 13, 2019, owing to malfunction of the wind-direction sensor. The sensor used had a measurement range of between 0 and 355 degrees, and so does not resolve wind direction within 5 degrees west of north.

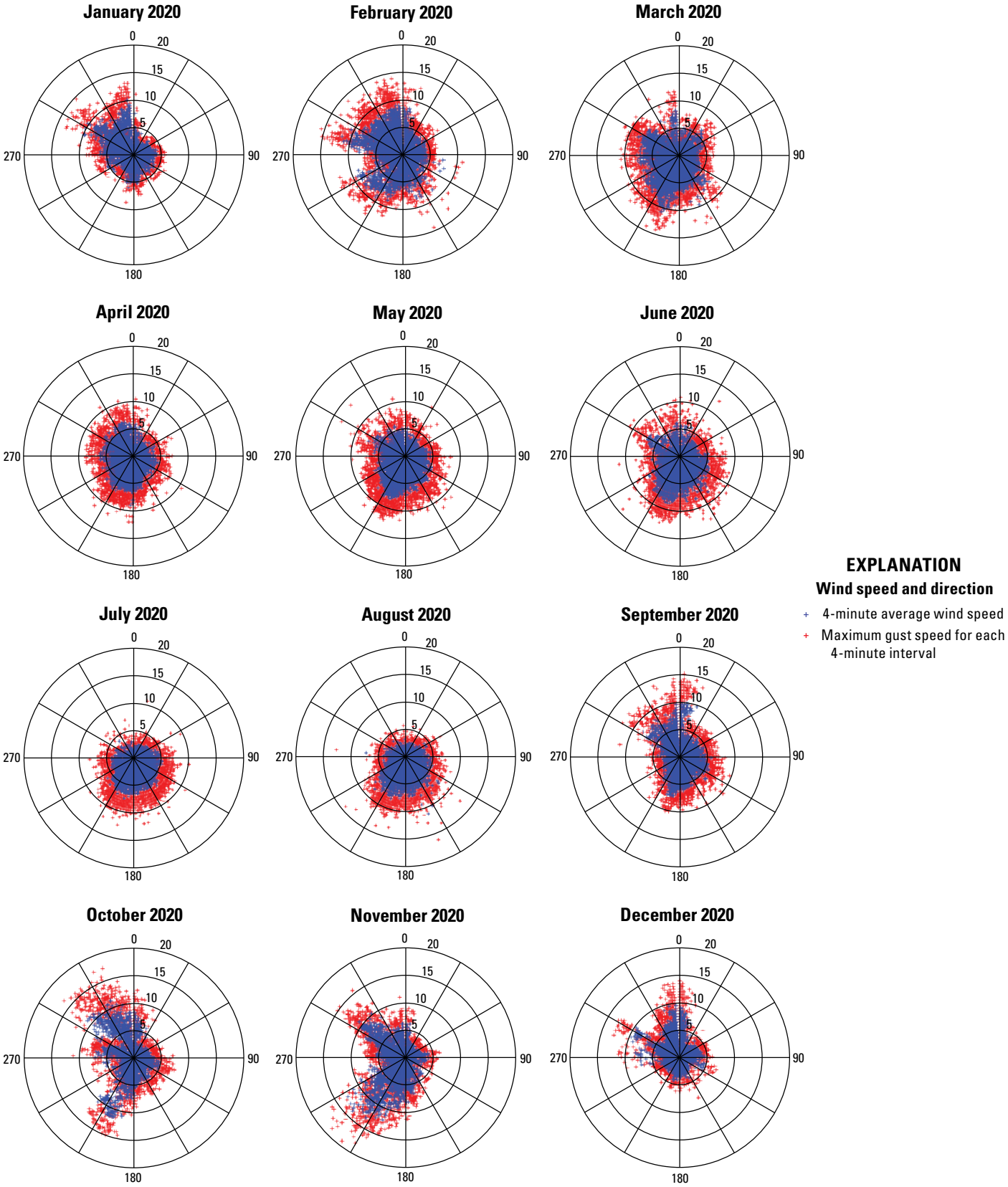

Figure 7. Polar plots of wind speed (in 0 to 20 meters per second from the center to the perimeter of the circle, respectively) and wind direction (in degrees azimuth; shown radially along circle's perimeter) for each month of 2020. Blue symbols represent 4-minute average wind speed, and red symbols represent maximum gust speed for each 4-minute interval. The sensor used had a measurement range of between 0 and 355 degrees, and so does not resolve wind direction within 5 degrees west of north.

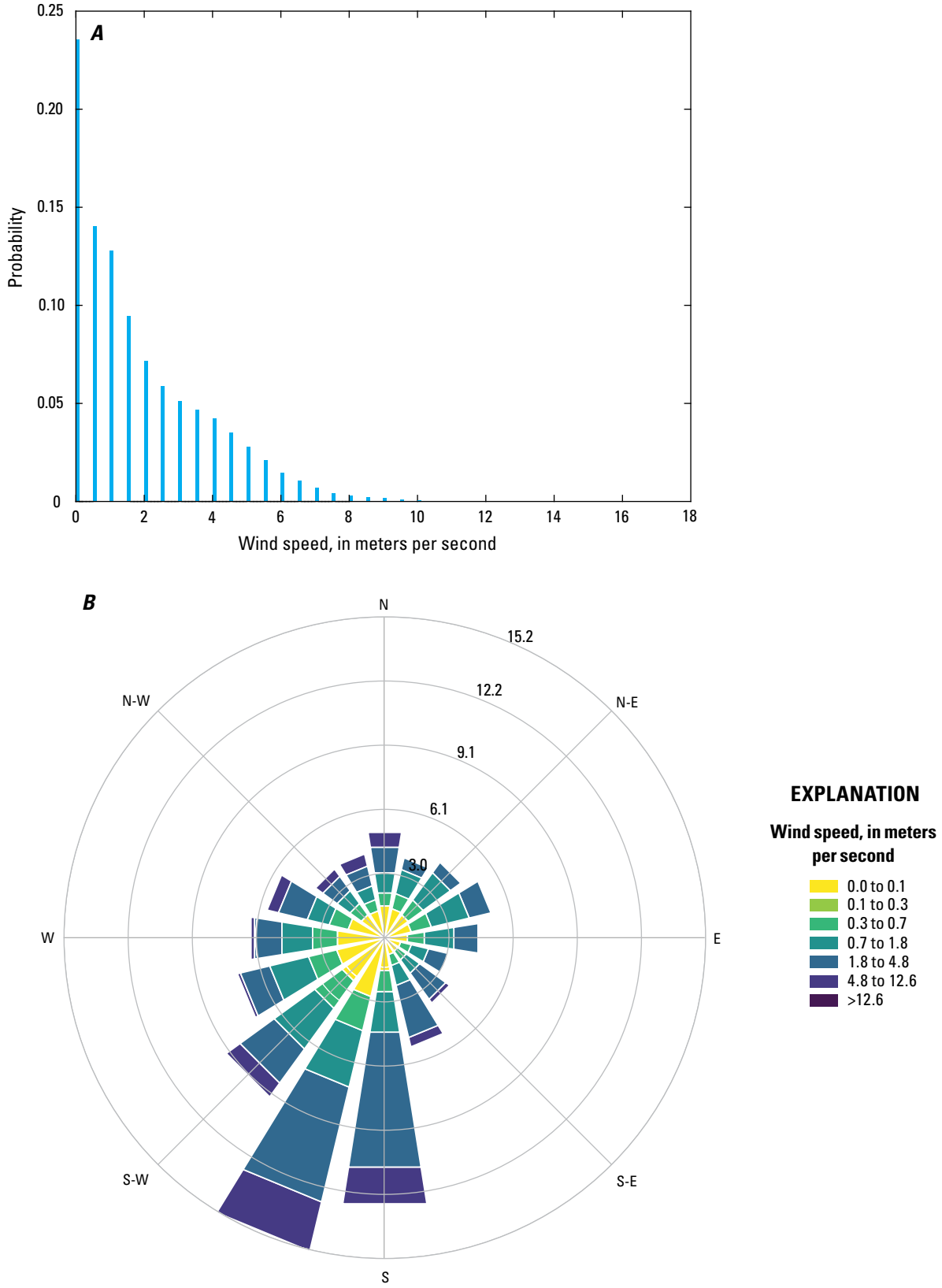

Figure 8. Histograms of 4-minute average wind-speed measurements for the entire study duration (February 2019 through December 2020). *A*, Relative frequency histogram showing the probability of wind speed (in meters per second). *B*, Wind-rose histogram showing wind speed frequency by direction. The stacked color-filled boxes show relative frequency of each windspeed from a given direction, whereas the length of the bar shows the relative frequency of a wind direction. Wind-rose histogram made with Windrose for Python 3.4 (Roubeyrie and Celles, 2018).

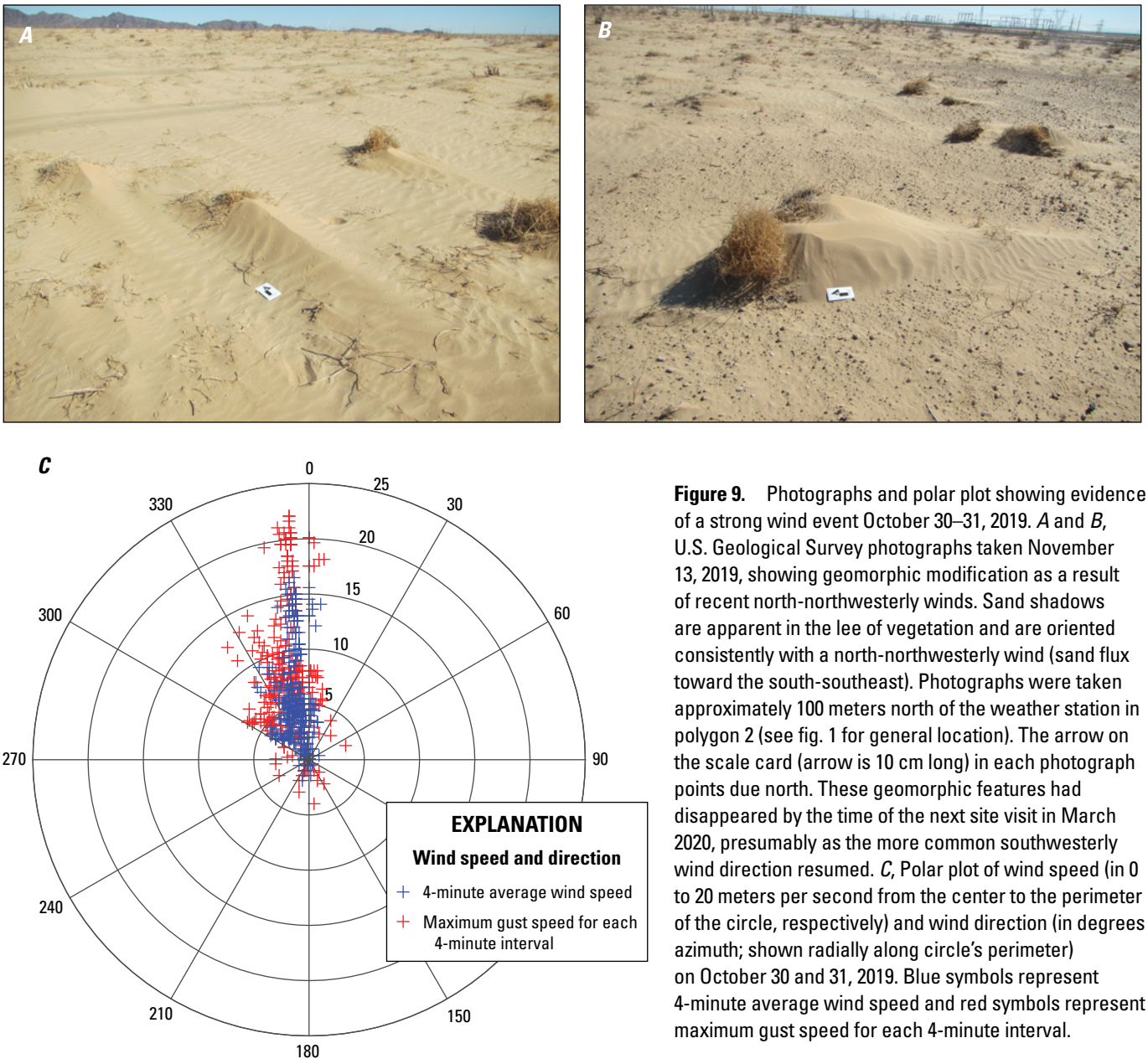

Figure 9. Photographs and polar plot showing evidence of a strong wind event October 30–31, 2019. *A* and *B*, U.S. Geological Survey photographs taken November 13, 2019, showing geomorphic modification as a result of recent north-northwesterly winds. Sand shadows are apparent in the lee of vegetation and are oriented consistently with a north-northwesterly wind (sand flux toward the south-southeast). Photographs were taken approximately 100 meters north of the weather station in polygon 2 (see fig. 1 for general location). The arrow on the scale card (arrow is 10 cm long) in each photograph points due north. These geomorphic features had disappeared by the time of the next site visit in March 2020, presumably as the more common southwesterly wind direction resumed. *C*, Polar plot of wind speed (in 0 to 20 meters per second from the center to the perimeter of the circle, respectively) and wind direction (in degrees azimuth; shown radially along circle's perimeter) on October 30 and 31, 2019. Blue symbols represent 4-minute average wind speed and red symbols represent maximum gust speed for each 4-minute interval.

Modeled sand fluxes, calculated using the four transport equations in table 1, were on the order of 10^5 kilograms (100 metric tons) per meter width per year (fig. 10). The calculated sand flux shown in figure 10 incorporates the assumption that sand would be entrained and transported by wind only when dry (sand was considered too wet to move if at least 1 mm of rain fell within 1 hour, and for 6 hours thereafter). This assumption required removing wind data for parts of 12 days from consideration in the modeling exercise. Removing the presumed wet conditions had a negligible effect on calculated sand flux; for each of the four models, the sand flux over dry intervals differs from the sand flux calculated over the entire study interval (dry and wet) by one percent or less. The modeled fluxes (average of the values produced by the four models) indicate that the October 30–31, 2019, northerly wind event could have mobilized as much as 4,860 kilograms of sand per meter width within 10 hours, assuming unlimited sand supply. The dominant direction of sand flux (the average value of the four model results for each 4-minute data point) was calculated to be toward the northeast (fig. 11), which is a response to sand-mobilizing wind that blows frequently from the southwest.

Surficial Sediment Characterization

Visual observations and grain-size analyses were used to characterize surface morphology and local sedimentary processes for eight polygons and the southeastern part of the Palen dune field (fig. 1), as shown in figures 12–20. Sediment particle size is shown graphically in figures 12–16 and figures 18–20 without

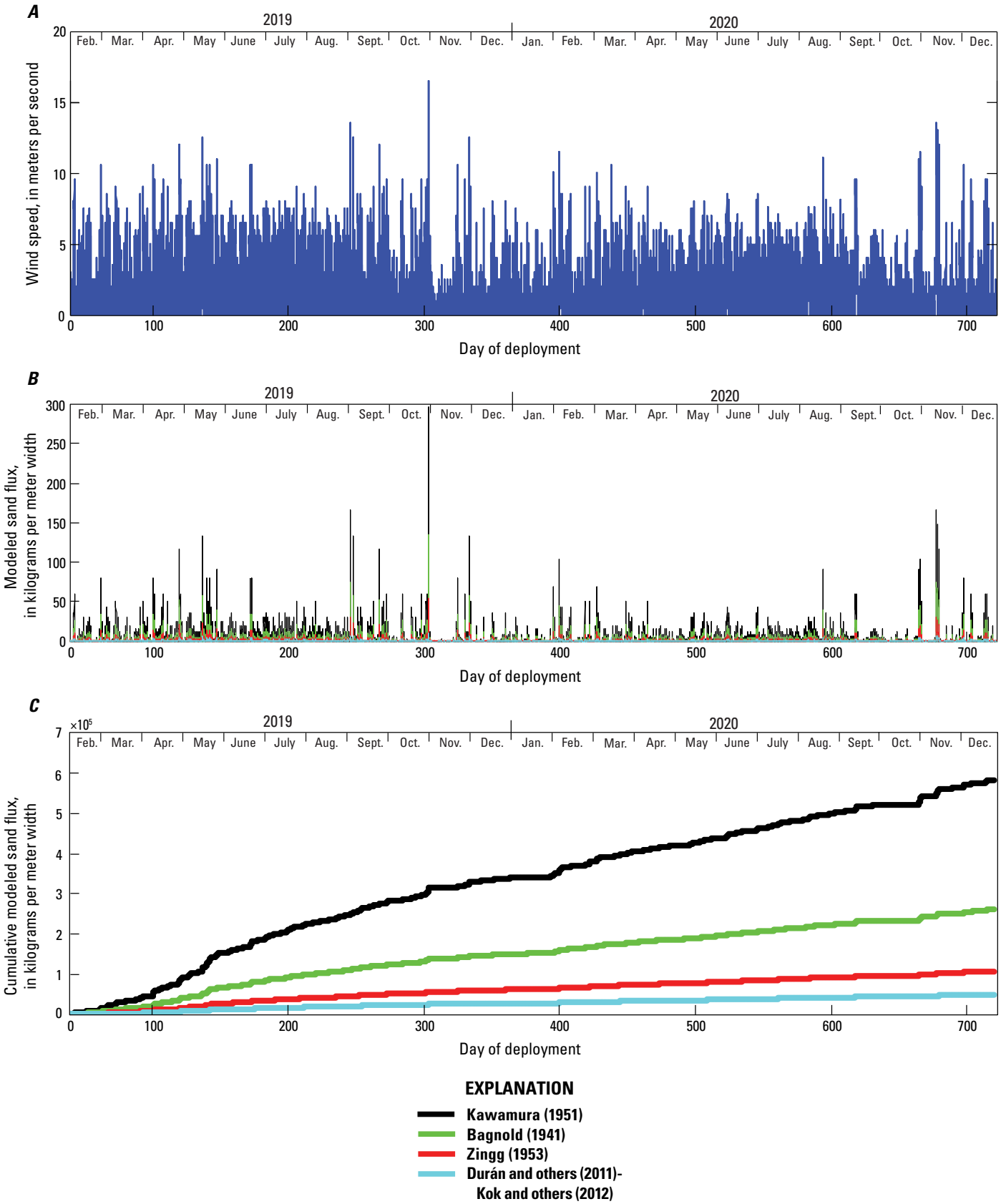

Figure 10. Graphs of wind speed, modeled sand flux, and cumulative modeled sand flux for the duration of the study. *A*, Graph of wind speed, as 4-minute average values (see also fig. 3*A*). *B*, Time-series graph of modeled sand flux in kilograms per meter width, at 4-minute resolution, calculated using the aeolian sand-transport equations in table 1 for time when the sand is presumed to have been dry. *C*, Graph of cumulative sand transport during dry conditions throughout the study duration.

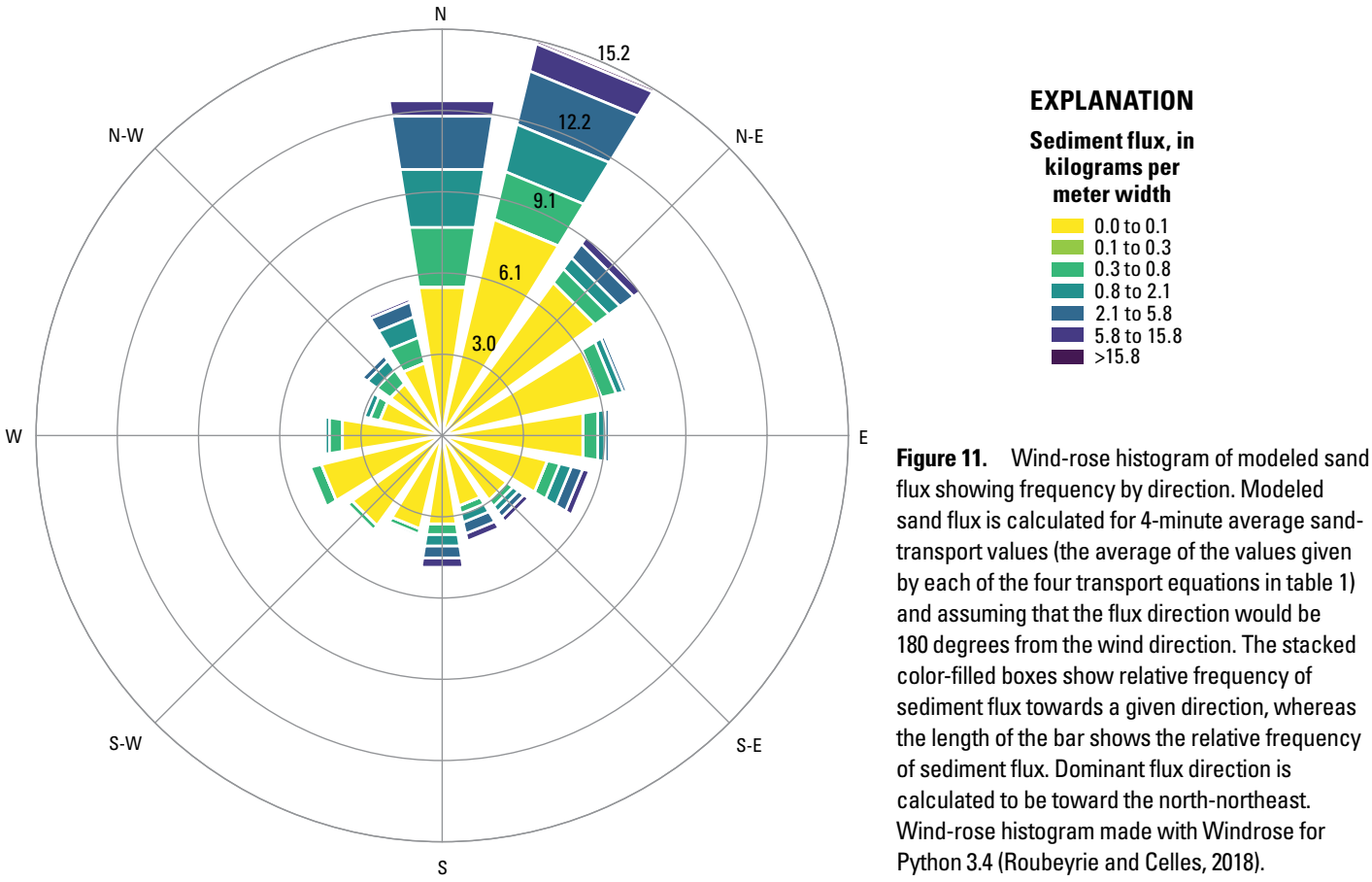

Figure 11. Wind-rose histogram of modeled sand flux showing frequency by direction. Modeled sand flux is calculated for 4-minute average sand-transport values (the average of the values given by each of the four transport equations in table 1) and assuming that the flux direction would be 180 degrees from the wind direction. The stacked color-filled boxes show relative frequency of sediment flux towards a given direction, whereas the length of the bar shows the relative frequency of sediment flux. Dominant flux direction is calculated to be toward the north-northeast. Wind-rose histogram made with Windrose for Python 3.4 (Roubeyrie and Celles, 2018).

defining the distribution between 4 and 63 µm (shown as a straight line in each plot), owing to the aforementioned LPSA problem. In general, surface morphology in the study area consisted of sparsely vegetated sand sheets that contain local areas of active aeolian dunes, as well as distal portions of alluvial fans draining the Mule Mountains and McCoy Mountains. We observed localized field evidence for recent aeolian sediment transport (wind ripples, sand shadows, and active barchanoid dune morphology). Although no flowing or standing water was present during our site visits, we noted mud cracks that indicated the earlier presence of standing water in some areas. Fluvial ripples in surface sediment indicated recent surface-water flow in several ephemeral stream channels. Conditions in each polygon are described below.

Polygon 1, at an elevation of 127 m, included part of the depocenter where the ephemeral channel Wiley Well wash delivers runoff occasionally (fig. 12). Local morphology did not consist of clearly defined alluvial channels at the time of our visits in 2019 and 2020, but we observed many areas that contained dried mud cracks in playa-like fine-sediment deposits, indicating the former presence of standing water (fig. 12*A*). Surface sediment was predominantly sand, and the surface was generally flat except where the sand formed mounds centered around creosote bushes. Creosote-centered sand mounds were a common feature in most polygons we examined and probably represent small coppice dunes or nebkhas, which form as windblown sand accumulates around vegetation while the plant grows. The morphology of these coppice dunes suggests neither recent deflation nor inflation. Evidence for recent deflation would have included exposed plant roots, and recent inflation (accretion) would have been inferred from partial burial of living vegetation, but neither was observed in polygon 1. Evidence for erosional modification (blowout) of older aeolian deposits leaving a mounded remnant deposit would normally include exposures of aeolian sedimentary structures along the edges of the mound, which also was not clearly apparent in polygon 1. Evidence of recent aeolian sand activity was rare, although wind-rippled sand occurred in small, uncommon patches. Sediment samples consisted of well-sorted fine to medium sand, with the exception of sample 1-2, which was finer material from a mud-cracked, playa-like surface (fig. 12*C*). Vegetation in polygon 1 was dominated by creosote bushes, *Plantago ovata*, and *Cryptantha* sp. Burrows of unidentified animals were common, including one large (greater than 15 cm across), bifurcating burrow in sand. The surface morphology and vegetation showed little spatial variability within the polygon.

Polygon 2, including the area surrounding our weather station (elevation 135 m), is within a large sand sheet east (downwind) of Wiley Well wash (figs. 1, 13). The polygon 2 landscape is more sparsely vegetated than that of polygon 1. The land surface is flat and has alternating wind-rippled sand accumulations and coarser-grained lag deposits. Dune morphology is rare, but in February 2019 we observed several low-relief dunes (less than 1 m high) southwest of the weather station. Active sand transport was evident

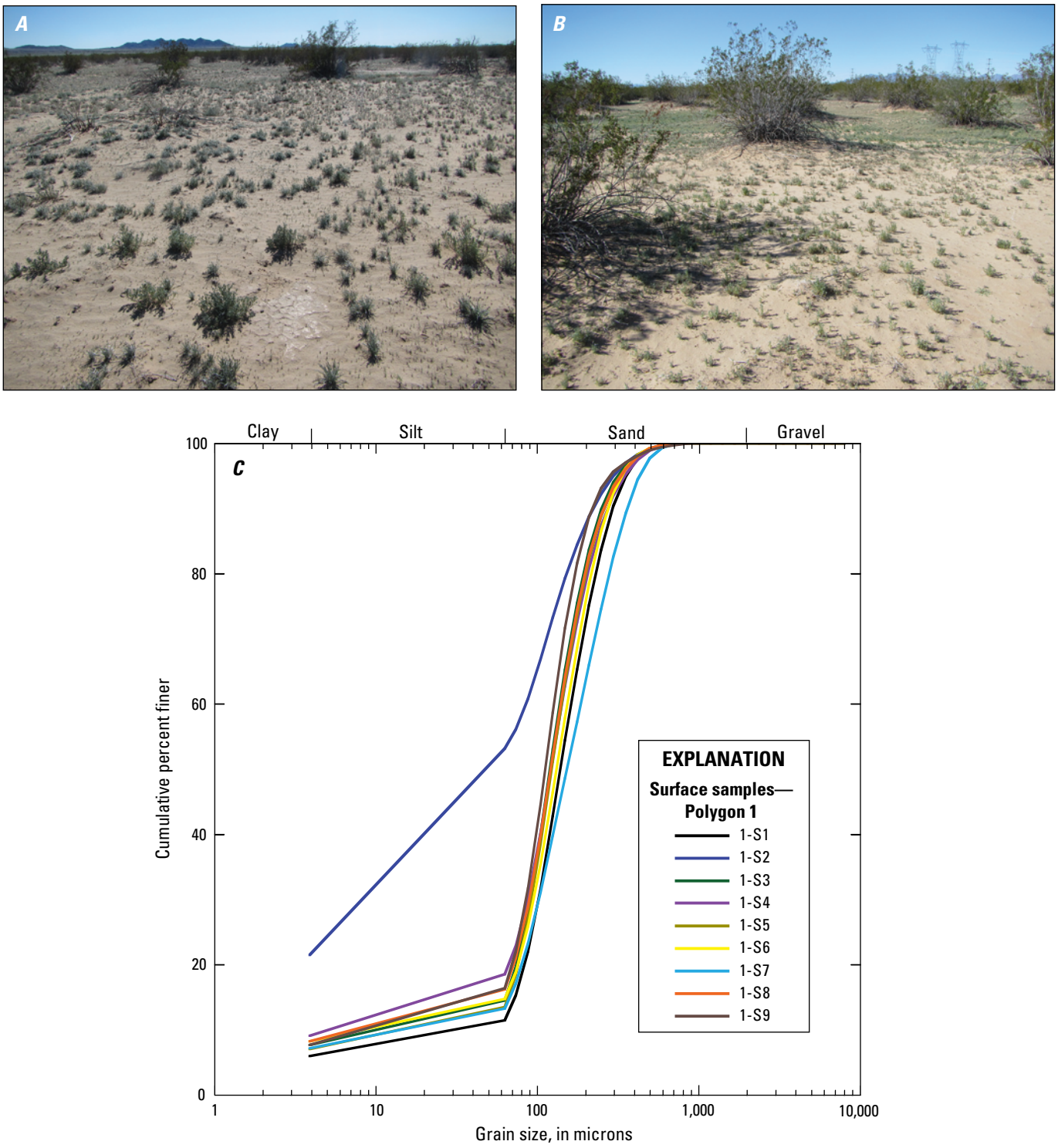

Figure 12. U.S. Geological Survey photographs (taken February 7, 2019) of the land surface in polygon 1 and grain-size graph of samples collected from polygon 1 in February 2019 (see fig. 1 for location). *A* and *B*, Photographs showing vegetation growing on a sand-dominated surface. Faint mud cracks are visible in the foreground of *A*, and small coppice dunes are visible at the base of creosote bushes in *B*. *C*, Grain-size graph of samples 1-S1 through 1-S9. Sample 1-S1 represents a sand-rich region without creosote-centered coppice dunes or evidence of recent water ponding. Sample 1- S2 was collected from a playa-like surface with mud cracks that indicated water ponding. Sample 1- S3 was from a coppice dune around a creosote bush (similar to *B*). Sample 1-S4 was from a playa-like surface with mud cracks. Sample 1-S5 was from a sandy, flat area with a large animal burrow. Sample 1-S6 was from a coppice dune around a creosote bush. Sample 1-S7 was within faintly wind-rippled sand. Sample 1-S8 was collected at the edge of a creosote-centered coppice dune surrounded by faintly wind-rippled sand. Sample 1-S9 was from a large creosote-centered coppice dune.

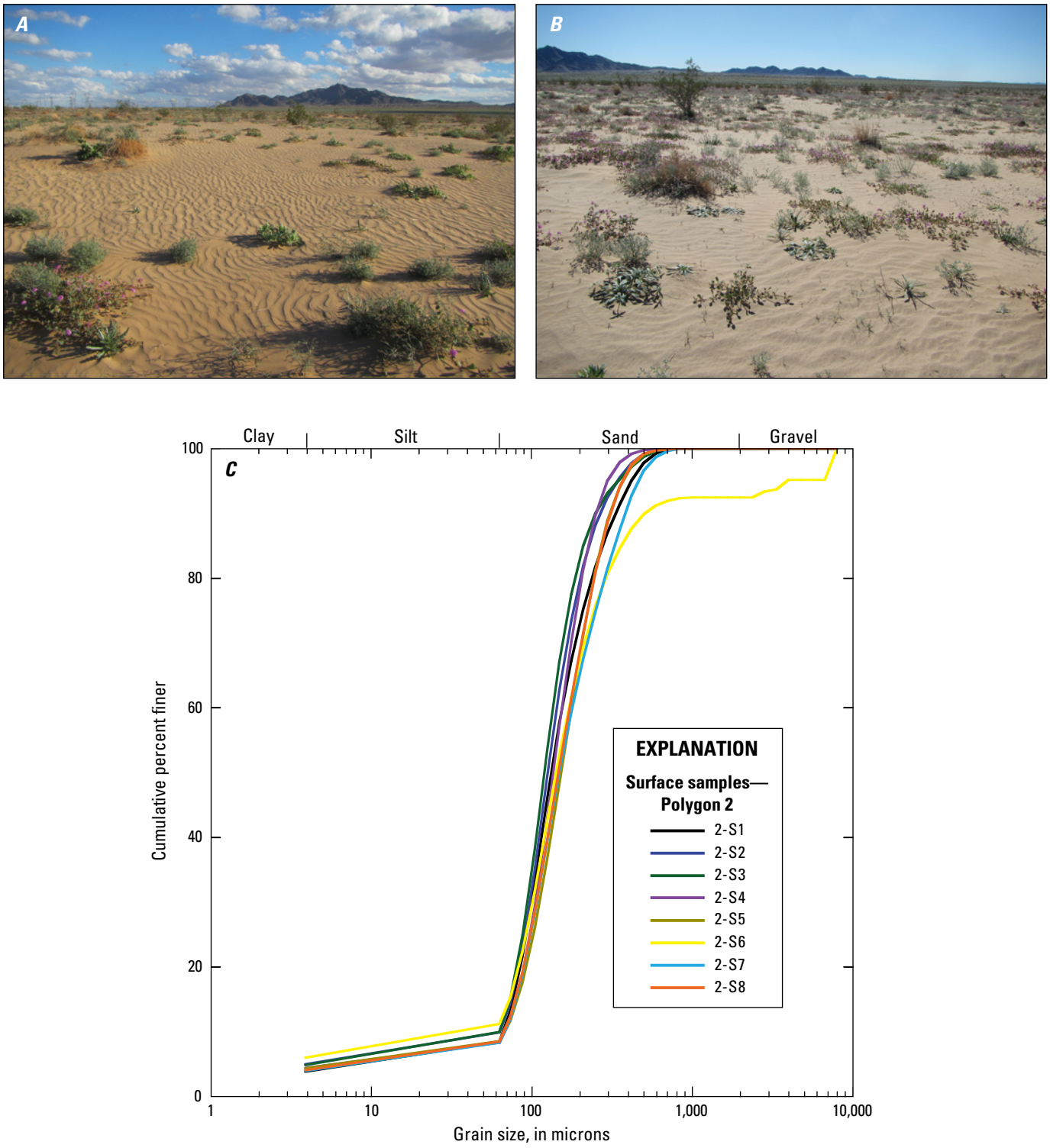

Figure 13. U.S. Geological Survey photographs of the land surface in polygon 2 (near the weather station) taken on February 5, 2019, and grain-size graph of samples collected from polygon 2 in February 2019 (see fig. 1 for location). *A*, Photograph showing sparsely vegetated and wind-rippled sand (facing southeast, showing the Mule Mountains in the background). *B*, Photograph showing sparsely vegetated, wind-rippled sand in polygon 2, facing south, with the western part of the Mule Mountains in the background. *C*, Grain-size graph of samples 2-S1 through 2-S8. Sample 2-S1 was collected at the weather station. Sample 2-S2 was collected from an aeolian lag deposit immediately west of the weather station. Sample 2-S3 was from a bare sand patch measuring approximately 30 square meters Sample 2-S4 was collected from a sandy, creosote-centered mound. Sample 2-S5 was from a wind-rippled surface approximately 5 m west of a small active dune. Sample 2-S6 was within an interdune lag deposit. Sample 2-S7 was within wind-rippled sand. Sample 2-S8 was within wind-rippled sand.

from rippled surfaces on the dunes, but the dune morphology was not well developed. During most site visits geomorphic wind-direction indicators were not well developed, although we did observe small sand shadows (5 cm high or less) in February 2019 indicating recent sand transport toward the northeast. A notable exception was the presence of prominent south-pointing sand shadows shortly after the strong northwesterly wind event in late October 2019 (fig. 9). These features, some as tall as 40 cm and more than 1 m long, were observed on November 13, 2019, but were no longer present in March 2020 after being presumably erased by the more common southwesterly winds. Local deflation and inflation occurred at the weather station; we observed that the rebar rods supporting the tripod feet were exposed and reburied by aeolian sand, indicating bed-elevation changes of 10–20 cm over time scales of months. Minor coppice-dune accumulation was noted around some of the larger creosote bushes in polygon 2. Other geomorphic indicators of long-term deflation or inflation were not observed in polygon 2. Eight sediment samples analyzed from polygon 2 consisted of well-sorted fine to medium sand; sample 2-S6, an interdune lag deposit, contained some coarser material (fig. 13*C*). Given the dominant wind direction (southwest to northeast) and the tendency for ephemeral stream channels to supply aeolian sand to locations downwind (for example, Clarke and Rendell, 1998), we inferred that the area of polygon 2 likely receives windblown sediment supply from Wiley Well wash and its depocenter. Animal burrows are common in polygon 2, including some greater than 10 cm in diameter. Vegetation includes sparse creosote, abundant sand verbena, *Plantago ovata* (desert plantain), and exotic Sahara mustard and Russian thistle.

Polygon 3 is located east of polygon 2 and farther downwind from Wiley Well wash, the largest nearby source of fluvially derived sediment (fig. 1). We inferred that sediment is removed from the wash by wind and reaches the sand sheet to the east by aeolian transport; however, less sand would reach the location of polygon 3 than polygon 2. The land surface of polygon 3 (elevation 125 m) has little geomorphic variation and exposes fine to medium gravel (fig. 14). Gravel clasts on this surface consist of predominantly metamorphic material interpreted as a distal deposit of an alluvial fan from the Mule Mountains and a minor component of well-rounded chert clasts. Sediment immediately below the surface was substantially finer-grained (fig. 14*B*). We interpreted the surface to reflect a combination of aeolian and alluvial deposition that was modified by wind into a lag deposit. Coppice dunes were present around creosote bushes (finer material than the gravel lag; fig. 14*C*). Given its position farther east of Wiley Well wash and the lack of wind-rippled sand surfaces in polygon 3, we interpreted polygon 3 to be an area with less aeolian sediment supply than polygon 2. Vegetation in polygon 3 included creosote bushes and low-lying forbs and grasses.

Polygon 4 is south-southeast of polygon 3, on the northeast side of the Mule Mountains at elevation 115 m, and is not near any obvious source of abundant aeolian sediment supply (fig. 1*C*). The landscape at polygon 4 resembles that of polygon 3 in being a flat, uniform exposure of gravel and sand and consisting of low-relief, creosote-centered coppice dunes (fig. 15*A*). Similar to polygon 3, fine to medium gravel at the surface in polygon 4 indicates a lag deposit formed by wind reworking of material deposited by alluvial fan activity and by aeolian deposition. Occasional small exposures of faintly wind-rippled sand were present (fig. 15*B*). The dominant particle size in all samples was fine to medium sand, with gravel also present in the lag deposit (samples 4-S2 and 4-S4; fig. 15*C*). Clasts in the lag surface included many well-rounded chert pebbles. Vegetation in polygon 4 included creosote, burrobush, and annual forbs. Animal burrows were noted, a burrowing owl was seen in the southern part of the polygon in March 2020, and coyote tracks were present in 2019.

Polygon 5 is due south of polygon 4 and east of the Mule Mountains, on the distal part of an alluvial fan at elevation 115–118 m (fig. 1*C*). The land surface within polygon 5 slopes gently eastward. In addition to the alluvial fan gravel, some exposures of sand were present in February 2019 (fig. 16*A*), including within a small, low-relief alluvial channel in which cut banks indicated flowing water in the recent past (fig. 16*B*). Most of the landscape in polygon 5 consists of a gravelly lag deposit (including sample 5-S1; fig. 16*C*), although the sandy areas are composed of fine to medium sand (such as sample 5-S2). The polygon 5 landscape is sparsely vegetated by creosote, galleta grass, desert plantain, and nonnative *Schismus* sp. (Mediterranean grass). Low-relief, sandy coppice deposits are present around some of the creosote bushes.

Polygon 6 and Wiley Well wash lie west of the Mule Mountains (figs. 1, 17, 18) and represent a linked fluvial and aeolian sedimentary system. The elevation in the area in and around polygon 7 ranges from 162 m in the channel of Wiley Well wash to 320 m at the top of a large aeolian sand ramp on the western side of the Mule Mountains (fig. 1*C*). The dominant southeasterly wind direction and the relative positions of the wash channel and sand ramp imply that sediment forming the sand ramp is derived primarily from Wiley Well wash. Our characterization of this area included collecting sediment samples and geomorphic observations from several channels within Wiley Well wash, from polygon 6, and from the western end of the sand ramp. The wash channels contain particle sizes ranging from fine sand to cobbles, and the finer deposits contain sedimentary structures including subaqueous ripples and 20-cm-high subaqueous dunes (fig. 18). East of the wash, the terrain in polygon 6 comprises the distal part of an alluvial fan and overlying aeolian sand. Surface morphology showed characteristics of aeolian and alluvial-fan sediment transport (wind-rippled sand patches and shallow channels containing subaqueous ripples, respectively; fig. 17*A, B*) and included areas of well-sorted fine to medium aeolian sand (fig. 17*C*, samples 6-S4 and 6-S5). In addition to the sand ramp receiving windblown sediment from Wiley Well wash, it is likely that sediment recycling would occur there as some of the fine material that alluvial streamflow transports downslope (westward) would be moved back upslope (eastward) by wind—processes also documented in other drylands (for example, East and others, 2015). Occasional exposures of wind-rippled aeolian sand were present along with small sand shadows whose orientation indicated recent southeastward transport (toward 150–175 degrees, as of February 2019). Sand has accumulated as coppice dunes around some of the creosote and smaller shrubs. The fluvial

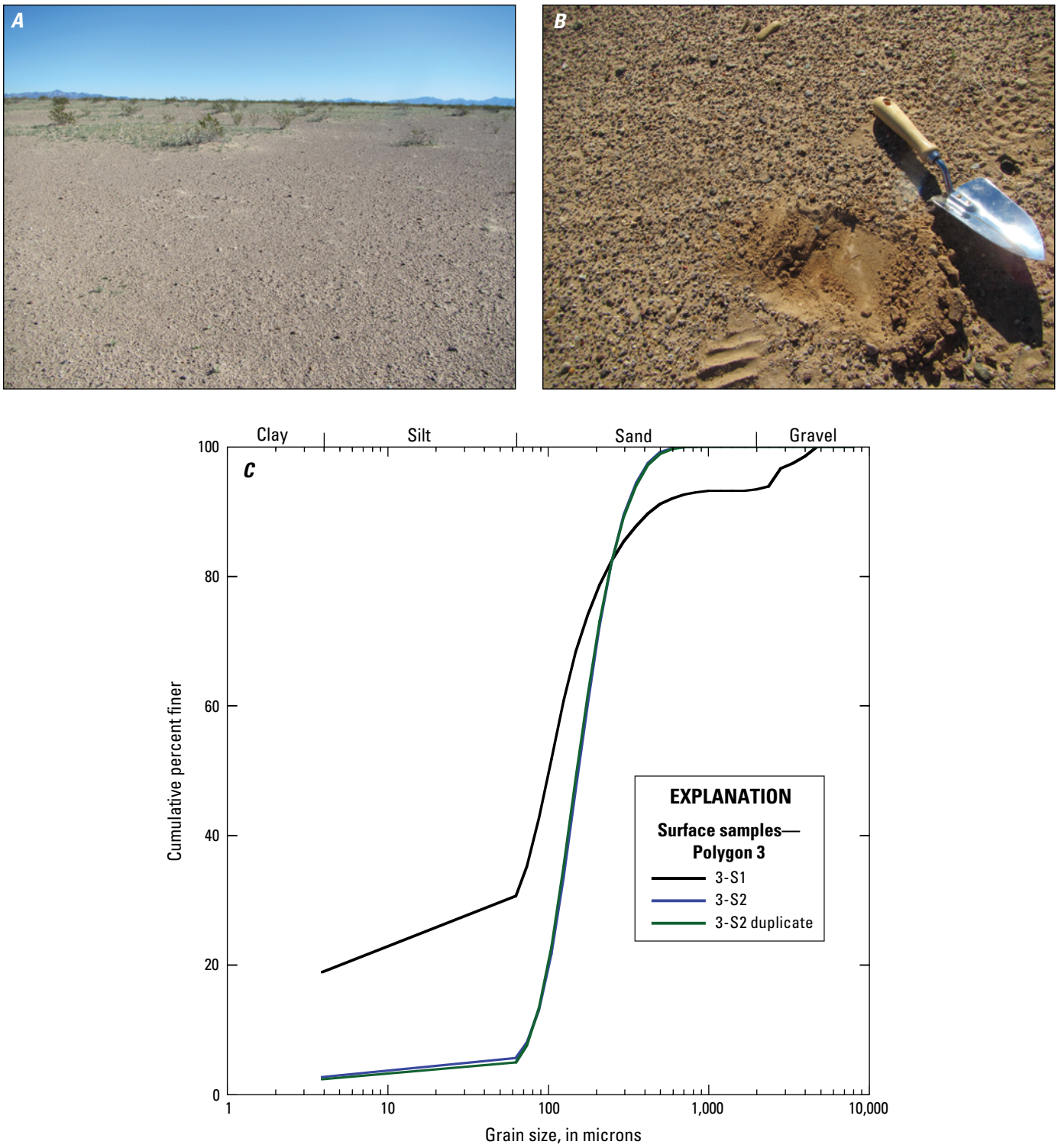

Figure 14. U.S. Geological Survey photographs of the land surface in polygon 3 (taken February 6, 2019) and grain-size graph of samples collected from polygon 3 in February 2019 (see fig.1*C* for location). *A*, Photograph showing the flat, sparsely vegetated land surface in polygon 3; the surface consists of a sand and gravel lag deposit. *B*, Photograph showing that sediment immediately below the surface (exposed by shallow excavation with the trowel shown) is finer-grained than the winnowed, gravelly lag deposit at the surface. *C*, Grain-size graph of samples 3-S1 and 3-S2. Sample 3-S1 was collected from an aeolian lag deposit. Finer sediment than that of Sample 3-S1 was observed below the land surface, as shown in *B*. Sample 3-S2 (analyzed twice in the laboratory as a duplicate for instrument quality control) was collected from a sandy, creosote-centered mound.

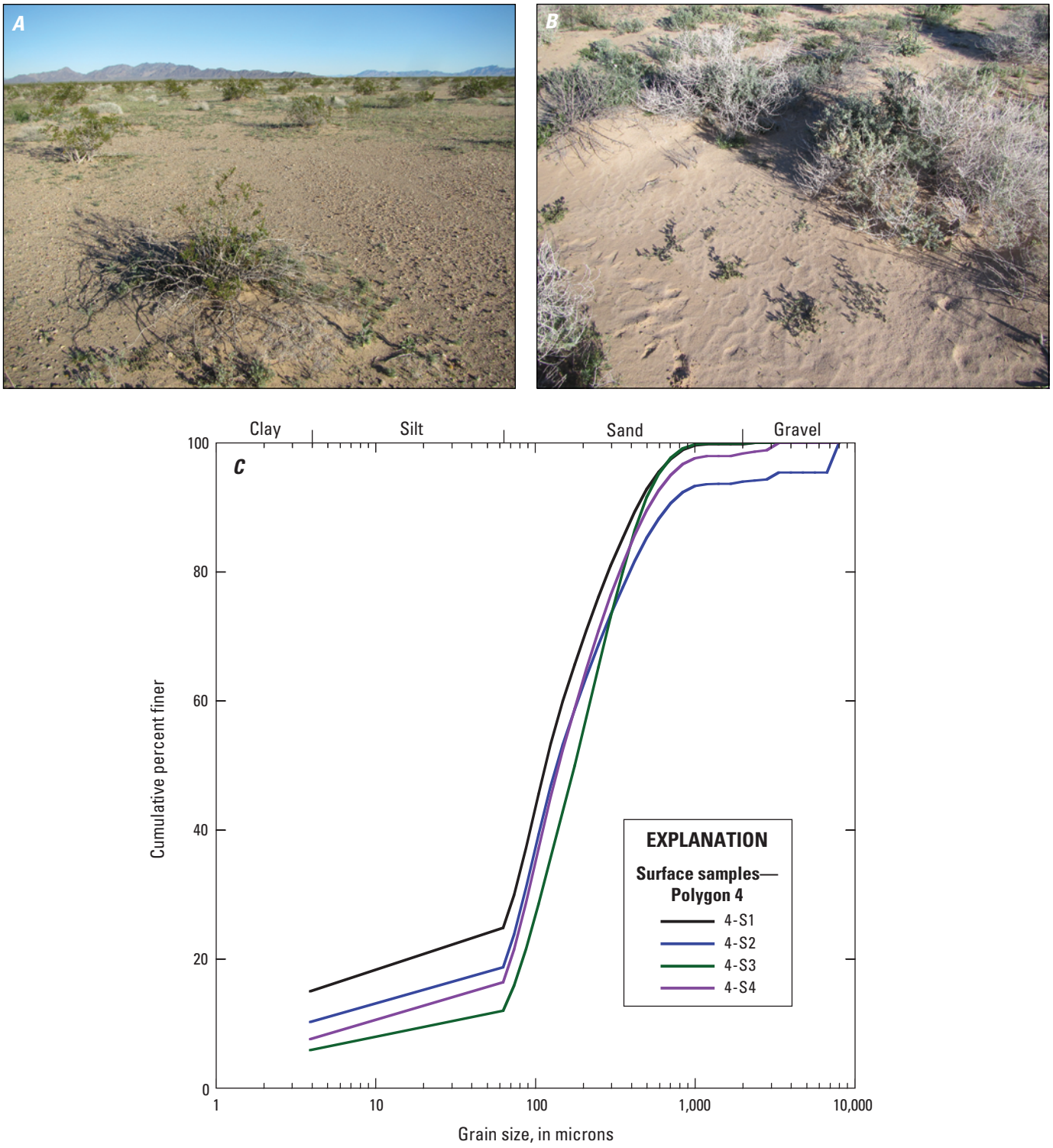

Figure 15. U.S. Geological survey photographs of the land surface in polygon 4 (taken February 6, 2019) and grain-size graph of samples collected from polygon 4 in February 2019 (see fig. 1*C* for location). *A*, Photograph showing creosote-centered coppice dunes surrounded by a gravelly lag deposit on the land surface in polygon 4. *B*, Photograph showing a patch of wind-rippled sand surrounded by vegetation. *C*, Grain-size graph of samples 4-S1 through 4-S4. Sample 4-S1 was collected from an aeolian lag deposit on the land surface. Sample 4-S2 was also from a lag deposit, which included some well-rounded chert pebbles. Sample 4-S3 was collected from a small, sandy, low-relief mound at the base of a dead creosote bush. Sample 4-S4 was collected from the surface lag deposit.

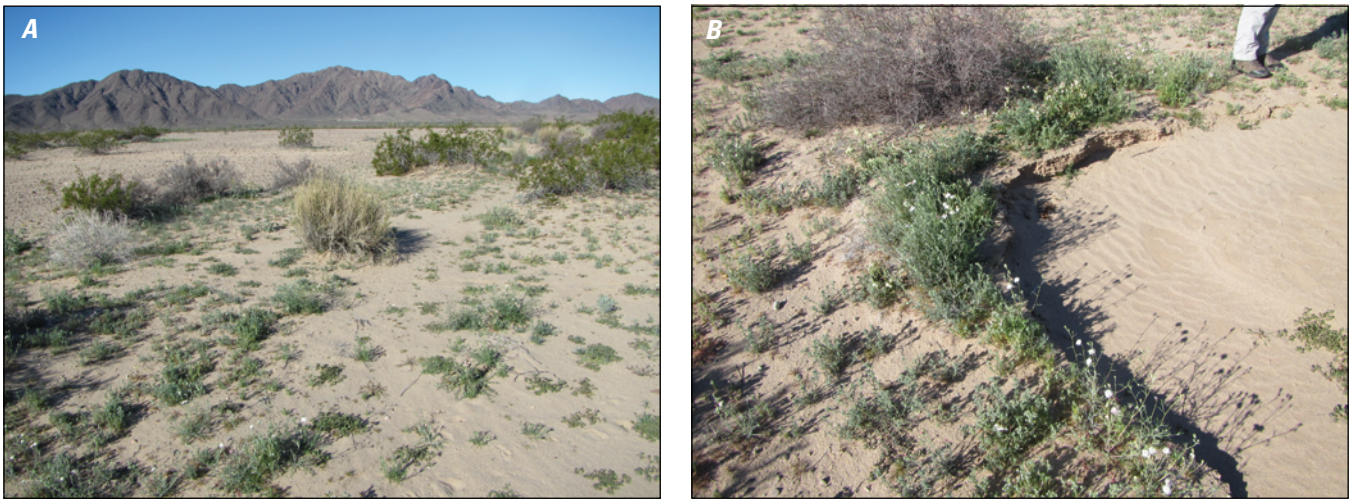

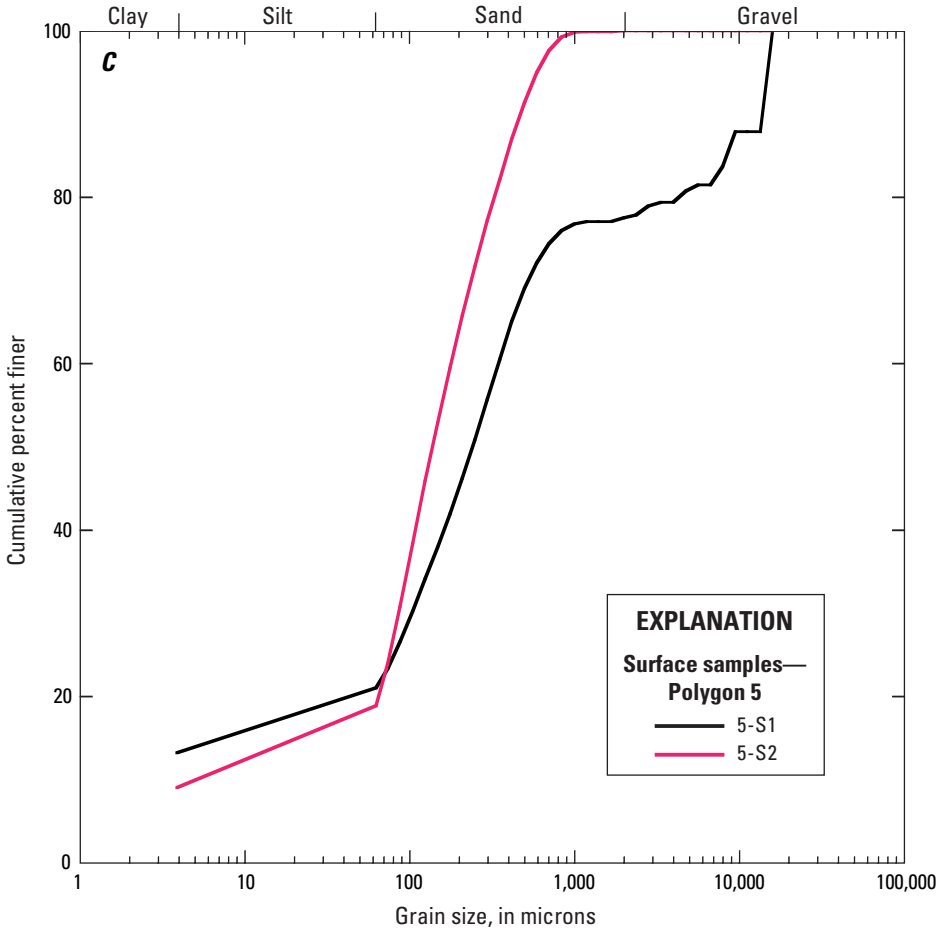

Figure 16. U.S. Geological Survey photographs of the land surface in polygon 5 (taken February 6, 2019) and grain-size graph of samples collected from polygon 5 in February 2019 (see fig. 1*C* for location). *A*, Photograph showing the sparsely vegetated alluvial fan surface, sloping up toward the Mule Mountains in this west-facing view. *B*, Photograph showing a low-relief cut bank at the edge of an alluvial channel indicates recent streamflow on the surface of the alluvial fan, although the sedimentary bedforms at the right of the image appear to have been formed by wind reworking the alluvial sand. *C*, Grain-size graph of samples 5-S1 and 5-S2. Sample 5-S1 was collected from a lag deposit on a distal alluvial-fan surface. Sample 5-S2 was collected from a low-relief, sandy mound on which galleta grass, creosote, and small forbs were growing.

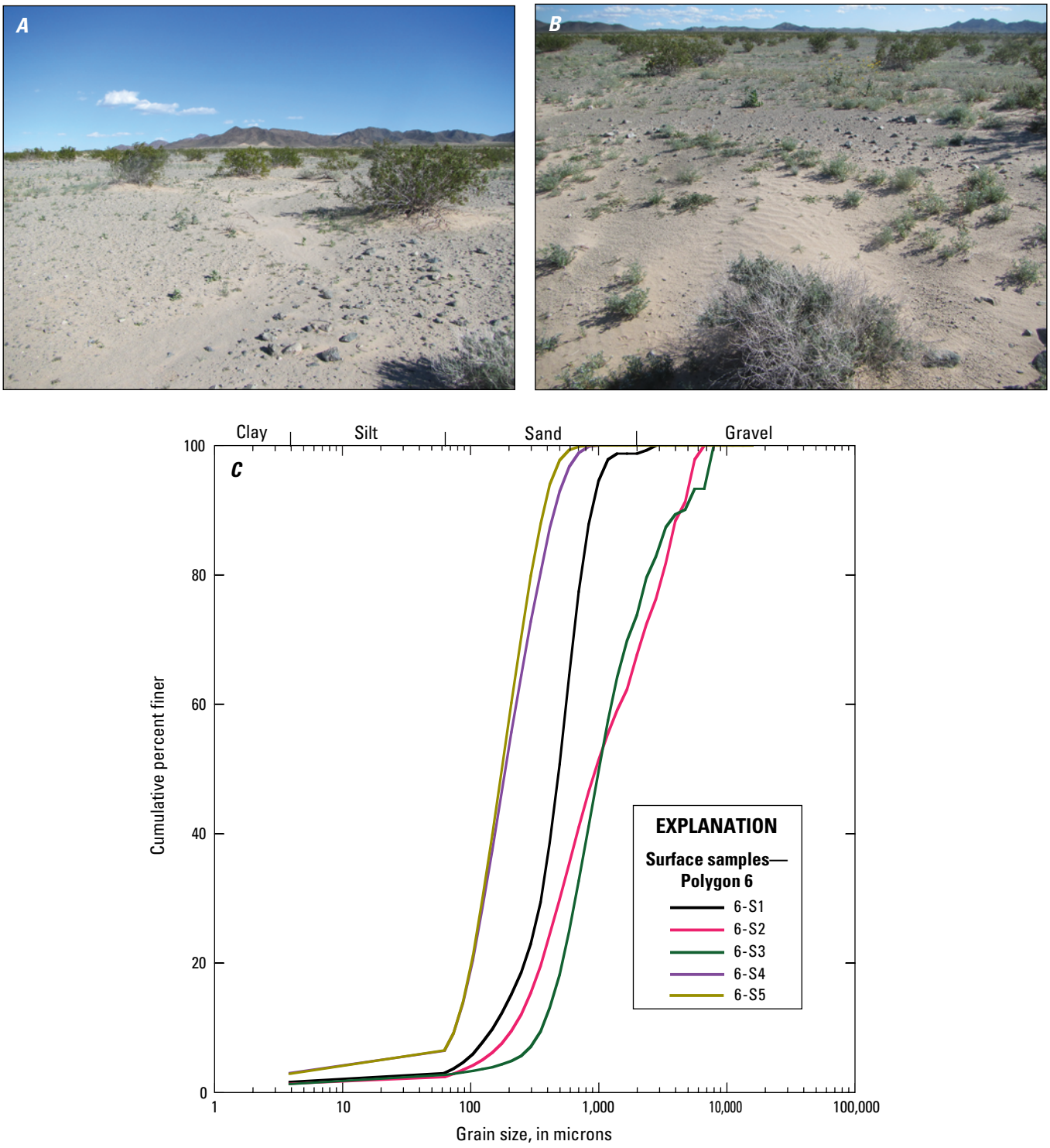

Figure 17. U.S. Geological Survey photographs of the land surface in polygon 6 (taken February 6, 2019) and grain-size graph of samples collected from polygon 6 in February 2019. *A*, Photograph showing the surface of the alluvial fan draining the western Mule Mountains (view facing east); a shallow (dry) alluvial channel is present in the center of the photograph, flowing toward the photographer. *B*, Photograph showing a patch of wind-rippled sand (light-colored sediment in the foreground and middle of the image) situated in the lee of a shrub atop the alluvial fan surface in polygon 6 (view facing southwest, aligned with the recent wind direction inferred from the wind-ripple orientations). Coarser-grained alluvial-fan sediment is visible in the background, behind the wind-rippled sand. *C*, Grain-size graph of samples 6-S1 through 6-S5. Samples 6-S1, 6-S2, and 6-S3 were collected within the dry, ephemeral stream channel of Wiley Well wash (see fig. 18 for photographs). Sample 6-S4 represents a wind-rippled sand deposit atop a distal alluvial-fan surface east of Wiley Well wash. Sample 6-S5 was collected within a sand shadow in the lee of vegetation shown in *B*; the sand shadow orientation indicated sand flux toward 163 degrees azimuth (toward south-southeast, indicating wind from the north-northwest).

Figure 18. U.S. Geological Survey photographs of the ephemeral stream channel Wiley Well wash, at the location immediately west of polygon 6, facing upstream (south), taken February 6, 2019. Both photographs show sand and gravel deposits in the ephemeral stream channel that have sedimentary structures (subaqueous ripples and dunes) characteristic of deposition by flowing water. Bed sediment consists of a range of grain sizes from sand to gravel. The recently active stream channel is approximately 20 m across at the location of *A* and 5 m across at the location of *B*.

material in the Wiley Well wash channels was coarse and poorly sorted (samples 6-S1, 6-S2, and 6-S3; fig. 17*C*). Vegetation in polygon 6 includes creosote, galleta, burrobush, occasional sand verbena, and an unidentified Asteraceae species. Animal burrows were observed in polygon 6, the largest being approximately 20 cm wide and 30 cm tall.

Polygon 7 features an active aeolian dune field that covers approximately 2 km^2 at elevation 134–139 m. The dunes apparently formed as a result of abundant aeolian sediment supply derived from the Wiley Well wash depocenter—the dune field is within the distal, northeastern part of this large depocenter (fig. 1*C*). Some sediment supply may also come from an unnamed, south-flowing ephemeral wash that drains the McCoy Mountains; the dune field occurs just north of where the north-flowing Wiley Well wash and the south-flowing ephemeral stream distributaries meet. The dune field includes dozens of dunes 1–3 m high, most with barchanoid morphology, that interact with very sparse vegetation (fig. 19). Some dunes display sinuous rather than barchanoid planform. Dune activity is evident from well-developed slip faces and sand shadows, and from dune slip faces partially burying living trees. The orientations of dune slip faces observed in February and November 2019 faced generally east, indicating eastward migration; slip-face orientations ranged from 59 to 128 degrees. Sand shadows observed in February 2019 indicated recent sand transport toward the east—sand shadows then were oriented toward 70–121 degrees. In November 2019, two weeks after the major northwesterly wind event of October 30–31, sand shadows in polygon 7 were oriented toward the south, although the much larger slip faces of dunes were still oriented eastward. The dunes commonly contained superimposed smaller bedforms on their stoss (upwind) surfaces. Interdune lag deposits contain metamorphic gravel clasts and, locally, mud-cracked fine sediment indicating the occasional presence of standing water. The east edge of the dune field is defined by the unnamed stream channel draining south from the McCoy Mountains. Dunes migrate eastward as far as the wash but not across it, which indicates that the dune sand is recycled into fluvial sediment when the wash flows. Episodic flow is expected to continue preventing the dunes from migrating across the wash entirely. The relative positions of washes and dunes in polygon 7 shows the interacting, cycling nature of aeolian and fluvial and (or) alluvial sediment transport in driving geomorphic evolution in this dryland setting. Grain-size analyses from the polygon 7 dune field show the dune sand (samples 7-S1 and 7-S3) to be mostly well-sorted medium sand, whereas interdune lag deposits (samples 7-S2 and 7-S4) are coarser and more poorly sorted, as is common for interdune deposits (fig. 19*C*). Animal burrows are present in the dune field, and some are as large as 10 cm across. Vegetation in polygon 7 consists of occasional creosote bushes, *Parkinsonia florida* (blue palo verde trees), sand verbena, Sahara mustard, and other small forbs and grasses.

Polygon 8 is located on the northwestern side of the Mule Mountains (fig. 1), at elevation 142–164 m, in an alluvial fan dissected by channel incision. The alluvial fan deposits in this region contain poorly sorted sediment (sand to cobble sized; fig. 20*A*). Alluvial fan material is overlain in many places by patches of well-sorted fine to medium sand (figs. 20*B*, *C*), some of which cover more than 100 square meters (m^2).

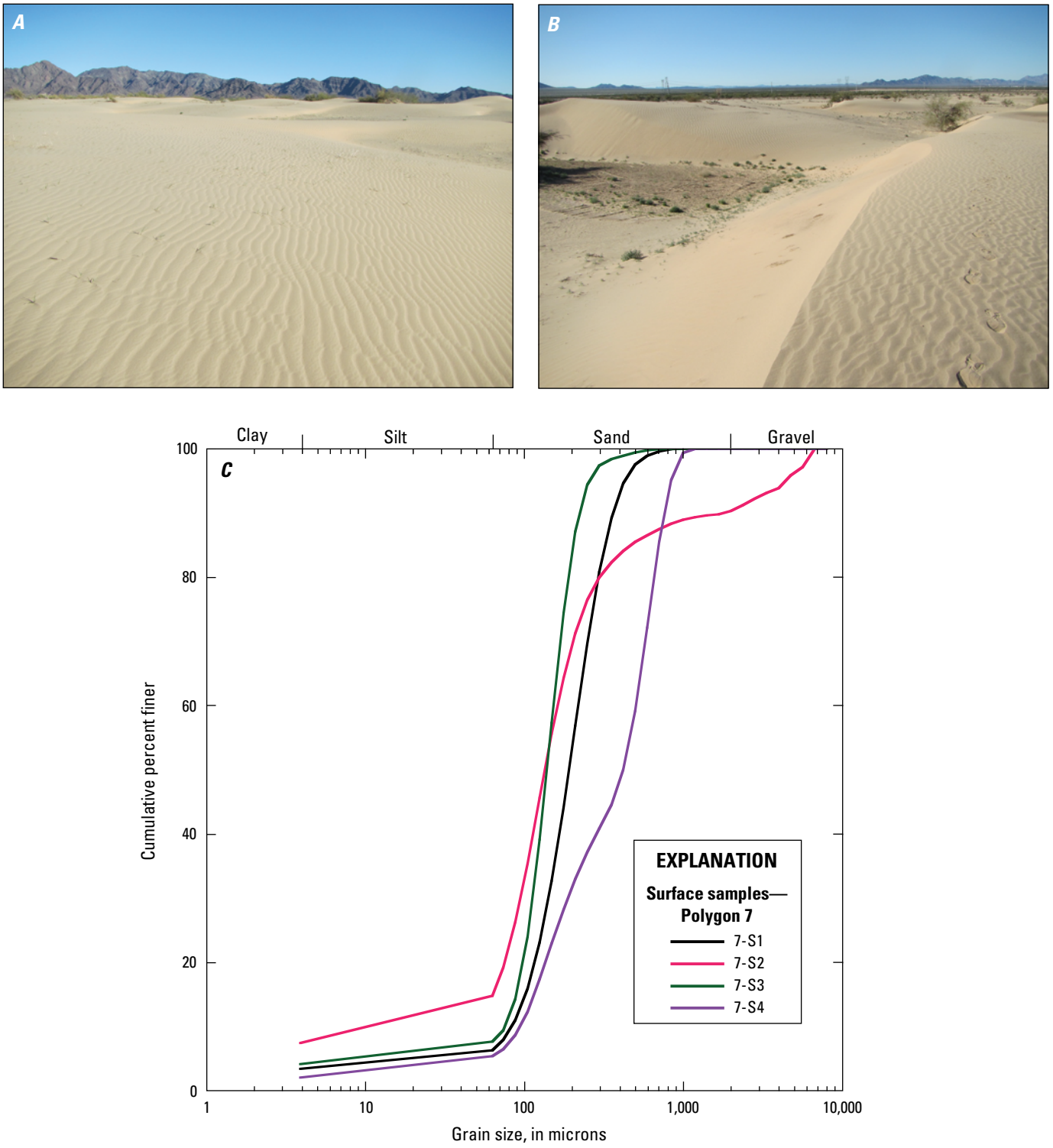

Figure 19. U.S. Geological Survey photographs of the land surface in polygon 7 (taken February 7, 2019) and grain-size graph of samples collected from polygon 7 in February 2019. *A* and *B*, Photographs show active aeolian dunes with wind-rippled surfaces; sparse vegetation is visible in the interdune area at the left side of *B*. *C*, Grain-size graph of samples 7-S1 through 7-S4. Sample 7-S1 was collected from an active dune surface consisting of mostly unvegetated dunes, commonly more than 2 meters high, with barchanoid morphology. Sample 7-S2 represents an interdune lag deposit. Sample 7-S3 was collected from an active dune surface within a large expanse of unvegetated sand. Sample 7-S4 was collected from an interdune deposit.

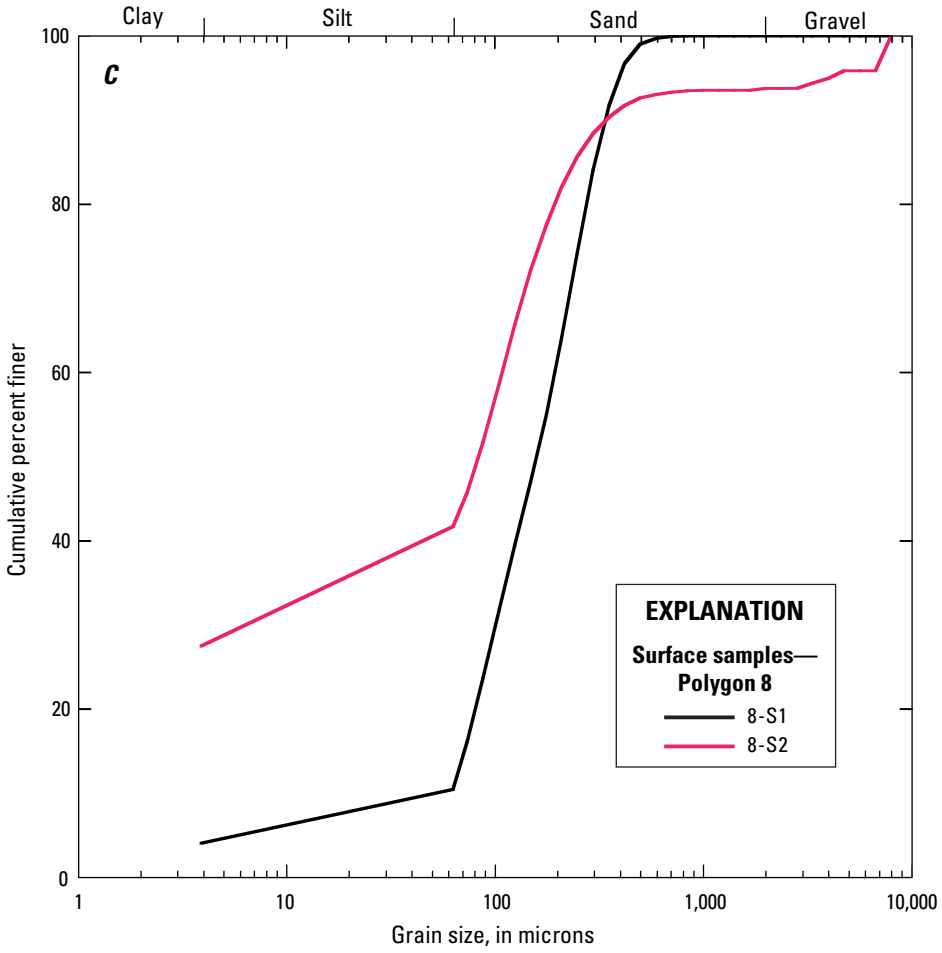

Figure 20. U.S. Geological Survey photographs of the land surface in polygon 8 (taken February 6, 2019) and grain-size graph of samples collected from polygon 8 in February 2019. *A* and *B*, Photographs show a distal alluvial fan surface dissected by channels; the Mule Mountains are visible farther south in the background. *B*, Photograph shows a ridge between wide alluvial channels features a veneer of aeolian sand. *C*, Grain-size graph of samples 8-S1 and 8-S2. Sample 8-S1 was collected from an aeolian sand deposit that formed a veneer on the downwind (generally eastern) side of ridges within a dissected alluvial fan. *C*, Sample 8-S2 was from a desert pavement surface on the distal portion of a dissected alluvial fan.

Wind ripples were noted on the sand patches. Digging 10 cm beneath the surface by hand exposed interbedded medium sand and coarser alluvial fan gravel, as well as some gypsum. In small, localized areas, we observed mud cracks that indicated the former presence of standing water and its subsequent evaporation, which is consistent with the formation of gypsum deposits—commonly an evaporite mineral. Locally, aeolian sand is thick enough to form small, low-relief dunes, but the dominant, landscape-forming process at polygon 8 and its surrounding area is alluvial fan activity. Some desert pavement development is apparent on the higher-elevation portions of the distal alluvial fan. Vegetation in polygon 8 includes sand verbena growing on the aeolian sand deposits, creosote, Sahara mustard, desert plantain, an unidentified aster, and other small forbs and shrubs. We also observed animal burrows as large as 10–15 cm in diameter.

In addition to the eight polygons described above, the southeastern part of the Palen dune field (fig. 1) was visited in February 2019. This large dune field (more than 35 km^2) contains many barchanoid dunes, sourced by sediment from the ephemeral Palen Lake (fig. 1*A*). A recent remote-sensing analysis determined that the dunes have been migrating southeast at rates of 50 m/yr (Potter and Weigand, 2016). Between 1984 and 2011, the areal extent of active dunes in the Palen dune field increased by 60 percent, and vegetation cover decreased by approximately 30 percent (Potter and Weigand, 2016). The active dunes that we observed in February 2019, just southwest of the Palen Mountains at elevation 127 m, had slip faces indicating southeastward migration (slip faces were oriented toward 97–156 degrees). Sand shadows were also oriented toward the southeast. Active, rapid dune migration was evident on the ground as dunes could be seen burying living trees to depths of a meter or more. Grain size on the three dune samples we collected was dominantly fine to medium sand, and a fourth sample, from an interdune deposit, consisted mostly of very fine sand (fig. 21*C*). Sparse vegetation in the southeastern portion of the Palen dune field includes Sahara mustard, Russian thistle, creosote and blue palo verde trees.

Stratigraphy and Luminescence Dating

Findings from subsurface excavations in March 2020 are described in this subsection; the results from pits 1, 2, 3, 202, and 4 (locations on fig. 1*C*) are presented in order from northwest to southeast. Five stratigraphic columns are compiled in fig. 22, and details are shown for individual pits in figures 23–27. Ages determined by luminescence dating are summarized in table 3.

Pit 1 was excavated by backhoe into an already exposed cutbank in a dry wash north of Interstate 10 (elevation 132 m). The alluvial cutbank was 135 cm high and the pit was dug to 120 cm below the stream bed, for a total exposed sediment depth of 255 cm. The land surface around the alluvial channel consisted of distal alluvial fan deposits (sand and gravel), was sparsely vegetated with creosote, and appeared to have incipient desert-pavement development. The fan surface included multiple entrenched alluvial channels that had some channel braiding within washes and visible subaqueous sedimentary structures, such as ripples, indicating recent surface-water flow. Most of the alluvial sediment in the wash was finer than 32 mm, as measured with a gravelometer. The wash in which pit 1 was excavated trends northeast to southwest at 30 degrees.

The upper 55 cm of pit 1 strata consisted of siliciclastic sand and gravel that constitute three units. The uppermost unit was unconsolidated sand, was 10YR 6/4 on the Munsell soil color chart, and extended from the surface to 29 cm depth. Within this unit, a pedogenic A horizon was defined between 0 and 20 cm. Below the A horizon, the remainder of the section was classified as a Btk horizon on the basis of clay and carbonate content, with color 7.5YR 5/4 to 5YR 4/4. Within the uppermost unit, sample IRSL-1 (collected at a depth of 20 cm) yielded a date best estimated at 1.82 ± 0.13 ka. This sample was located high enough in the section that sediment could be affected by soil-forming and mixing processes. The migration of sand particles from the surface by illuviation or bioturbation could bring particles more recently exposed to sunlight to lower depths, lowering the average luminescence age of individual sand grains at depth. The net effect on our multigrain luminescence dating method would be to lower the apparent depositional age of a given sample. To minimize these possible effects for IRSL-1, we used a coarse grain size (180–250 μm sand grains) assuming these would be less mobile than finer grains. We also used very small aliquots (about 10–20 grains per disc) to minimize the averaging effect of infiltrated grains on multigrain measurements. Finally, we applied the maximum age model of Galbraith and Roberts (2012), a statistical method that biases the age calculation toward grains with a greater luminescence and thus higher age. This model is often used in this context of mixed materials to avoid infiltrated grains (Galbraith and Roberts, 2012). Application of the maximum age model is justified by the proximity of IRSL-1 to the surface, the presence of sparse roots, and the lack of clear sedimentary structures in the unit, which were interpreted to indicate some mixing in the upper layer. The use of these methods should minimize any effect of mixing or infiltration. Application of the maximum age model, as opposed to the CAM used for the rest of the samples, results in an age of 1.82 ± 0.13 ka for sample IRSL-1. This value is just outside of the uncertainty from the CAM age of 1.56 ± 0.10 ka. The similarity in ages suggests that any mixing effect may not be large compared to the true depositional age. Although we interpret the maximum age model age as a fairly good approximation of the true depositional age, we cannot discount that the entire deposit may have been mixed, such that all the grains have a young age compared to the age from primary deposition. In such a scenario, it is debatable if such intense mixing may be considered a post-depositional process instead of a primary depositional one. However, the arid climate and sparse vegetation of pit 1 may make such intense mixing unlikely.

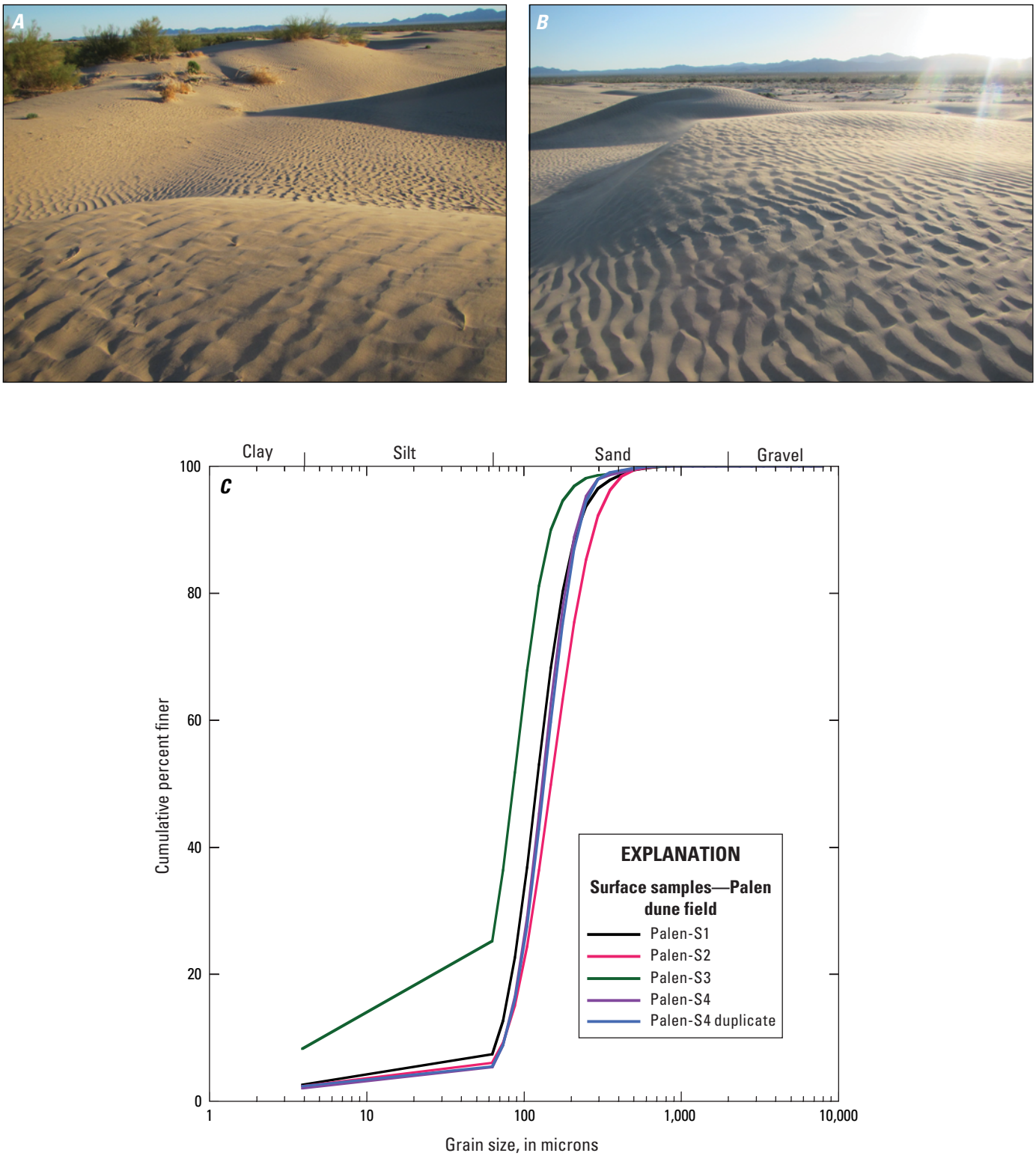

Figure 21. U.S. Geological Survey photographs of the land surface in the southeast side of the Palen dune field (see fig. 1*B* for location), and grain-size graph of samples collected from the southeastern part of the Palen dune field in February 2019. *A* and *B*, Photographs were taken on February 6, 2019, and show active aeolian dunes with wind-rippled surfaces, and sparse vegetation in the background of each image. In the background of *A*, dunes can be seen burying living trees (view is facing southwest in *A*, west in *B*). *C*, Grain-size graph of samples Palen-S1 through Palen-S4.Samples Palen-S1, Palen-S2, and Palen-S4 (also run as a laboratory duplicate, for quality control) were taken from the surface of active, mostly unvegetated aeolian dunes with barchanoid morphology. Sample Palen-S3 was collected from an interdune lag deposit.

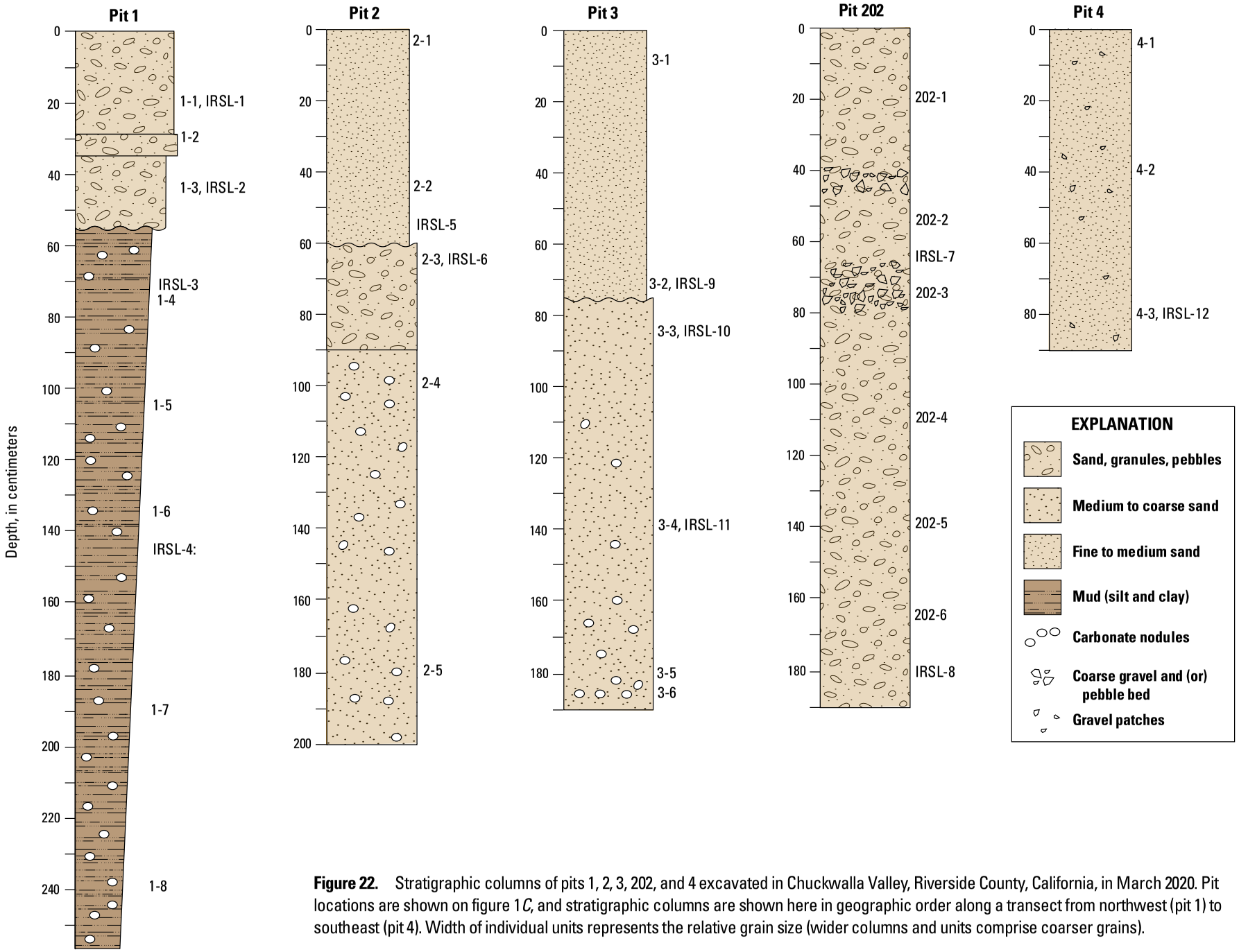

Figure 22. Stratigraphic columns of pits 1, 2, 3, 202, and 4 excavated in Chuckwalla Valley, Riverside County, California, in March 2020. Pit locations are shown on figure 1*C*, and stratigraphic columns are shown here in geographic order along a transect from northwest (pit 1) to southeast (pit 4). Width of individual units represents the relative grain size (wider columns and units comprise coarser grains).

Table 3. Sediment-sample ages determined by infrared-stimulated luminescence (IRSL) dating.

[Pits are listed in order from northwest to southeast. Abbreviations: cm, centimeter; ka, thousand years ago]

Sample name	Pit number	Latitude	Longitude	Depth below surface (cm)	Age (ka)
IRSL-1	1	33.612	−114.898	20	1.82 ± 0.13
IRSL-2	1	33.612	−114.898	45	15.2 ± 1.1
IRSL-3	1	33.612	−114.898	70	226 ± 11.4
IRSL-4	1	33.612	−114.898	145	266 ± 15.4
IRSL-5	2	33.587	−114.834	55	0.31 ± 0.0
IRSL-6	2	33.587	−114.834	65	2.20 ± 0.2
IRSL-7	202	33.557	−114.778	70	11.2 ± 0.9
IRSL-8	202	33.557	−114.778	180	22.2 ± 0.9
IRSL-9	3	33.586	−114.823	72	4.35 ± 0.4
IRSL-10	3	33.586	−114.823	85	20.1 ± 2.7
IRSL-11	3	33.586	−114.823	140	21.2 ± 1.6
IRSL-12	4	33.546	−114.752	80	24.4 ± 1.4

A coarse, gravel-dominated unit extended below a diffuse contact at 29 cm to a depth of 35 cm, and farther below, a unit of gravelly sand extended 35–55 cm depth, from which sample IRSL-2 (at 45 cm) provided an age of 15.2 ± 1.1 ka (late Pleistocene). Weak stratification was apparent within the three uppermost units, consisting of faint crossbedding and gravel lenses. On the basis of these features, we inferred repeated deposition of sand and gravel, which is consistent with an alluvial setting. At 55 cm depth a prominent, sharp unconformity was apparent (fig. 23). Below the unconformity, the remainder of the sediment (down to the base at 255 cm depth) was substantially finer than the overlying units and showed slight upward coarsening, but generally was massive with little or no distinct bedding. Particularly below 110 cm, the massive lower unit was observed to be very dense and dominated by clay and silt. Near the base, sample 1-8 (from 240 cm depth) contained 25 percent silt and clay (fig. 23*D*). Nested gypsum crystals and soft carbonate masses (both occurring commonly larger than 1 cm across) were present throughout the deposit below the unconformity (fig. 23*C*). Streaks of gypsum and carbonate became more abundant deeper in this massive, fine-grained unit. Two Pleistocene IRSL ages indicated that the massive, fine unit contained much older material than above the unconformity. Sample IRSL-3 (70 cm depth) was dated to 226 ± 11.4 ka, and sample IRSL-4 (145 cm depth) was dated to 266 ± 15.4 ka. Sediment below 145 cm was considered too fine-grained for IRSL dating to be feasible. We note that the pIRIRSL protocol that we developed in this study was neither designed nor tested for samples as old as these. Therefore, it is possible that these represent minimum ages, depending on how the feldspar pIRIRSL technique behaves using the higher doses associated with these ages. However, exploring the effectiveness of this protocol is beyond the scope of the present study.

The lower material in pit 1 (below the unconformity at 55 cm depth) was interpreted to represent a Pleistocene lake bed that formed a playa deposit, judging from the fine grain sizes and evaporite mineralization, or perhaps part of a Pleistocene floodplain deposit of the Colorado River. The local sediment accumulation rate in that playa environment is estimated to have been 0.002 cm/yr, based on the 75-cm vertical distance between samples IRSL-3 and IRSL-4, and with no hiatus evident within the playa deposition. If that deposition rate were maintained through the rest of the playa sediment accumulation (from 70 cm depth up to the unconformity at 55 cm), then the uppermost lacustrine and (or) playa sediment presumably would represent an age of around 218 ka. Therefore, the unconformity at 55 cm possibly spans almost 100 thousand years (k.y.) of missing time, before the sedimentary record at this location resumed with sand and gravel accumulation in late Pleistocene time. Sediment above 55 cm depth is interpreted as distal alluvial fan deposits, possibly accompanied by minor accumulation of aeolian sediment. The accumulation of the uppermost 55 cm presumably occurred episodically; minor hiatuses formed from fan channels that scoured and deposited material and avulsed and abandoned drainage paths. We calculate an accumulation rate of 0.013 cm/yr for the uppermost (alluvial) sediment in pit 1 (that is, 20 cm accumulating above the depth of sample IRSL-1 in the last 1,560 years), apparently an order of magnitude faster than during the Pleistocene lacustrine phase.

Pit 2 was excavated with a backhoe into the sparsely vegetated sand sheet in the northwestern part of polygon 2 at elevation 135 m (figs. 1*B*, 24). The surface material at that site primarily consists of loose sand, which was commonly wind-rippled and formed occasional dunes 10–40 cm high. Small coppice dunes were also observed around shrubs. Patchy exposures of sand and gravel 1 to 3 m^2 were present near the excavation site and were inferred to be aeolian lag deposits. Gravel clasts in those surface lag exposures included well-rounded siliciclastic pebbles of sandstone, quartzite, chert, and possibly other lithologies. We did not observe any surface exposures indicating recent water-borne sediment transport near pit 2.

The excavation of pit 2 reached a depth of 200 cm. The uppermost unit (fig. 24*D*), a C horizon with color classified as 10YR 6/4, consisted of well-sorted fine to medium sand (samples 2-1 and 2-2; fig. 24*E*) that formed faint laminations dipping toward the east. Laminations had the appearance and

Figure 23. Stratigraphic column, U.S. Geological Survey photographs (taken March 16, 2020), and grain-size graph showing data collected from pit 1, excavated in March 2020. *A*, Stratigraphic column showing relative grain size (width of column) of sediment observed and depths of sediment samples 1-1 through 1-8, and for four post infrared infrared-stimulated luminescence (pIRIRSL) samples. Ages are indicated to the right of pIRIRSL sample labels and shown in table 3. *B*, Photograph showing the upper 1.5 m of pit 1. The measuring tape reel at right is resting on a distal alluvial fan surface incised by a dry stream channel whose cutbank was used as part of the pit 1 stratigraphic column. *C*, Photograph showing a representative example of the carbonate- and gypsum-bearing, mud-rich deposit about 2 meters deep in pit 1. *D*, Graph of grain-size distribution for samples from pit 1. Samples 1-1, 1-2, and 1-3 contain sand and gravel from the upper half-meter of the deposit. Samples 1-4 through 1-8 were collected from finer-grained Pleistocene material below an unconformity at 55 cm, interpreted as likely lake-bed (playa) deposits.

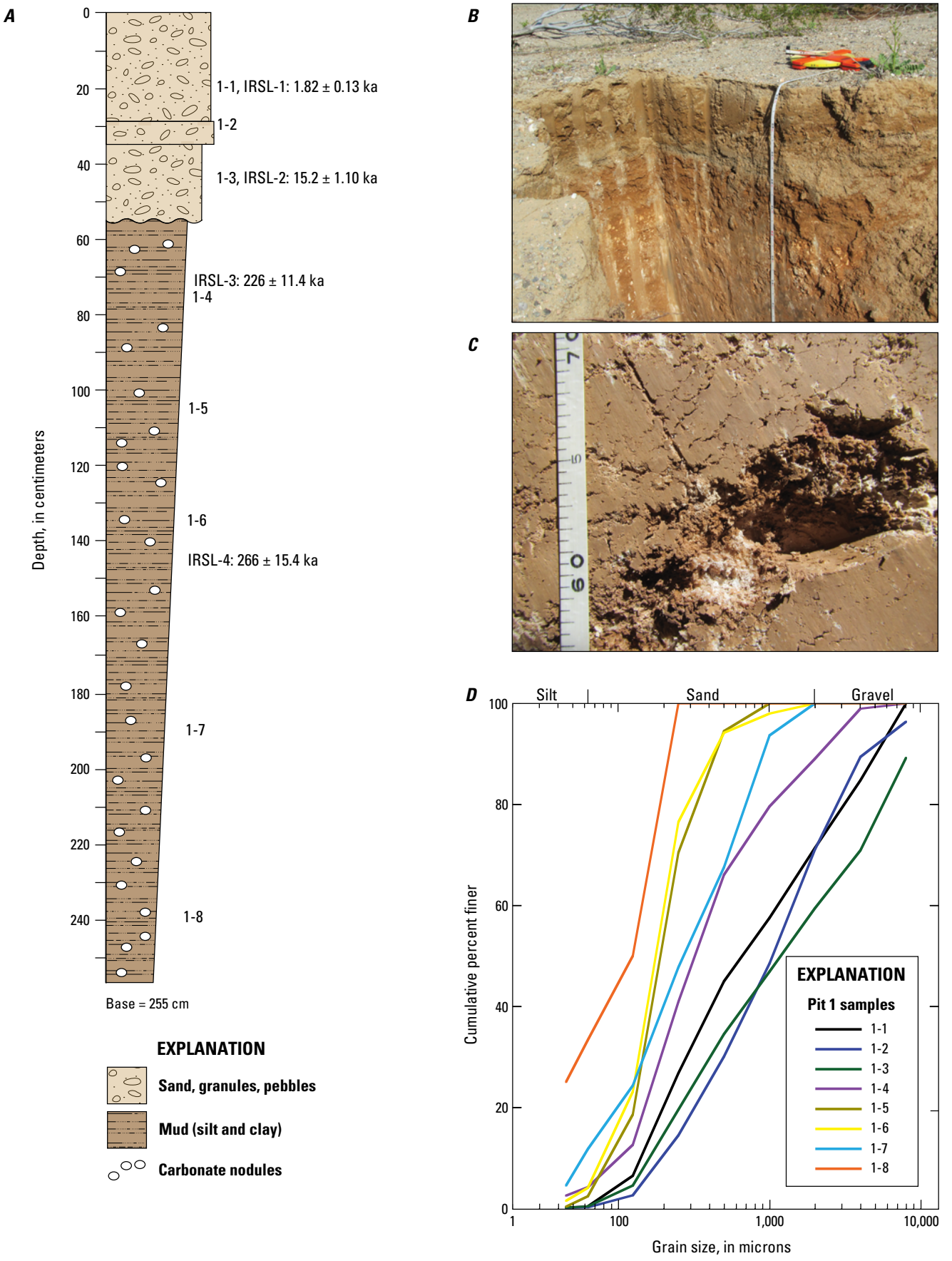
A
Depth, in centimeters
0
20
40
60
80
100
120
140
160
180
200
220
240
1-1, IRSL-1: 1.82 ± 0.13 ka
1-2
1-3, IRSL-2: 15.2 ± 1.10 ka
IRSL-3: 226 ± 11.4 ka
1-4
1-5
1-6
IRSL-4: 266 ± 15.4 ka
1-7
1-8
Base = 255 cm
EXPLANATION
Sand, granules, pebbles
Mud (silt and clay)
Carbonate nodules
B
C
D
Silt
Sand
Gravel
Cumulative percent finer
Grain size, in microns
1
100
1,000
10,000
EXPLANATION
Pit 1 samples
1-1
1-2
1-3
1-4
1-5
1-6
1-7
1-8

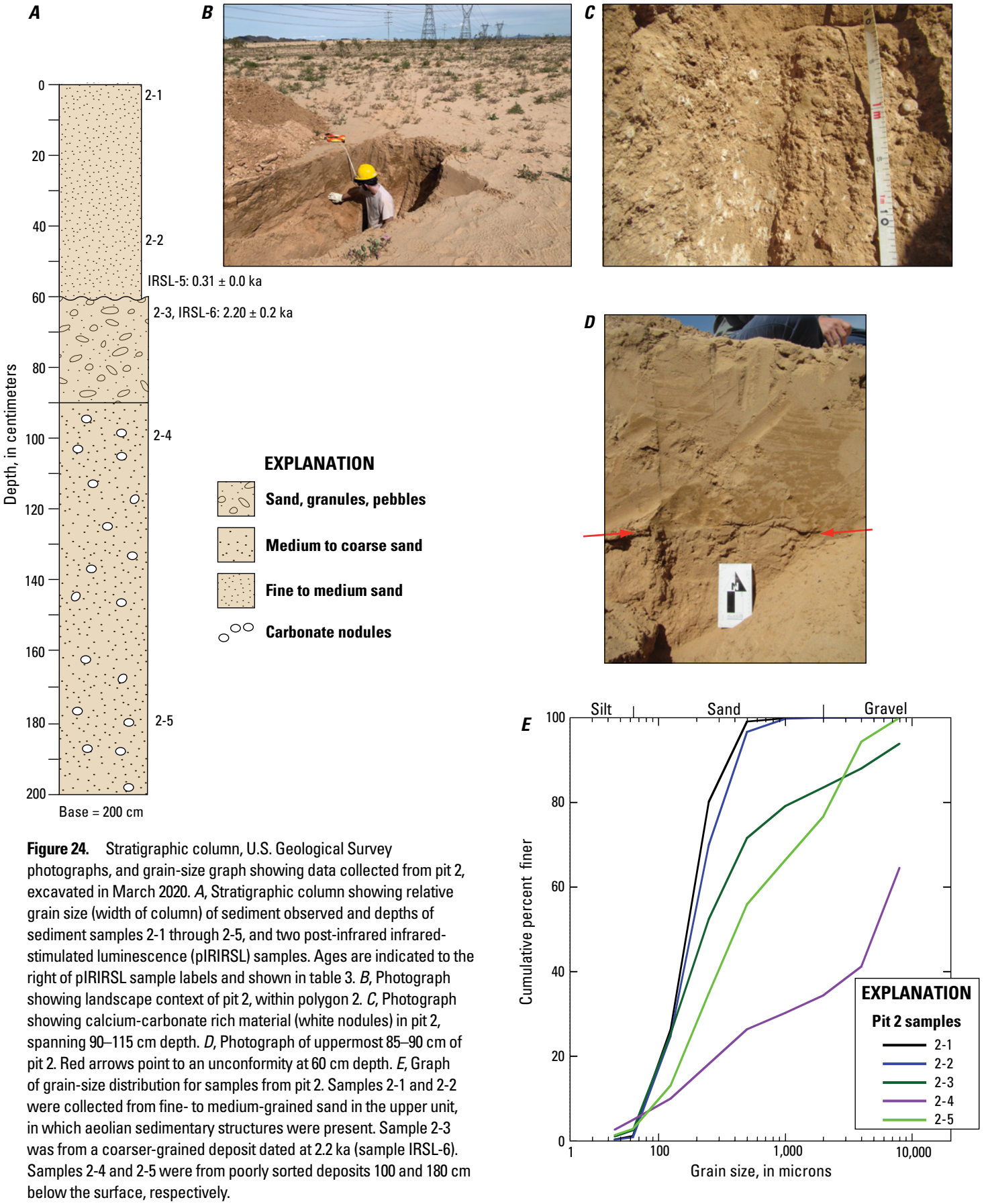

Figure 24. Stratigraphic column, U.S. Geological Survey photographs, and grain-size graph showing data collected from pit 2, excavated in March 2020. *A*, Stratigraphic column showing relative grain size (width of column) of sediment observed and depths of sediment samples 2-1 through 2-5, and two post-infrared infrared-stimulated luminescence (pIRIRSL) samples. Ages are indicated to the right of pIRIRSL sample labels and shown in table 3. *B*, Photograph showing landscape context of pit 2, within polygon 2. *C*, Photograph showing calcium-carbonate rich material (white nodules) in pit 2, spanning 90–115 cm depth. *D*, Photograph of uppermost 85–90 cm of pit 2. Red arrows point to an unconformity at 60 cm depth. *E*, Graph of grain-size distribution for samples from pit 2. Samples 2-1 and 2-2 were collected from fine- to medium-grained sand in the upper unit, in which aeolian sedimentary structures were present. Sample 2-3 was from a coarser-grained deposit dated at 2.2 ka (sample IRSL-6). Samples 2-4 and 2-5 were from poorly sorted deposits 100 and 180 cm below the surface, respectively.

scale of aeolian sedimentary structures, and so this uppermost unit was interpreted as a dune foreset deposit (see, for example, Rubin and Hunter, 1982; Rubin and Hunter, 1987). The lower contact of this unit also dipped slightly toward the east, such that its depth ranged from 50 to 70 cm within the pit (contact shown at 60 cm in fig. 24*A*). Sample IRSL-5, collected at 55 cm depth in the uppermost sand deposit, yielded an age of 0.31 ± 0.0 ka. Below the inferred aeolian dune foreset sand, a massive, slightly coarser, but still sand-dominated unit extended from about 60 to 90 cm depth. This layer, a 10YR 6/4 Bk horizon, was slightly indurated, poorly sorted, and contained siliciclastic gravel in addition to sand. Many of the gravel particles had carbonate precipitate adhering to their downward-facing surfaces (field tested with weak acid). Sample IRSL-6, at a depth of 65 cm in this sand-dominated unit, returned an age of 2.20 ± 0.2 ka. Therefore, the contact between the uppermost aeolian dune sand and the underlying, more indurated sand and gravel (marked with red arrows in fig. 24*D*) evidently is an unconformity spanning approximately 2,000 years.

The upper contact (about 90 cm depth) of the lowermost unit in pit 2 was poorly defined. The material below this contact (to 200 cm depth) was composed of massive, well-indurated, poorly sorted sand and gravel; this interval was defined as a Bk horizon consisting of pervasive, well-cemented carbonate development (fig. 24*C*). Carbonate distribution resembled that of a stage I or II carbonate soil, consistent with the abundant carbonate mineralization observed by Everett and others (2013) in the lower units of their borehole in eastern Chuckwalla Valley near the location of pit 2. No pIRIRSL date was obtained from this lowermost unit at pit 2 because the degree of induration precluded driving the steel collection tube into the wall of the pit. Furthermore, the presence of abundant pedogenic carbonate in the lower part of pit 2 suggested that dose-rate changes over time could preclude accurate luminescence dating. Siliciclastic particles in the lowermost unit consisted of several lithologies, including quartzite, and some clasts seemed to have desert varnish on their surfaces. Sizes of clasts at different depths in pit 2 were as large as 32 mm, measured with a gravelometer in the field (samples collected for later sieving included only material 8 mm and finer; fig. 24*E*). Well-rounded siliciclastic pebbles of similar lithologies to those in the pit are present in nearby surface lag deposits. These resemble clasts in the ancestral Colorado River deposits of Palo Verde Mesa (which we visited in outcrops both north and south of Interstate 10) or those reported to be exposed in the river gravels of unit QTmm on the northwestern side of the Mule Mountains (Stone, 2006).

We interpret the lower part of the depositional sequence at pit 2 to represent an older phase of alluvial deposition (of undetermined age) that probably interacted with aeolian sediment accumulation. These modes of sediment transport and deposition may have combined to produce the material below 60 cm depth in this location, although interbedding of fluvial and aeolian deposits is not clearly apparent; it is possible that original sedimentary structures characteristic of aeolian or fluvial deposition (for example, Draut and others, 2008) have been obscured by pedogenic carbonate precipitation. The alluvial activity is evidenced by the common occurrence of well-rounded gravel below 60 cm depth at this site. This material may have been deposited directly by a former channel or floodplain of the Colorado River or, alternatively, by alluvial fan activity originating on the northern flanks of the Mule Mountains that reworked older Colorado River (unit QTmm of Stone, 2006) gravels. Both means of delivering alluvial sand and gravel to the pit 2 location seem plausible, and distinguishing between them is difficult because Colorado River paleocourses have not been dated geochronometrically in this immediate field area.

Local sediment accumulation at the pit 2 site appears to have been entirely aeolian after approximately 2 ka. Aeolian dune foreset bedding advanced over this area, likely migrating eastward given the eastward dip of laminations and of the unconformity bracketed by samples IRSL-5 and IRSL-6 (fig. 24). The most recent deposit, from 60 cm depth to the modern surface, occurred fairly rapidly at an average rate of 0.18 cm/yr (55 cm of sand accumulating in 0.31 k.y.). Instead of accumulating continuously at this rate, the entire upper unit (60 cm) probably accumulated much more rapidly, perhaps in one or two years as a dune migrated through this location, and thereafter the site experienced nondeposition or deposition that was removed later by deflation.

Pit 3 was excavated with a backhoe to a depth of 190 cm at a site 1.1 km east-southeast of pit 2, at elevation 134 m (fig. 25; location shown in fig. 1*B*). The surface morphology near pit 3 is similar to that around pit 2 and consists of loose sand that is commonly wind-rippled and constitutes small aeolian coppice dunes 10–50 cm high (dune morphology was not well developed there as of March 2020). Patches of coarse sand and gravel, inferred to be aeolian lag deposits, are present near pit 3 (fig. 25*B*)—that is, a winnowed lag deposit formed by wind deflation of a mixed alluvial and aeolian deposit. Some of the clasts in those surface lag exposures are well-rounded siliciclastic pebbles, including some that are chert. The advanced state of rounding indicates that these gravel clasts had been transported long distances by water. Other clasts at the surface are subangular to subrounded.

Sediment exposed in pit 3 consisted mostly of well-sorted medium sand and minor amounts of coarse sand, very coarse sand, and occasional gravel (fig. 25). The upper unit of pit 3 extends to about 75 cm depth and was a C horizon composed of 10YR7/4 unconsolidated, laminated, well-sorted, fine to medium sand interpreted as an aeolian deposit. Near the base of this unit, at 72 cm depth, sample IRSL-9 yielded an age of 4.35 ± 0.4 ka. A gently westward-dipping contact occurred about 75 cm depth. Below that contact, pedogenic carbonate indicated a CBk to Bk horizon (color 10YR 6/4) throughout the lower part of the section (from 75 to 190 cm depth). No other contacts were observed below 75 cm depth. The weakly indurated lower unit was massive, showed no apparent bedding or sedimentary structures, and was composed mostly of sand but contained sparse lithic fine gravel (one clast was 16 mm and the rest were finer). No sorting was apparent in the lower unit. Pedogenic carbonate was commonly observed within the lower unit as nodules that could be disaggregated by hand; and linear, subhorizontal carbonate

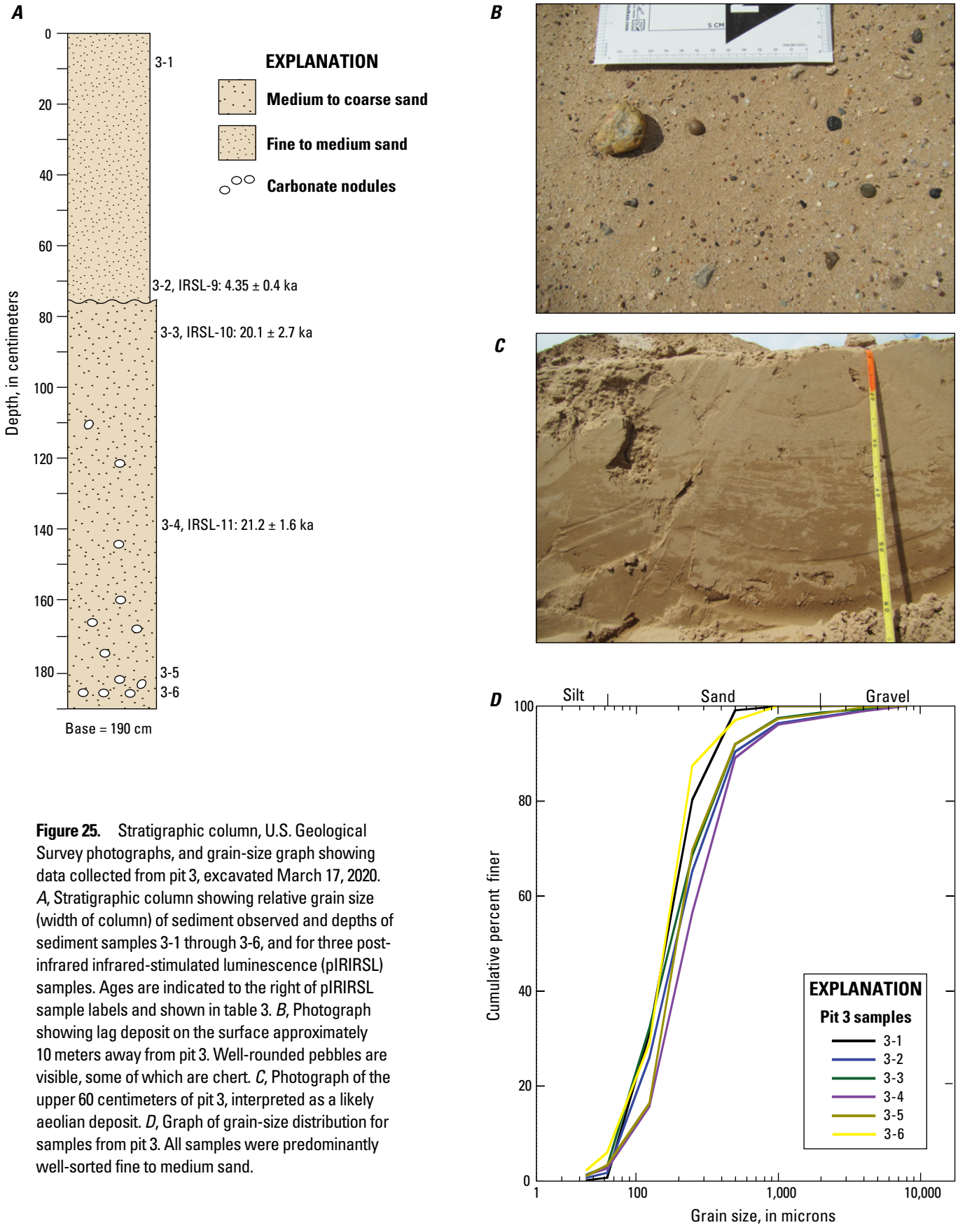

Figure 25. Stratigraphic column, U.S. Geological Survey photographs, and grain-size graph showing data collected from pit 3, excavated March 17, 2020. *A*, Stratigraphic column showing relative grain size (width of column) of sediment observed and depths of sediment samples 3-1 through 3-6, and for three post-infrared infrared-stimulated luminescence (pIRIRSL) samples. Ages are indicated to the right of pIRIRSL sample labels and shown in table 3. *B*, Photograph showing lag deposit on the surface approximately 10 meters away from pit 3. Well-rounded pebbles are visible, some of which are chert. *C*, Photograph of the upper 60 centimeters of pit 3, interpreted as a likely aeolian deposit. *D*, Graph of grain-size distribution for samples from pit 3. All samples were predominantly well-sorted fine to medium sand.

threads, and irregularly shaped discontinuous carbonate masses were present at about 185 cm depth. From a depth of 85 cm (10 cm below the contact), sample IRSL-10 gave a date of 20.1 ± 2.7 ka. From a depth of 140 cm, sample IRSL-11 gave a date of 21.2 ± 1.6 ka. Thus, the two Pleistocene dates from the lower unit of pit 3 overlap within the analytical uncertainty range, and both were substantially older than the upper unit.

We considered the depositional environment in the lower part of pit 3 (75–190 cm depth) to be most likely alluvial, given the rapid accumulation rate implied by the two IRSL dates within this unit—55 cm of sediment accumulated with no discernible age difference between the lower and upper part of that deposit. The presence of well-rounded gravel indicates waterborne transport at some time in the past, although no fluvial sedimentary structures, bedding, or obvious sorting were seen that would have identified unaltered subaqueous deposits there. Similar to pit 2, we noted that in pit 3 the lithology and rounding of gravel clasts resembled the Pleistocene Colorado River gravels mapped to the east and the gravels of unit QTmm (Stone, 2006) flanking the northern Mule Mountains due south of pit 3. If gravel clasts did originate as Colorado River sediment, it is unclear whether the lower deposit at pit 3 is an intact Colorado River deposit or alluvial fan activity remobilized older Colorado River material from the QTmm of Stone (2006) deposits to the south. The occasional gravel-sized clasts within the lower unit of pit 3 were not concentrated into the type of gravel lag deposit that we observed on the modern interdune lag surfaces formed by wind deflation. We noted that the lower portion of pit 3 resembled the lower portion of pit 2 (90–200 cm depth in pit 2) in terms of sedimentary characteristics, although we considered it too indurated to sample for pIRIRSL dating and likely to have dose-rate complications owing to the abundance of pedogenic carbonate.

Above the unconformity at 75 cm depth, sediments are well sorted and laminated; we interpret that the dominant process forming that uppermost unit was aeolian deposition. This unit accumulated at a net rate of 0.02 cm/yr over recent millennia, based on the date and depth of sample IRSL-9. However, similar to our interpretation of the upper unit at pit 2, this topmost unit of pit 3 likely represents much faster accumulation owing to local dune migration, perhaps followed by subsequent deflation. Given the modern surface morphology and sedimentary characteristics, the sand sheet around pit 3 is inferred to experience ongoing minor aeolian inflation and deflation on the order of 10 cm vertically, similar to what we observed around the feet of our weather-station tripod, but with no geomorphic evidence of major recent inflation or deflation.

Pit 202 was excavated to a depth of 190 cm in a distal alluvial fan surface (elevation 117 m) inset into an older fan surface on the northeast side of the Mule Mountains (fig. 26). The fan upslope of this site is not one that drains ancestral Colorado River material (unit QTmm) from the Mule Mountains but is instead a fan (unit Qa3) with inset wash (unit Qw) that drains Jurassic volcanic bedrock (Stone, 2006; see fig. 1*C*). The surface of the fan is composed of coarse, subangular to subrounded igneous or low-grade metamorphic material (fig. 26*B*). We observed occasional well-rounded chert pebbles, but those were rare compared to the subangular igneous clasts. The fan morphology at the location of pit 202 includes small channels with minor incision (less than 10 cm). Incipient desert pavement is developed on gentle bar and swale topography that has an amplitude of 10–20 cm and wavelength of 3–4 m.

Sediment in pit 202 was poorly sorted, dominated by medium sand to gravel (fig. 26). The fan surface has minor desert pavement development and overlies a fine-grained, vesicular (Av) horizon immediately underneath (fig. 26*B*). Sediment in pit 202 was classified as 10YR 6/4 and 10YR 5/4 CK material that showed depositional bedding, but no major contacts. We did not define individual units for separate description but noted that individual coarser gravel and (or) pebble beds occurred at about 40–45 and 65–80 cm depths. We did not observe significant pedogenic carbonate cement in this pit, and no indurated carbonate clasts similar to those in pits 2 and 3 to the northwest were observed. Sample IRSL-7, between the two notable gravel beds, returned an early Holocene date of 11.2 ± 0.9 ka. Sample IRSL-8, from a depth of 180 cm, returned a late Pleistocene age of 22.2 ± 0.9 ka. We interpreted the deposits in pit 202 to represent alluvial fan activity. Minor contribution by aeolian sand deposition is possible, but no part of the section contained well-sorted sand or sedimentary structures that would have indicated aeolian deposition unequivocally. The average sediment accumulation rate between the two IRSL samples was calculated to be 0.1 cm/yr (110 cm in 11 k.y.). The more recent accumulation rate between sample IRSL-7 and the modern ground surface was calculated to be 0.006 cm/yr. Given the variable, episodic, and sometimes extreme drylands alluvial fan runoff and sediment delivery, we expect that sediment, in fact, accumulates rapidly and rarely at this location.

Pit 4 was dug by hand into the surface at the southwest side of polygon 4 (figs. 1*B*, 27). The surface morphology consists of a flat, uniform exposure of sand and gravel at elevation 115 m and is dotted with low-relief coppice dunes. Gravel patches are common and are interpreted as a lag deposit formed by wind reworking of material emplaced by distal alluvial fan activity and probably some aeolian deposition. Some exposures of faintly wind-rippled sand are also present. Clasts of the surface lag deposit include rounded chert clasts, and some appear similar to the igneous or low-grade metamorphic material on the surface by pit 202 (fig. 27*C*). Bioturbation was evident on the surface near pit 4 in the form of large burrows, which are common in this polygon. A burrowing owl was seen approximately 50 m away from the pit 4 location in March 2020.

Pit 4 was dug to a depth of 90 cm. The exposed material was classified as one massive unit that had no apparent bedding. The upper 2 cm were classified as an A1 horizon. An A2 horizon was identified from 2 to 12 cm depth, and a Ck horizon (indicating pedogenic carbonate) for the remainder of the section (12–90 cm depth). Color was 7.5YR 6/4 throughout the exposure. The sediment was weakly indurated and moderately sorted and was dominated by fine to coarse sand but contained some very coarse sand and gravel (fig. 27*D*–*F*). Some gravel clasts were coarse enough that they could not pass through the 22.6 mm gravelometer aperture (see grain-size distributions for sieved material in fig. 27*F*). The deposit did not appear to contain sedimentary

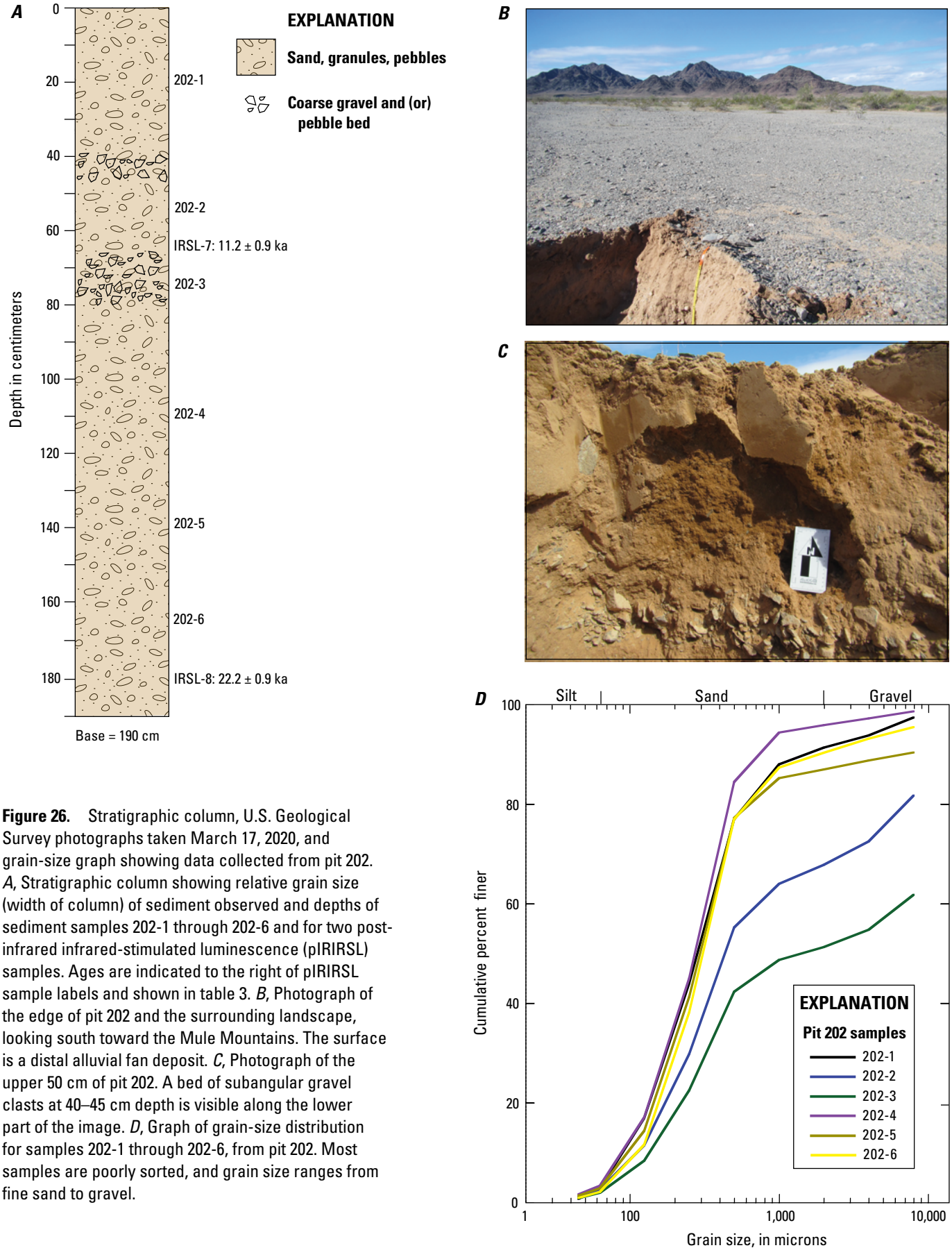

Figure 26. Stratigraphic column, U.S. Geological Survey photographs taken March 17, 2020, and grain-size graph showing data collected from pit 202. *A*, Stratigraphic column showing relative grain size (width of column) of sediment observed and depths of sediment samples 202-1 through 202-6 and for two post-infrared infrared-stimulated luminescence (pIRIRSL) samples. Ages are indicated to the right of pIRIRSL sample labels and shown in table 3. *B*, Photograph of the edge of pit 202 and the surrounding landscape, looking south toward the Mule Mountains. The surface is a distal alluvial fan deposit. *C*, Photograph of the upper 50 cm of pit 202. A bed of subangular gravel clasts at 40–45 cm depth is visible along the lower part of the image. *D*, Graph of grain-size distribution for samples 202-1 through 202-6, from pit 202. Most samples are poorly sorted, and grain size ranges from fine sand to gravel.

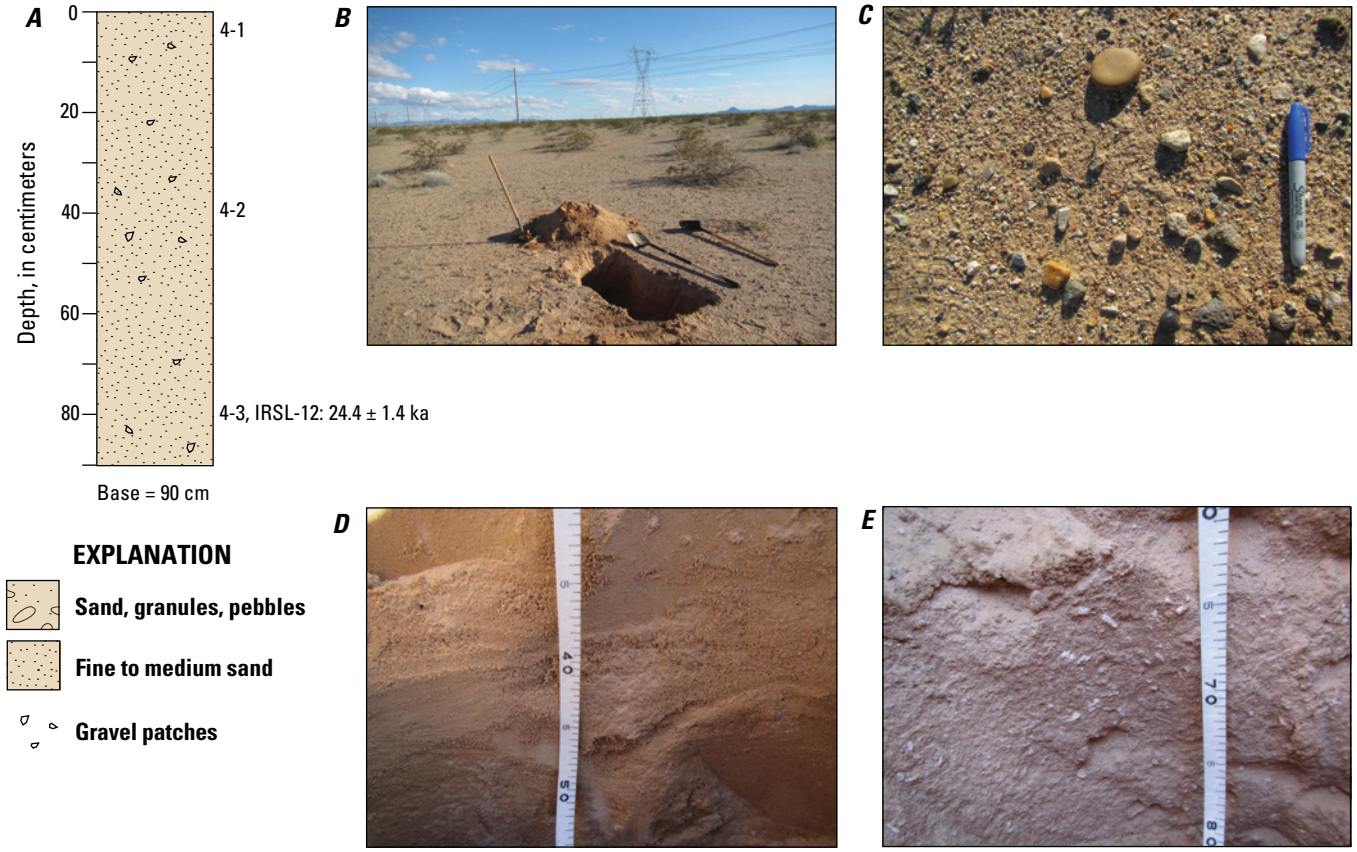

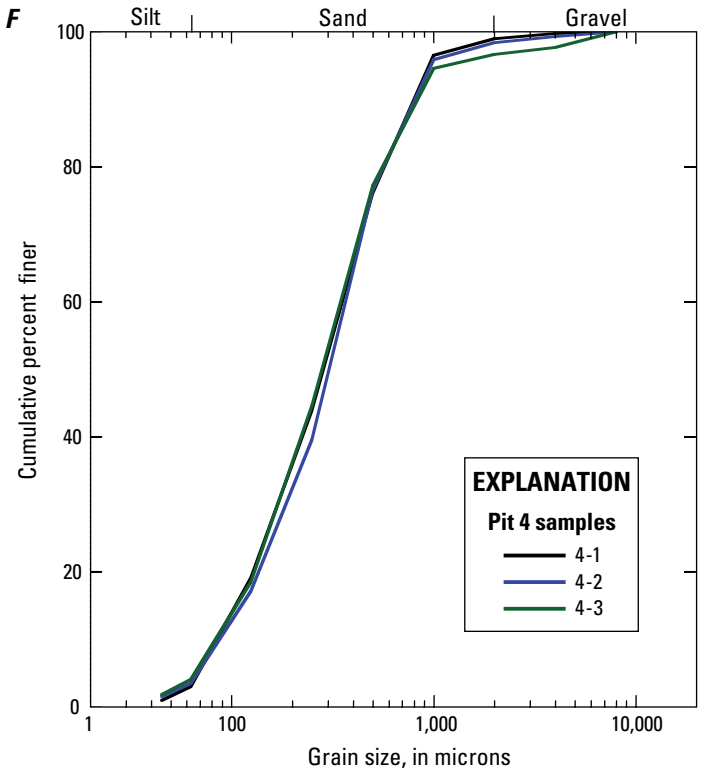

Figure 27. Stratigraphic column, U.S. Geological Survey photographs, and grain-size graph showing data collected from pit 4, excavated by hand on March 17, 2020, within polygon 4. *A*, Stratigraphic column showing relative grain size (width of column) of sediment observed and depths of sediment samples 4-1 through 4-3, and for one post-infrared infrared-stimulated luminescence (pIRIRSL) sample; its age is indicated to the right of its label and shown in table 3. *B*, Photograph of pit 4 and its surrounding landscape. *C*, Photograph of surface lag deposit adjacent to pit 4. The surface material includes well rounded pebbles, many of which are chert (pen for scale). *D*, Photograph of sand-dominated deposit within pit 4, shown from 31 to 52 cm below the surface. *E*, Photograph of sediment 60–80 cm below the surface in pit 4. White areas are carbonate material. *F*, Graph of grain-size distribution for samples from pit 4. All three samples (4-1 through 4-3) are composed mostly of well sorted fine to medium sand.

structures, which may have been obscured by bioturbation and carbonate precipitation. Aeolian deposition similar to the well-sorted aeolian sand on the uppermost part of pits 2 and 3 was not observed in pit 4. Although concentrated gravel lenses are not present in pit 4, the general appearance of material in pit 4 resembled that of the lower part of pit 202. Sample IRSL-12, from a depth of 80 cm, yielded a date of 24.4 ± 1.4 ka. If representing a long-term sediment accumulation rate, this would be equivalent to 0.003 cm/yr. However, there is no indication of recent sediment accumulation at or near pit 4, either in the form of aeolian inflation, dune migration, or recent alluvial fan activity. The well-developed lag surface and low-relief coppice dunes suggest a surface that probably has been relatively stable for centuries or longer. We interpreted the dominant sedimentary process at pit 4 to be aeolian mixed with distal alluvial fan deposition. Little alteration of surface morphology occurs there today, aside from rare distal alluvial fan deposition and minor reworking of sand into the coppice dunes.

Discussion

The geomorphic and sedimentary records in eastern Chuckwalla Valley reflect several hundred thousand years of landscape evolution and process interaction. The new stratigraphic and geochronologic data presented above demonstrate the varying local significance of aeolian, alluvial fan, lacustrine (playa), and possible Colorado River influence over a range of time scales. The pit 1 excavation, north of Interstate 10, revealed Pleistocene playa deposits (266–226 ka), overlain unconformably by alluvial fan strata (late Pleistocene to Holocene) with probably minor aeolian sediment contribution. The four sites we excavated in the central part of the eastern Chuckwalla Valley (pits 2, 3, 202, and 4) all contained strata that appeared to be predominantly alluvial, on the basis of grain size and sorting. Aeolian deposition formed the uppermost units of pits 2 and 3 (late to latest Holocene deposits less than 1 m thick) and probably also contributed some material to the alluvial strata, as is common in desert alluvial fan environments throughout the southern California desert and elsewhere (for example, Blair and McPherson, 2009).

Interestingly, four samples of alluvial sediment from three pits showed ages coincident with the Last Glacial Maximum (LGM): the ages of samples IRSL-10 and IRSL-11 from pit 3, sample IRSL-8 from pit 202, and sample IRSL-12 from pit 4 are generally within analytical uncertainty of each other and cluster around 23–21 ka. The ages of samples IRSL-10 and IRSL-11 (alluvial sediment in pit 3) indicated rapid sediment accumulation, potentially even as one depositional event at least 55 cm thick (table 3). Although the analytical uncertainty does not allow us to resolve whether these ages represented a single extreme storm that affected much of eastern Chuckwalla Valley, it is evident that alluvial sediment transport and deposition were active in this area around the LGM. This interpretation is consistent with previous studies having inferred a cooler climate at the LGM in the southwestern U.S. that was likely twice as wet as today (D'Arcy and others, 2017). During the LGM, large pluvial lakes existed about 100 km north of our study area in the Mojave Desert (Soda Lake basin) that formed around 22–21 ka, remained large until around 13 ka, and shrank to shallower playa conditions by 11 ka (Enzel and others, 2003; Reheis and others, 2012; and Honke and others, 2019).

Because of the common occurrence of well-rounded quartzite and chert-rich gravel clasts in the central to eastern part of Chuckwalla Valley (pits 2, 3, and 4), we surmised that ancestral Colorado River materials are an important sediment source to this area or were in the past. Delivery of Colorado River sediment most likely occurred by reworking of alluvial deposits (unit QTmm of Stone, 2006) on the north and northeast flanks of the Mule Mountains (fig. 1*C*), but possibly also by in situ deposition of flood sediment (sand and well-rounded gravel) finer than but coeval with the cobble-dominated Pleistocene Palo Verde Mesa deposits (unit Qpv of Stone, 2006). If the Colorado River formerly reached our study area to deposit the alluvial sediment we excavated, that would imply a past connection between Chuckwalla and Palo Verde Valleys, a possibility that future studies could investigate in more detail. In contrast to the well-rounded gravels in pits 2, 3, and 4 that may have been derived from the Colorado River, the prevalence of subangular igneous clasts at pit 202 reflects its location at the distal end of a wash with sediment sources dominated by older igneous bedrock in the Mule Mountains. Future investigations of sediment provenance could determine with more certainty what role recycled Colorado River sediment plays in modern sediment sources and recent stratigraphic evolution.

Earlier analyses by Kenney (2016) identified a transition from alluvial to aeolian deposition that occurred during early Holocene time (8 to 5 ka) in the area northeast of the Mule Mountains. Our data do not contradict that interpretation, but the unconformity we uncovered at pit 3 spanned more missing time than the transition; the uppermost preserved alluvial deposits are late Pleistocene (about 20 ka), whereas the base of preserved aeolian deposition was middle to late Holocene (about 4 ka; fig. 25), so our current findings cannot refine the age of that transition. At pits 202 and 4, northeast of the Mule Mountains, alluvial deposition remained dominant and no local transition to substantial aeolian activity was observed. At pit 1, the Holocene and recent alluvial fan activity was the only significant process post-dating much older Pleistocene lake sedimentation, and no substantial modern aeolian influence was apparent. Notably, Pease and Tchakerian (2003), who studied an aeolian sand ramp 50 km north of the Mule Mountains, identified periods of dry climate represented by aeolian sand deposition before 22 ka and between 15 and 6 ka, and development of paleosol (soil) units during the intervening times. The age of the 22–15 ka paleosol at the Big Maria sand ramp site of Pease and Tchakerian (2003) is consistent with our inference of wetter climate characterized by alluvial rather than aeolian deposition in eastern Chuckwalla Valley at the time of the LGM.

Our characterization of modern surficial processes and weather patterns in eastern Chuckwalla valley confirms long-standing recognition of a prevailing west-to-east wind regime in southwestern U.S. drylands (for example, Zimbleman and others,

1995; Muhs and others, 2003; Lancaster, 2020). The dominant sand-transport direction occurring in eastern Chuckwalla Valley is toward the northeast. However, occasional strong wind events from the north can transport large quantities of sand southward and temporarily reshape local geomorphic features, as we observed in late October 2019. Influence of a north to northwest wind direction is also locally dominant in the southeastern part of the Palen dune field, where dunes migrate toward the southwest owing to topographic steering of wind around mountain ranges. The existence and evolution of well-developed dunes in Chuckwalla Valley (most notably in polygon 7) are controlled by local topography; the dune field in polygon 7 is sourced from fluvial deposits in the Wiley Well wash depocenter immediately to the west, and eastward dune migration there is limited by a south-flowing alluvial channel draining from the McCoy Mountains. The polygon 7 dune field and the recycling of fluvial sand in the sand ramp on the west flank of the Mule Mountains (near polygon 6) are excellent examples of fluvial–aeolian interactions fundamentally controlling dryland morphology and sediment transport, as also occurs in other drylands globally (Langford, 1989; Rendell and others, 2003; Cohen and others, 2010; Belnap and others, 2011; East and others, 2015).

Therefore, if natural sand-transport corridors are to be maintained in eastern Chuckwalla Valley, then retaining the ability for sand to be transported eastward from the ephemeral stream channels and playas that supply sediment to the dunes, sand sheets, and sand ramps of Chuckwalla Valley would be needed and would allow for southward transport during episodic strong weather events. Although Kenney (2018) defined numerous local sand-migration pathways with discrete boundaries, we favor the perspective that sand-migration corridors do not have fixed boundaries and cannot readily be discretized over small spatial scales, especially after large, synoptic weather events. Rather, aeolian sediment-migration corridors are dynamic spatially and temporally, reorganizing based on seasonal changes to wind drift potential. A general framework of west-to-east winds produces sand migration that includes sediment from alluvial channels downwind to the east, occasionally and locally also to the south, and is recycled repeatedly between alluvial channels and aeolian deposits.

The modern sedimentary environment is key to the feasibility of maintaining solar-energy infrastructure. Land surfaces with greater sand mobility would be less stable, and therefore less feasible for development, than stable surfaces with little active aeolian sand. Today, the least feasible areas of eastern Chuckwalla Valley are those where dune migration is active (for example, polygon 7) or where, even without well-developed dunes, recent aeolian activity is evident from common wind rippled surfaces, sand shadows that form under strong winds, or thick aeolian deposits in the uppermost stratigraphy. Areas of low or limited feasibility include the zone mapped by Stone (2006) as unit Qs between Interstate 10 and the Mule Mountains (fig. 1*D*) and surrounding sparsely vegetated sand sheets, including the locations of pit 2, polygon 2, and pit 3. Areas within several kilometers downwind (east) of Wiley Well wash (including polygon 6) are expected to undergo seasonal- and event-scale inflation and deflation on the order of 10–40 cm. This estimate is based on landscape response to the October 2019 high wind event and our observations of seasonal exposure and reburial of the weather-station tripod legs. It is possible that altering vegetation cover and installing equipment on such a loose, sand-dominated surface could alter local wind dynamics to create new zones of deposition (eddies) around constructed materials. Portions of the landscape within active alluvial-fan channels or ephemeral washes can also be expected to destabilize during episodic high flow events.

It is also necessary to consider the likely response of the landscape and its vegetation to ongoing climate change, including the potential for increasing aeolian sand activity (East and Sankey, 2020). The southwestern U.S. is experiencing warmer and drier conditions today than several decades ago, a trend widely expected to continue (Seager and others, 2007; Cook and others, 2015; Diffenbaugh and others, 2015; USGCRP, 2017, 2018; Ullrich and others, 2018; Williams and others, 2020). Warming and drying lead to a decrease in the ratio of precipitation (P) to total annual potential evaporation (PE) as temperatures warm. As P/PE ratios decrease, vegetation cover decreases as plants have less available moisture. For example, decreased vegetation was observed during recent warming and severe drought in southern California (Dong and others, 2019). Vegetation is commonly a major factor limiting the availability of sand for aeolian transport (for example, Ash and Wasson, 1983; Buckley, 1987; Kocurek and Lancaster, 1999); another limiting factor is moisture, such as on playa surface, which prevents sediment from being entrained by wind. Thus, large dryland areas that are now sediment-supply limited by being sparsely vegetated or seasonally wetted could transition to greater aeolian activity in a warmer climate as stabilizing vegetation cover and playa moisture are reduced (Muhs and Maat, 1993; Muhs and Holliday, 1995; Lancaster, 1997; Muhs and Been, 1999; Lancaster and Helm, 2000; Pelletier, 2006; Pelletier and others, 2009; Yizhaq and others, 2009; Duniway and others, 2019; Redsteer, 2020). Increased dune activity has been documented in some western U.S. dune fields during drought in recent decades (Marín and others, 2005; Bogle and others, 2015). More frequent and intense dust storms are also likely and represent one of the largest expected economic effects of climate change in the U.S. (Achakulwisut and others, 2019). More extreme rain events in a warmer climate (for example, Allan and Soden, 2008; Intergovernmental Panel on Climate Change, 2014; Swain and others, 2018) presumably would supply more sediment to aeolian source regions, such as Wiley Well wash and the alluvial fans upslope of polygon 8 or pit 202. The least stable landscapes of eastern Chuckwalla Valley in future climate will likely be those immediately downwind of ephemeral stream channels and their depocenter (playa) regions, which will supply aeolian sand to downwind regions in possibly greater quantities than today, and with less vegetation to stabilize the aeolian sand sheets compared to today. Areas that are generally stable today—those areas far enough from major stream channels to receive reduced aeolian sediment supply with little evidence of substantial aeolian sand activity in the past, such as northeast of the Mule Mountains—may be affected by aeolian dust under future climate even if surface geomorphic changes remain negligible.

Conclusions

Our weather records and sand-transport modeling results indicate that, given unlimited sediment supply, wind in eastern Chuckwalla Valley is capable of transporting approximately 10^5 kilograms (100 metric tons) of sand per meter width per year. The same order of magnitude sediment flux would occur as a dune of the size found in Chuckwalla Valley (3–4 m high, 30–60 m wide, and 25–35 m long) migrates past a fixed point; the wind regime is sufficient to transport that quantity of sand annually at a given location if enough sediment is available and unimpeded by vegetation. Feasible development of solar energy facilities will depend upon sediment availability and dust generation remaining low enough locally to minimize disruption to infrastructure.

Stratigraphic profiles at five sites along a northwest-to-southeast transect revealed Pleistocene playa deposits (dating to 266–226 ka) south of the McCoy Mountains and immediately north of Interstate 10, overlain by late Pleistocene to Holocene alluvial fan deposits. To the southeast (south of Interstate 10, but north of the Mule Mountains), we identified rapid accumulation of alluvial sediment around the time of the Last Glacial Maximum (23–20 ka), unconformably overlain by recent and Holocene aeolian and alluvial fan sediment. We have used stratigraphic characteristics and luminescence ages to calculate accumulation rates for these sites, identifying spatial variation in landscape stability over decadal and longer time scales.

Future investigations of landscape evolution in Chuckwalla Valley could include geochemical and mineralogic analyses to infer sediment-transport pathways in greater detail and provide information that could refine identification of feasible sites for solar-energy development. The role of vegetation cover in modulating aeolian sediment entrainment and transport would also be worthwhile to examine through further field study, particularly the role of nonnative plant species. Although some exotic plant species grow to cover large areas rapidly, they may not provide long-term stability to sandy surfaces (for example, Draut and others, 2012), and windblown sediment pulses can still occur if vegetation life cycles are out of phase with the most active seasonal wind regime. The development of effective solar facilities would benefit from a thorough understanding of regional geomorphic and sedimentary processes as well as the ways in which these processes interact with the ecosystem to shape the landscape.

Acknowledgments

This study was supported by funding from the Bureau of Land Management. We thank James Weigand and Andrew Johnson for their logistical assistance and for sharing their knowledge of the study region. Reviewers Andrew Cyr and Kyle House provided valuable comments that improved the report. The authors thank Angela Tan, Miranda Baker, and Gideon East for help with grain-size analysis, Phil Frederick for detailed editing of the manuscript, and Cory Hurd for graphics assistance and layout. Digital data associated with this report will be made available for download as a USGS data release from: https://doi.org/10.5066/P9LZ02E4.

References Cited

Achakulwisut, P., Anenberg, S.C., Neumann, J.E., Penn, S.L., Weiss, N., Crimmins, A., Fann, N., Martinich, J., Roman, H., and Mickley, L.J., 2019, Effects of increasing aridity on ambient dust and public health in the U.S. Southwest under climate change: GeoHealth, v. 3, p. 127–144, accessed February 2, 2021, at https://doi.org/10.1029/2019GH000187.

AghaKouchak, A., Cheng, L., Mazdiyasni, O., and Farahmand, A., 2014, Global warming and changes in risk of concurrent climate extremes—insights from the 2014 California drought: Geophysical Research Letters, v. 41, p. 8,847–8,852, accessed February 2, 2021, at https://doi.org/10.1002/2014GL062308.

Allan, R.P., and Soden, B.J., 2008, Atmospheric warming and the amplification of precipitation extremes: Science, v. 321, no. 5895, p. 1,481–1,484, accessed February 2, 2021, at https://doi.org/10.1126/science.1160787.

Ash, J.E., and Wasson, R.J., 1983, Vegetation and sand mobility in the Australian desert dunefield: Zeitschrift für Geomorphologie, supplement, v. 45, p. 7–25.

Auclair, M., Lamothe, M., and Huot, S., 2003, Measurement of anomalous fading for feldspar IRSL using SAR: Radiation Measurements, v. 37, no. 4–5, p. 487–492.

Bagnold, R.A., 1941, The physics of blown sand and desert dunes (4th ed.): London, Chapman and Hall, 265 p.

Barth, N.A., Villarini, G., and White, K., 2018, Contribution of eastern North Pacific tropical cyclones and their remnants on flooding in the western United States: International Journal of Climatology, v. 38, p. 5,441–5,446, accessed February 2, 2021, at https://doi.org/10.1002/joc.5735.

Bauer, B.O., Davidson-Arnott, R.G.D., Nordstrom, K.F, Ollerhead, J., and Jackson, N.L., 1996, Indeterminacy in aeolian sediment transport across beaches: Journal of Coastal Research, v. 12, p. 641–653.

Beck, H.E., Zimmermann, N.E., McVicar, T.R., Vergopolan, N., Berg, A., and Wood, E.F., 2018, Present and future Köppen-Geiger climate classification maps at 1-km resolution: Scientific Data, v. 5, no. 180214, accessed February 2, 2021, at https://doi.org/10.1038/sdata.2018.214.

Belnap, J., Munson, S.M., and Field, J.P., 2011, Aeolian and fluvial processes in dryland regions: the need for integrated studies: Ecohydrology, v. 4, p. 615–622.

Biondi, F., and Meko, D.M., 2019, Long-term hydroclimatic patterns in the Truckee-Carson basin of the eastern Sierra Nevada, USA: Water Resources Research, v. 55, p. 5,559–5,574, accessed February 2, 2021, at https://doi.org/10.1029/2019WR024735.

Blair, T.C., and McPherson, J.G., 2009, Processes and forms of alluvial fans, chap. 14 of Parsons, A.J., and Abrahams, A.D., eds., Geomorphology of desert environments (2d ed.): Dordrecht, Netherlands, Springer, p. 413–467.

Block, D., Gootee, B.F., House, P.K., and Pearthree, P.A., 2019, Geologic map of the Blythe 7 1/2' quadrangle, La Paz County, Arizona and Riverside County, California: Arizona Geological Survey Digital Geologic Map 124, 2 sheets, 45 p., scale 1:24,000. [Also available at http://hdl.handle.net/10150/636492.]

Bogle, R., Redsteer, M.H., and Vogel, J., 2015, Field measurement and analysis of climatic factors affecting dune mobility near Grand Falls on the Navajo Nation, southwestern United States: Geomorphology, v. 228, p. 41–51, http://doi.org/10.1016/j.geomorph.2014.08.023.

Buckley, R., 1987, The effect of sparse vegetation on the transport of dune sand by wind: Nature, v. 325, p. 426–428.

Carr, A.S., Hay, A.S., Powell, D.M., and Livingstone, I., 2019, Testing post-IR IRSL luminescence dating methods in the southwest Mojave Desert, California, USA: Quaternary Geochronology, v. 49, p. 85–91.

Clarke, M.L., and Rendell, H.M., 1998, Climate change impacts on sand supply and the formation of desert sand dunes in the south-west U.S.A.: Journal of Arid Environments, v. 39, p. 517–531.

Cohen, T.J., Nanson, G.C., Larsen, J.R., Jones, B.G., Price, D.M., Coleman, M., and Pietsch, T.J., 2010, Late Quaternary aeolian and fluvial interactions on the Cooper Creek Fan and the association between linear and source-bordering dunes, Strzelecki Desert, Australia: Quaternary Science Reviews, v. 29, p. 255–471.

Cook, B.I., Ault, T.R., and Smerdon, J.E., 2015, Unprecedented 21st century drought risk in the American Southwest and Central Plains: Science Advances, v.1, no. 1, 7 p., https://doi.org/10.1126/sciadv.1400082.

Crow, R.S., Block, D., Felger, T.J., House, P.K., Pearthree, P.A., Gootee, B.F., Youberg, A.M., Howard, K.A., and Beard, L.S., 2018, The Colorado River and its deposits downstream from Grand Canyon in Arizona, California, and Nevada: U.S. Geological Survey Open-File Report 2018–1005, 6 p., https://doi.org/10.3133/ofr20181005.

D'Arcy, M., Roda-Boluda, D.C., and Whittaker, A.C., 2017, Glacial-interglacial climate changes recorded by debris flow fan deposits, Owens Valley, California: Quaternary Science Reviews, v. 169, p. 288–311, accessed February 2, 2021, at https://doi.org/10.1016/j.quascirev.2017.06.002.

Diffenbaugh, N.S., Swain, D.L., and Touma, D., 2015, Anthropogenic warming has increased drought risk in California: Proceedings of the National Academy of Sciences, v. 112, no. 13, p. 3,931–3,936, accessed February 2, 2021, at https://doi.org/10.1073/pnas.1422385112.

Dong, C., MacDonald, G.M., Willis, K., Gillespie, T.W., Okin, G.S., and Williams, A.P., 2019, Vegetation responses to 2012–2016 drought in northern and southern California: Geophysical Research Letters , v. 46, p. 3,810–3,821, accessed February 2, 2021, at https://doi.org/10.1029/2019GL082137.

Draut, A.E., Redsteer, M.H., and Amoroso, L., 2012, Recent seasonal variations in arid landscape cover and aeolian sand mobility, Navajo Nation, southwestern United States, in Giosan, L., Fuller, D.Q., Nicoll, K., Flad, R.K., and Clift, P.D., eds., Climate, Landscapes and Civilizations: American Geophysical Union, Geophysical Monograph 198, p. 51–60, https://doi.org/10.1029/2012GM001214.

Draut, A.E., and Rubin, D.M., 2008, The role of eolian sediment in the preservation of archeologic sites along the Colorado River corridor in Grand Canyon National Park, Arizona: U.S. Geological Survey Professional Paper 1756, 79 p., accessed February 2, 2021, at https://pubs.usgs.gov/pp/1756/.

Draut, A.E., Rubin, D.M., Dierker, J.L., Fairley, H.C., Griffiths, R.E., Hazel, J.E. Jr., Hunter, R.E., Kohl, K., Leap, L.M., Nials, F.L., Topping, D.J., and Yeatts, M., 2008, Application of sedimentary-structure interpretation to geoarchaeological investigations in the Colorado River corridor, Grand Canyon, Arizona, USA: Geomorphology, v. 101, p. 497–509.

Duniway, M.C., Pfennigwerth, A.A., Fick, S.E., Nauman, T.W., Belnap, J., and Barger, N.N., 2019, Wind erosion and dust from US drylands: a review of causes, consequences, and solutions in a changing world: Ecosphere, v. 10, no. 3, 28 p.

Durán, O., Claudin, P., and Andreotti, B., 2011, On aeolian transport—Grain-scale interactions, dynamical mechanisms and scaling laws: Aeolian Research, v. 3, p. 243–270.

Durcan, J.A., King, G.E., and Duller, G.A., 2015, DRAC—Dose rate and age calculator for trapped charge dating: Quaternary Geochronology, v. 28, p. 54–61. [Also available at https://doi.org/10.1016/j.quageo.2015.03.012.]

East, A.E., and Sankey, J.B., 2020, Geomorphic and sedimentary effects of modern climate change: current and anticipated future conditions in the western United States: Reviews of Geophysics, v.58, no. 4, 59 p., accessed February 2, 2021, at https://doi.org/10.1029/2019RG000692.

East, A.E., Clift, P.D., Carter, A., Alizai, A., and VanLaningham, S., 2015, Fluvial–eolian interactions in sediment routing and sedimentary signal buffering: an example from the Indus Basin and Thar Desert: Journal of Sedimentary Research, v. 85, p. 715–728.

Enzel, Y., Wells, S.G., and Lancaster, N., 2003, Late Pleistocene lakes along the Mojave River, southeast California: Geological Society of America Special Paper 368, p. 61–77.

Everett, R.R., Brown, A.A., and Smith, G.A., 2013, Chuckwalla Valley multiple-well monitoring site, Chuckwalla Valley, Riverside County, California: U.S. Geological Survey Open-File Report 2013–1221, accessed February 2, 2021, at https://pubs.usgs.gov/of/2013/1221/.

Galbraith, R.F., and Roberts, R.G., 2012, Statistical aspects of equivalent dose and error calculation and display in OSL dating; an overview and some recommendations: Quaternary Geochronology, v. 11, p. 1–27.

Gray, H.J., and East, A.E., 2021, Luminescence, weather, and grain-size data from eastern Chuckwalla Valley, Riverside County, California: U.S. Geological Survey data release, https://doi.org/10.5066/P9LZ02E4.

Gray, H.J., Mahan, S.A., Nelson, M.S., and Rittenour, T.M., 2015, Guide to luminescence dating techniques and their application for paleoseismic research, in Lund, W.R., ed., Proceedings volume, Basin and Range Province Seismic Hazards Summit III: Utah Geological Survey Miscellaneous Publication, v. 15-5, invited paper, 18 p. [Also available at, https://ugspub.nr.utah.gov/publications/misc_pubs/mp-15-5/mp-15-5_invited_paper.pdf.]

Gray, H.J., Jain, M., Sawakuchi, A.O., Mahan, S.A., and Tucker, G.E., 2019, Luminescence as a sediment tracer and provenance tool: Reviews of Geophysics, v. 57, no. 3, p. 987–1017, accessed February 2, 2021, at https://doi.org/10.1029/2019RG000646.

Griffin, D., and Anchukaitis, K.J., 2014, How unusual is the 2012–2014 California drought?: Geophysical Research Letters, v. 41, p. 9,017–9,023, accessed February 2, 2021, at https://doi.org/10.1002/2014GL062433.

Griffiths, P.G., Magirl, C.S., Webb, R.H., Pytlak, E., Troch, P.A., and Lyon, S.W., 2009, Spatial distribution and frequency of precipitation during an extreme event—July 2006 mesoscale convective complexes and floods in southeastern Arizona: Water Resources Research, v. 45, W07419, 14 p., accessed February 2, 2021, at https://doi.org/10.1029/2008WR007380.

Guilinger, J.J., Gray, A.B., Barth, N.C., and Fong, B.T., 2020, The evolution of sediment sources over a sequence of post-fire sediment-laden flows revealed through repeat high-resolution change detection: Journal of Geophysical Research-Earth Surface, v. 125, no. 10, 23 p., accessed Febraury 2, 2021, at https://doi.org/10.1029/2020JF005527.

Harvey, A.M., Wigand, P.E., and Wells, S.G., 1999, Response of alluvial fan systems to the late Pleistocene to Holocene climatic transition—contrasts between the margins of pluvial Lakes Lahontan and Mojave, Nevada and California, USA: Catena, v. 36, p. 255–281.

Hatchett, B.J., Boyle, D.P., Putnam, A.E., and Bassett, S.D., 2015, Placing the 2012–2015 California-Nevada drought into a paleoclimatic context—Insights from Walker Lake, California-Nevada, USA: Geophysical Research Letters, v. 42, p. 8,632–8,640, accessed February 2, 2021, at https://doi.org/10.1002/2015GL065841.

Hatchett, B.J., Cao, Q., Dawson, P.B., Ellis, C.J., Hecht, C.W., Kawzenuk, B., Lancaster, J.T., Osborne, T.C., Wilson, A.M., and 11 others, 2020, Observations of an extreme atmospheric river storm with a diverse sensor network: Earth and Space Science, v. 7, no. 8, 21 p., accessed February 2, 2021, at https://doi.org/10.1029/2020EA001129.

Hereford, R., Webb, R.H., and Longpre, C.I., 2006, Precipitation history and ecosystem response to multidecadal precipitation variability in the Mojave Desert region, 1893–2001: Journal of Arid Environments, v. 67, p. 13–34.

Honke, J.S., Pigati, J.S., Wilson, J., Bright, J., Goldstein, H.L., Skipp, G.L., Reheis, M.C., and Havens, J.C., 2019, Late Quaternary paleohydrology of desert wetlands and pluvial lakes in the Soda Lake basin, central Mojave Desert, California (USA): Quaternary Science Reviews, v. 216, p. 89–106, accessed February 2, 2021, at https://doi.org/10.1016/j.quascirev.2019.05.021.

Intergovernmental Panel on Climate Change [IPCC], 2014, Climate Change 2014; Synthesis Report in Core Writing Team, R.K. Pachauri and L.A. Meyer, eds., Contribution of working groups I, II and III to the Fifth Assessment Report of the Intergovernmental Panel on Climate Change: Geneva, Switzerland, IPCC, 151 p., accessed February 2, 2021, at https://www.ipcc.ch/report/ar5/syr/.

Kawamura, R., 1951, Study of sand movement by wind: University of Tokyo, Institute of Science and Technology Report, v. 5 no. 3–4, p. 95–112. [in Japanese.]

Kenney, M.D., 2016, Geomorphic and stratigraphic evaluation of the stable early to mid-Holocene eolian (windblown dune systems for proposed Desert Quartzite Solar Project, eastern Chuckwalla Valley and Palo Verde Mesa area, Riverside County, California: First Solar, report prepared by Kenney GeoScience, Job No. 721-11, 170 p.

Kenney, M.D., 2018, Geomorphic and stratigraphic evaluation of stable early to mid-Holocene eolian (windblown) dune systems for proposed Crimson Solar Project, eastern Chuckwalla Valley, Riverside County, California: AECOM Crimson Solar Project, report prepared by Kenney GeoScience, Job No. 737-16, 207 p.

Kocurek, G., and Lancaster, N., 1999, Aeolian system sediment state: theory and Mojave Desert Kelso dune field example: Sedimentology, v. 46, p. 505–515.

Kok, J.F., Parteli, E.J.R., Michaels, T.I., and Karam, D.B., 2012, The physics of wind-blown sand and dust: Reports on Progress in Physics, v. 75, no. 10, 106901, 119 p., accessed February 2, 2021, at https://doi.org/10.1088/0034-4885/75/10/106901.

Kreutzer, S., Schmidt, C., Fuchs, M.C., Dietze, M., Fischer, M., and Fuchs, M., 2012, Introducing an R package for luminescence dating analysis: Ancient TL, Luminescence Dosimetry Laboratory, v. 30, no. 1, p. 1–8.

Lancaster, N., 1997, Response of eolian geomorphic systems to minor climate change: examples from the southern Californian deserts: Geomorphology, v. 19, p. 333–347.

Lancaster, N., 2020, Dunefields of the Southwest Deserts, Chap. 9 of Lancaster, N., and Hesp, P., eds., Inland Dunes of North America: Gewerbestrasse, Switzerland, Springer, p. 311–337.

Lancaster, N., and Helm, P., 2000, A test of a climatic index of dune mobility using measurements from the southwestern United States: Earth Surface Processes and Landforms, v. 25, p. 197–208.

Lancaster, N., and Tchakerian, V.P., 2003, Late Quaternary eolian dynamics, Mojave Desert, California in Enzel, Y., Wells, S.G., and Lancaster, N., eds., Paleoenvironments and paleohydrology of the Mojave and southern Great Basin deserts: Geological Society of America Special Paper 368, p. 231–249.

Langford, R.P., 1989, Fluvial-aeolian interactions—Part I, modern systems: Sedimentology, v. 36, no. 6, p. 1,023–1,035.

Lawson, M.J., Roder, B.J., Stang, D.M., and Rhodes, E.J., 2012, OSL and IRSL characteristics of quartz and feldspar from southern California, USA: Radiation Measurements, v. 47, no. 9, p. 830–836.

Lee, S.-K., Lopez, H., Chung, E.-S., DiNezio, P., Yeh, S.-W., and Wittenberg, A.T., 2018, On the fragile relationship between El Niño and California rainfall: Geophysical Research Letters, v. 45, p. 907–915, accessed February 2, 2021, at https://doi.org/10.1002/2017GL076197.

Li, B., Jacobs, Z., Roberts, R.G., and Li, S.H., 2014, Review and assessment of the potential of post-IR IRSL dating methods to circumvent the problem of anomalous fading in feldspar luminescence: Geochronometria, v. 41, no. 3, p. 178–201.

Maddox R.A., McCollum, D.M., and Howard, K.W., 1995, Large-scale patterns associated with severe summertime thunderstorms over central Arizona: Weather and Forecasting, v. 10, p. 763–778. [Also available at https://doi.org/10.1175/1520-0434(1995)010%3C0763:LSPAWS%3E2.0.CO;2.]

Marín, L., Forman, S.L., Valdez, A., and Bunch, F., 2005, Twentieth century dune migration at the Great Sand Dunes National Park and Preserve, Colorado, relation to drought variability: Geomorphology, v. 70, p. 163–183.

Menke, J., Reyes, E., Hepburn, A., Johnson, D., and Reyes, J., 2016, California vegetation map in support of the desert renewable energy conservation plan (2014–2016 additions): California Department of Fish and Wildlife Renewable Energy Program and the California Energy Commission, report prepared by Aerial Information Systems, Inc., 322 p., accessed October 28, 2020, at https://www.cnps.org/wp-content/uploads/2019/01/veg-drecp-map-accuracy-report-2016-additions.pdf.

Metzger, D.G., Loeltz, O.J., and Irelna, B., 1973, Geohydrology of the Parker-Blythe-Cibola area, Arizona and California: U.S. Geological Survey Professional Paper 486-G, 130 p.

Miller, D.M., Schmidt, K.M., Mahan, S.A., McGeehin, J.P., Owen, L.A., Barron, J.A., Lehmkuhl, F., and Löhrer, R., 2010, Holocene landscape response to seasonality of storms in the Mojave Desert: Quaternary International, v. 215, p. 45–61, accessed February 2, 2021, at https://doi.org/10.1016/j.quaint.2009.10.001.

Muhs, D.R., and Been, J.M., 1999, Reactivation of stabilized sand dunes on the Colorado Plateau: U.S. Geological Survey, accessed September 15, 2020, at https://geochange.er.usgs.gov/sw/impacts/geology/sand/.

Muhs, D.R., and Holliday, V.T., 1995, Evidence of active dune sand on the great plains in the 19th century from accounts of early explorers: Quaternary Research, v. 43, p. 198–208.

Muhs, D.R., and Maat, P.B., 1993, The potential response of eolian sands to greenhouse warming and precipitation reduction on the Great Plains of the U.S.A.: Journal of Arid Environments, v. 25, p. 351–361.

Muhs, D.R., Reynolds, R.L., Been, J., and Skipp, G., 2003, Eolian sand transport pathways in the southwestern United States; importance of the Colorado River and local sources: Quaternary International, v. 104, p. 3–18.

National Oceanic and Atmospheric Administration, 2020a, Daily summaries station details [Blythe, California]: National Oceanic and Atmospheric Administration database, accessed October 14, 2020, at https://www.ncdc.noaa.gov/cdo-web/datasets/GHCND/stations/GHCND:USC00040924/detail.

National Oceanic and Atmospheric Administration, 2020b, Daily summaries station details [Blythe ASOS, California]: National Oceanic and Atmospheric Administration database accessed February 3, 2021, at https://www.ncdc.noaa.gov/cdo-web/datasets/GHCND/stations/GHCND:USW00023158/detail.

Nials, F., Tennyson, M., Hintzman, M., LaVictoire, T., and Weidlich, S., 2013, Landform structure and archaeological sensitivity for the Palen solar electric generating system project, Riverside County, California: U.S. Department of Interior, Bureau of Land Management, Report no. 2013-60301380 prepared by AECOM, Inc., 48 p.

Parameter-elevation Regression on Independent Slopes Model [PRISM] Climate Group, 2020, Climate data: Oregon State University web page, accessed September 24, 2020, at https://prism.oregonstate.edu/normals/.

Parsons, A.J., and Abrahams, A.D., 2009, Geomorphology of desert environments (2d ed.): Dordrecht, Netherlands, Springer, 831 p.

Pease, P.P., and Tchakerian, V.P., 2003, Geochemistry of sediments from Quaternary sand ramps in the southeastern Mojave Desert, California: Quaternary International, v. 104, p. 19–29.

Pelletier, J.D., 2006, Sensitivity of playa windblown-dust emissions to climatic and anthropogenic change: Journal of Arid Environments, v. 66, p. 62–75, accessed February 2, 2021, at https://doi.org/10.1016/j.jaridenv.2005.10.010.

Pelletier, J. D., Mitasova, H., Harmon, R. S., and Overton, M., 2009, The effects of interdune vegetation changes on eolian dune field evolution; a numerical-modeling case study at Jockey's Ridge, North Carolina, USA: Earth Surface Processes and Landforms, v. 34, p. 1,245–1,254, accessed February 2, 2021 at, https://doi.org/10.1002/esp.1809.

Potter, C., and Wiegand, J., 2016, Analysis of desert sand dune migration patterns from Landsat image time series for the southern California desert: Journal of Remote Sensing and GIS, v. 5, no. 2, 1000164, 8 p, accessed February 2, 2021, at http://doi.org/10.4172/2469-4134.1000164.

Redsteer, M.H., 2020, Sand dunes, climate and sediment supply on tribal lands of the southern Colorado Plateau, chap. 8 of Lancaster, N., and Hesp, P., eds., Inland Dunes of North America: Gewerbestrasse, Switzerland, Springer, p. 287–310.

Reheis, M.C., and Kihl, R., 1995, Dust deposition in southern Nevada and California, 1984–1989; relations to climate, source area, and source lithology: Journal of Geophysical Research, v. 100, no. D5, p. 8,893–8,918.

Reheis, M.C., Bright, J., Lund, S.P., Miller, D.M., Skipp, G., and Fleck, R.J., 2012, A half-million-year record of paleoclimate from the Lake Manix core, Mojave Desert, California: Palaeogeography, Palaeoclimatology, Palaeoecology, v. 365–366, p. 11–37.

Rendell, H.M., Clarke, M.L., Warren, A., and Chappell, A., 2003, The timing of climbing dune formation in southwestern Niger; fluvio-aeolian interactions and the role of sand supply: Quaternary Science Reviews, v. 22, p. 1,059–1,065.

Reynolds, R.L., Yount, J.C., Reheis, M., Goldstein, H., Chavez, P., Fulton, R., Whitney, J., Fuller, C., and Forester, R.M., 2007, Dust emission from wet and dry playas in the Mojave Desert, USA: Earth Surface Processes and Landforms, v. 32, p. 1,811–1,827, accessed February 2, 2021, at https://doi.org/10.1002/esp.1515.

Roubeyrie, L., and Celles, S., 2018, Windrose; a Python Matplotlib, Numpy library to manage wind and pollution data, draw windrose: Journal of Open Source Software, v. 3, no. 29, p. 268.

Rubin, D.M., and Hunter, R.E., 1982, Bedform climbing in theory and nature: Sedimentology, v. 29, p. 121–138.

Rubin, D.M., and Hunter, R.E., 1987, Field guide to sedimentary structures in the Navajo and Entrada Sandstones in southern Utah and northern Arizona: Arizona Bureau of Geology and Mineral Technology, Special Paper, v. 5., p. 126–139.

Seager, R., Ting, M., Held, I., Kushnir, Y., Lu, J., Vecchi, G., Huang, H.-P., Harnik, N., Leetmaa, A., Lau, N.-C., Li, C., Velez, J., and Naik, N., 2007, Model projections of an imminent transition to a more arid climate in southwestern North America: Science, v. 316, p. 1,181–1,184.

Sherrod, D.R., and Tosdal, R.M., 1991, Geologic setting and Tertiary structural evolution of southwestern Arizona and southeastern California: Journal of Geophysical Research, v. 96, no. B7, p. 12,407–12,423.

Stone, P.A., 2006, Geologic map of the west half of the Blythe 30' by 60' quadrangle, Riverside County, California, and La Paz County, Arizona: U.S. Geological Survey Scientific Investigations Map 2922, 1 sheet, scale 1:100,000. [Also available at https://pubs.usgs.gov/sim/2006/2922/SIM2922_map.pdf.]

Stone, P.A., and Kelly, M.M., 1989, Geologic map of the Palen Pass quadrangle, Riverside County, California: U.S. Geological Survey Miscellaneous Field Studies Map MF-2070, https://doi.org/10.3133/mf2070.

Swain, D.L., Langenbrunner, B., Neelin, J.D., and Hall, A., 2018, Increasing precipitation volatility in twenty-first-century California: Nature Climate Change, v. 8, p. 427–433, accessed February 2, 2021, at https://doi.org/10.1038/s41558-018-0140-y.

Thiel, C., Buylaert, J.P., Murray, A., Terhorst, B., Hofer, I., Tsukamoto, S., and Frechen, M., 2011, Luminescence dating of the Stratzing loess profile (Austria)–Testing the potential of an elevated temperature post-IR IRSL protocol: Quaternary International, v. 234, no. 1–2, p. 23–31.

Thomsen, K.J., Murray, A.S., Jain, M., and Bøtter-Jensen, L., 2008, Laboratory fading rates of various luminescence signals from feldspar-rich sediment extracts: Radiation Measurements, v. 43, no. 9–10, p. 1,474–1,486.

Ullrich, P.A., Xu, Z., Rhoades, A.M., Dettinger, M.D., Mount, J.F., Jones, A.D., and Vahmani, P., 2018, California's drought of the future—A midcentury recreation of the exceptional conditions of 2012—2017: Earth's Future, v. 6, p. 1,568—1,587, accessed February 2, 2021, at https://doi.org/10.1029/2018EF001007.

U.S. Global Change Research Program [USGCRP], 2017, Climate Science Special Report, in Wuebbles, D.J., Fahey, D.W., Hibbard, K.A., Dokken, D.J., Stewart, B.C., and Maycock, T.K., eds., Fourth National Climate Assessment, Volume I: Washington, D.C., U.S. Global Change Research Program, 470 p., accessed February 2, 2021, at https://doi.org/10.7930/J0J964J6.

U.S. Global Change Research Program [USGCRP], 2018, Impacts, risks, and adaptation in the United States, in Reidmiller, D.R., Avery, C.W., Easterling, D.R., Kunkel, K.E., Lewis, K.L.M., Maycock, T.K., and Stewart, B.C., eds., Fourth National Climate Assessment, Volume II: Washington, D.C., U.S. Global Change Research Program, 1,515 p., accessed February 2, 2021, at https://doi.org/10.7930/NCA4.2018.

Williams, A.P., Cook, E.R., Smerdon, J.E., Cook, B.I., Abatzoglou, J.T., Bolles, K., Baeik, S.H., Badger, A.M., and Livneh, B., 2020, Large contribution from anthropogenic warming to an emerging North American megadrought: Science, v. 368, p. 314–318.

Yizhaq, H., Ashkenazy, Y., and Tsoar, H., 2009, Sand dune dynamics and climate change; a modeling approach: Journal of Geophysical Research, Earth Surface, v. 114, 11 p., accessed February 2, 2021, at https://doi.org/10.1029/2008JF001138.

Young, A. M., Skelly, K. T., and Cordeira, J. M., 2017, High-impact hydrologic events and atmospheric rivers in California—an investigation using the NCEI storm events database: Geophysical Research Letters, v. 44, p. 3,393–3,401, accessed February 2, 2021, at https://doi.org/10.1002/2017GL073077.

Zimbleman, J.R., Williams, S.H., and Tchakerian, V.P., 1995, Sand transport paths in the Mojave Desert, southwestern United States, in Tchakerian, V.P., ed., Desert Aeolian Processes: London, Chapman and Hall, p. 101–129.

Zingg, A.W., 1953, Wind tunnel studies of the movement of sedimentary material, in Proceedings of the 5th Hydraulic Conference Bulletin (Studies in Engineering, v. 34): Iowa City, Iowa State University, p. 111–135.

Glossary of Selected Terms

Aeolian pertaining to wind (also spelled eolian).

Alluvial fan a fan- or cone-shaped deposit of sediment (alluvium) emplaced by flowing water, usually occurring where water flow exits a confined space. The shape of alluvial fans is controlled by where the flow velocity decreased, causing sediment to be deposited. The particle size of sediment in alluvial fans is generally finer in the downstream direction.

Alluvium sediment deposited by flowing water.

Barchan dune a crescent-shaped sand dune, formed as wind transports sediment predominantly from one direction. The shape (morphology) of barchan or barchanoid (having some features of a barchan) dune can be used to infer the dominant wind direction because the steepest face forms on the downwind side. Barchan or crescentic dunes are a common type of aeolian dunes (other types being linear, star, dome, and parabolic dunes).

Coppice dune also called a nebkha or dune hummock, a coppice dune is a vegetated sandy mound in which sediment accumulates as vegetation traps wind-transported sand. Coppice dunes typically are lower in height than their associated vegetation.

Deflation lowering of the land surface resulting from wind erosion of fine sediment (opposite: inflation)

Depocenter a region of concentrated sediment deposition, where sediment thickness is maximal. Sedimentary depocenters are commonly found at the mouths of rivers or streams.

Desert pavement a desert surface covered with closely packed, mostly coarse grained (pebble and cobble-sized) sedimentary particles. The pavement-like texture develops as finer grains are removed by wind. Where exposed undisturbed for a long time, desert pavement surfaces develop desert varnish (oxidation and re-cementation facilitated by bacteria) on the exposed particle surfaces. See also **lag deposit**.

Fluvial pertaining to flowing water, as in a river or stream channel.

Geochronology the science of determining the age of sediment, rocks, fossils, or geologic events.

Lag deposit a sedimentary deposit formed by removal of fine-grained material, resulting in residual concentration of coarse-grained particles (commonly gravel). Formation of a lag deposit occurs by the winnowing action of fluvial, aeolian, tidal, or wave-induced sediment transport.

Luminescence geochronology a method of estimating the time at which sediment was last exposed at the land surface. Luminescence geochronology relies on light-emitting (luminescent) properties of mineral grains when they are stimulated by light, infrared radiation, or heat in a laboratory; the magnitude of luminescence is a function of the time since the last exposure to sunlight.

Playa a flat area at the lowest part of an internally drained basin (a basin with no outlet). Playas in deserts commonly form shallow, ephemeral lakes. Sediment accumulating in playa depocenters is reworked by wind when dry, forming aeolian dunes and generating aeolian dust.

Sand sheet a low-relief, sand-covered land surface lacking well developed aeolian dunes.

Sand ramp inclined aeolian sand deposits covering a topographic slope. Sand ramps form against topographic barriers and indicate local loss of wind velocity that promotes deposition of aeolian sediment.

Sedimentary structures textures, patterns, and arrangements of sediment grains that form while or shortly after the sediment is deposited. Sedimentary structures are commonly visible when a sediment deposit or sedimentary rock is exposed in cross-section. Examples of primary sedimentary structures (formed during deposition) include ripples and crossbedding, which form as a result of grain-size or density sorting and indicate the presence of bedforms such as ripples and dunes on the original sediment surface. These features can be used to infer the dominant direction(s) of water currents or wind that transported and deposited the sediment. Examples of secondary sedimentary structures, which form shortly after deposition, include mudcracks and raindrop impressions.

Moffett Field Publishing Service Center, California
Manuscript approved for publication February 25, 2021
Edited by Phil A. Frederick
Layout and design by Cory Hurd

ISSN 2328-0328 (online)
https://doi.org/10.3133/sir20215017